Hydrodynamic Analysis and Optimisation of a Novel "Wavergy" Device for Wave Energy Conversion

A thesis
Submitted to the Naval Architecture and Marine
Engineering Department
Faculty of Engineering – Alexandria University
in partial fulfilment of the requirements
for the degree of
Master of Science
in
Naval Architecture and Marine Engineering

by

Serag el-din Mohamed Salah el-din Mohamed Abdelmoteleb

September 2019

Hydrodynamic Analysis and Optimisation of a Novel "Wavergy" Device for Wave Energy Conversion

Presented by

Serag el-din Mohamed Salah el-din Mohamed Abdelmoteleb

For the degree

Master of Science

In

Naval Architecture and Marine Engineering

<u>Examination Committee</u>   **<u>Approved</u>**

Prof. Dr. Yousri Mohamed Anwar Welaya
Professor of Naval Architecture and Marine Engineering Department
Faculty of Engineering   ………..
Alexandria University (Egypt)

Prof. Dr. Adel Abd Elhalim Banawan
Professor of Naval Architecture and Marine Engineering Department
Faculty of Engineering   ………..
Alexandria University (Egypt)

Prof. Dr. Bayomy Abdelrahman Bayomy
City of Scientific Research and Technological Applications   ………..

Prof. Dr. Tamer Mahmoud Hamed Ahmed
Assistant Professor of Naval Architecture and Marine Engineering Department
Faculty of Engineering   ………..
Alexandria University (Egypt)

Vice Dean for Graduate Studies and Research

Prof. Dr. Magdy Abdelazim Ahmed   ………..

<u>Supervisor's Committee</u>   **<u>Approved</u>**

Prof. Dr. Yousri Mohamed Anwar Welaya
Professor of Naval Architecture and Marine Engineering Department
Faculty of Engineering   ………..
Alexandria University (Egypt)

Prof. Dr. Tamer Mahmoud Hamed Ahmed
Assistant Professor of Naval Architecture and Marine Engineering Department
Faculty of Engineering   ………..
Alexandria University (Egypt)

Acknowledgement

Declaration

I declare that no part of the work referred to in this thesis has been submitted in support of an application for another degree or qualification from this or any other university or institution.

S.M. Abdelmoteleb

Abstract

Oceans contain a large amount of untapped energy in the form of waves, tides, currents and thermal and salinity gradients, the focus in this work will be on wave energy. The energy stored in ocean waves has the potential to cover a significant portion of the global energy consumption and provide yet another sustainable alternative to fossil fuels as a source of energy. However, wave energy is still not extracted at large commercial scale. This is mainly due to the fact that wave energy converters are often subjected to harsh environmental conditions which hinders their ability to safely and cost-effectively extract energy from waves. Consequently, wave energy converters must be designed with survivability as well as cost effectiveness in mind.

This thesis deals with the hydrodynamic optimisation of the Wavergy device. Wavergy is a proprietary patent-pending wave energy converter that is inspired by the molecular lattice structures found in nature. The core concept behind the modular design of Wavergy is to provide redundancy and versatility to ensure safe continuous energy production and facilitate the deployment of the device at various locations with different resource levels. The main objective of this work is to understand the effects of various design parameters, such as the geometric characteristics of the device and the power take-off system properties, on the ability of the device to extract energy from waves.

To put Wavergy's performance into context, a proven wave energy conversion concept namely the Pelamis wave energy converter is used as a benchmark device and its resources represented in volume, power-take off and wave site is applied to Wavergy's optimisation procedure. Finally, Wavergy's performance is assessed at different wave sites and compared to a variety of devices using multiple performance evaluation factors.

Table of Contents

List of Figures

List of Tables

List of Abbreviations

BEM	:	Boundary Element Method
CAPEX	:	Capital Expenditures
CF	:	Capacity Factor
CWR	:	Capture Width Ratio
DOE	:	Design of Experiments
DOF	:	Degree of Freedom
EMEC	:	European Marine Energy Centre
LCOE	:	Levelized Cost of Energy
NLPQL	:	Nonlinear Programming by Quadratic Lagrangian
NOAA	:	National Oceanic and Atmospheric Administration
OPEX	:	Operational Expenditures
OPT	:	Ocean Power Technologies
OWC	:	Oscillating Water Columns
OWSC	:	Oscillating Wave Surge Converters
PTO	:	Power take-off
RAO	:	Response Amplitude Operators
RSM	:	Response Surface Method
TRL	:	Technology Readiness Level
WEC	:	Wave Energy Converters

List of Mathematical Symbols

A_{ij} : Added mass coefficient

A_w : Water plane area of a floating body

B_{ij} : Radiation damping coefficient

B_{PTO} : PTO damping coefficient

C_{ij} : Hydrostatic stiffness coefficient

C_m : Mooring stiffness coefficient

C_{PTO} : PTO stiffness coefficient

F_e : The wave excitation force

F_{hs} : The hydrostatic forces

F_{hd} : The hydrodynamic forces

F_{PTO} : The PTO reaction

F_{Re} : The reaction forces of the systems attached to the WEC (e.g. PTO and Mooring)

F_r : The radiation force

H_s : The significant wave height

$\bar{J}$: The mean wave power flux

K_{ij} : The radiation impulse response function

$\bar{P}$: Mean absorbed power

$\bar{P}_{SS}$: Mean absorbed power for a certain sea state

S_b : Body surface boundary

S_{JS} : The JONSWAP spectral density function

T_p : The peak wave period

V : Fluid velocity vector

Z : Radiation impedance

g : Gravitational acceleration

h : Seafloor depth

k : Wave number

m : Mass

n : Unit normal vector to a surface boundary

p	:	Pressure
r	:	Radial distance from a floating body
β	:	Angle of wave propagation
ζ	:	Free surface elevation from the mean water level
ζ_a	:	Wave amplitude
η_{SS}	:	The probability of occurrence of a certain sea state
ρ	:	Fluid density
ξ_j	:	Motion of a floating body in mode j
ϕ	:	Velocity potential flow function
ϕ_I	:	Incident wave velocity potential
ϕ_r	:	Radiated wave velocity potential
ϕ_s	:	Scattered wave velocity potential
ω	:	Wave frequency
$\hat{\ }$	:	Denotes complex amplitude
$\dot{\ }$	:	Denotes 1st derivative with respect to time
$\ddot{\ }$	:	Denotes 2nd derivative with respect to time

Chapter 1 : Introduction

1.1 Motivation

Since the beginning of the 1970s, the focus on finding alternative energy sources to replace fossil fuels has been rapidly increasing, with renewable energy sources such as wind and solar energy at the centre of this global focus. Forming seventy percent of the earth's surface, oceans have a huge potential as a sustainable energy source that is yet to be unlocked.

Marine renewable energy can take a variety of forms including waves, tides, currents, salinity gradient, and thermal gradient, this work will concentrate on the extraction of energy from waves. In spite of the existence of a wide variety of methods to extract energy from ocean waves with thousands of patents, the wave energy industry is hindered due to the fact that the cost of energy generated from such concepts is still very high to compete with other renewable and non-renewable energy sources. This high energy cost is mainly due to the high installation and maintenance costs and the need for the wave energy converters to endure the hostile nature of the marine environment, this created the need for a wave energy conversion device that is simple, robust and survivable which drove the development of Wavergy a new wave energy conversion concept [1].

1.2 Wavergy: a novel wave energy converter

Wavergy is a proprietary patent-pending design of a wave energy converter. The idea behind Wavergy is nature-inspired as the device mimics the molecular lattice structures found in nature in the sense that the device has a modular configuration with multiple connection points to provide redundancy and distribute the loads exerted by waves. Figure 1.1 shows conceptual drawings of the Wavergy device.

The device is an oscillating wave surge converter that captures wave energy through the relative motion between two sets of modular configurations or "blankets": the upper surface piercing blanket and the lower submerged blanket which is moored to seabed, each blanket consists of a staggered configuration of elliptical cylindrical energy converting modules as show in Figure 1.1 and the two blankets are joined together via connecting rods that are attached to generators located inside each energy converting module through gear multiplication as shown in Figure 1.2 which shows the Wavergy model used for proof of concept [2].

The modular nature of Wavergy can have a lot of advantages compared to WECs that rely on relative motion between few oscillating bodies including the following:

- **Redundancy:** every one of the multiple connections on each individual module serves as its own energy generating point with its own gear multiplication apparatus,
- **Versatility:** the interconnectedness of the device makes the device very flexible and adaptable to any location,
- **Load distribution:** the wave loads are distributed among the numerous connection points of the device meaning that the reaction forces within the device's power take off mechanism will be reduced which increases the device's survivability and robustness.
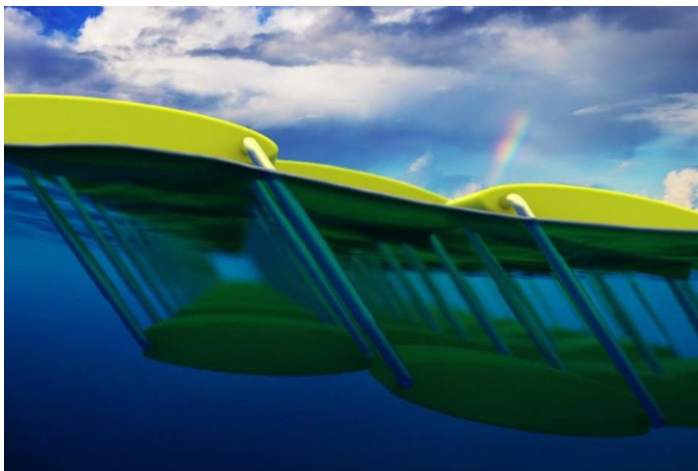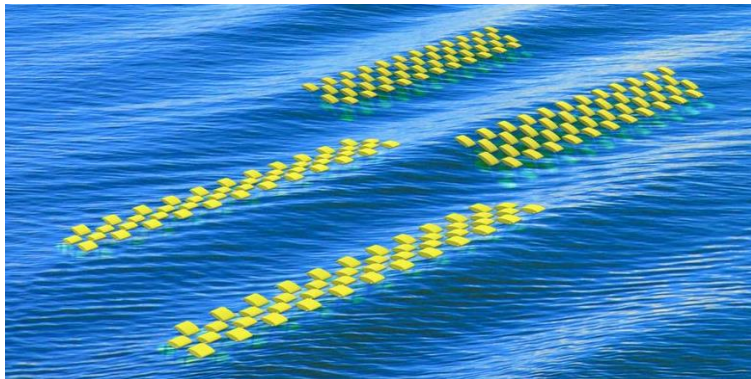
Figure 1.1 Conceptual drawings of the Wavergy device [2]
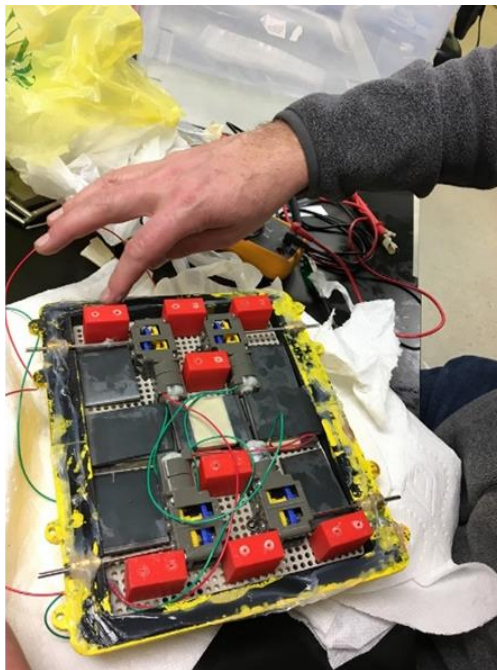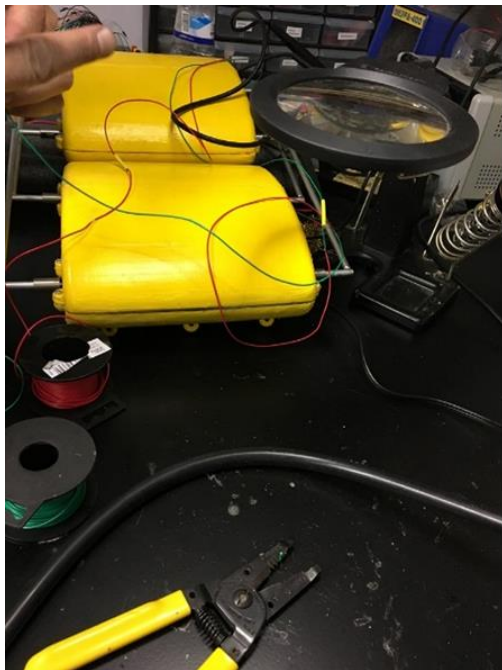
Figure 1.2 Wavergy model used for proof of concept

The aim of this work, is to assess and optimise the hydrodynamic performance of the Wavergy device through manipulating its geometric configuration and the properties of its power-take off system using the Pelamis wave energy converter as a benchmark device with a proven wave energy conversion concept. Various wave sites are also studied and comparisons with multiple wave energy conversion working principles are made.

1.3 Thesis outline

Chapter 2 reviews literature relevant to wave energy and wave energy conversion principles in general and hydrodynamic performance optimisation of wave energy converters in particular. The chapter is split into three sections. The first section provides a background on the global potential of ocean waves as an energy source. In the second section, different wave energy conversion methods are investigated and categorized and an overview of the current status of the wave energy industry is given. The last section presents various studies concerning the evaluation and optimisation of the performance of wave energy converters.

In chapter 3, the theoretical background of the methodology used to model and optimise Wavergy is demonstrated. This chapter covers the application of potential flow theory to the modelling of wave-structure interactions with focus on its use in the prediction of the responses of wave energy converters. Also, a brief discussion of the optimisation schemes used throughout the thesis is given at the end of the chapter.

The numerical modelling of the Wavergy device using ANSYS AQWA software is introduced in chapter 4. First the description of the Pelamis benchmark device is given and its resources represented in its total volume, power take-off damping and wave site are described. Secondly, the Wavergy device's modelling procedure is split into two steps the first step involves modelling only a single surface piercing energy converting module to optimise its geometric parameters and the second step uses a full modular configuration to investigate the effects of the number of modules and the spacing between. The final section derives the equations used to calculate the responses and the mean absorbed power of the Wavergy device.

The results and discussion of the aforementioned numerical modelling procedure is presented in chapter 5. The first two sections of this chapter introduce the results of the optimisation of the single module and multiple configuration of the Wavergy device using the Pelamis benchmark device's resources as constraints. In the third section, the results obtained in the previous sections by frequency-domain statistical analysis are verified using a time-domain analysis. In the fourth section, the optimised power matrix of the chosen Wavergy designs is derived. The last section gives a comparison between the Wavergy device and the published results of various wave energy converters in different wave sites using different performance evaluation measures.

Finally, Chapter 6 provides the conclusions and the suggested further work based on the results presented in the previous chapter.

Chapter 2 : Literature Review

2.1 Potential of ocean waves as a power resource

Various studies have tackled the issue of quantifying the magnitude of the global energy residing within ocean waves. This section reviews a few of these studies to shed a light on the motivation behind pursuing the ocean waves as a renewable energy resource.

Motivated by the rising oil prices and the renewed interest in sustainable clean energy sources, in 1976, Panicker estimated the total global wave power by calculating wave power in the Northern hemisphere using the wave data obtained from the Climatological Division of the fleet numerical weather centre in Monterey, California [3]. He then estimated the wave power in the Southern hemisphere by multiplying the previously calculated power of the Northern hemisphere by the ratio of the percentages of oceanic area to land area of Southern and Northern Hemispheres (80.9/60.7). Adding the power content of both hemispheres, he found the total global wave power at 12Z October 2nd 1975 to be 90000 TW. He also obtained a rough figure of the global wave power transfer to the coastline by assuming a global average wave height of 1 m and period of 8 s and by considering the total length of the global coastline to be 336,123 km, giving a total wave power along the coastlines of 5.3 TW which is of the same order of magnitude as the 2.2 TW predicted by Kinsman [4].

In 2010, Mørk et al computed the theoretical global wave power based on the wave data available from the WorldWaves database (a global wind-wave model validated and calibrated against satellite altimeter and buoy data) [5]. The evaluated global gross power resource was 3.7 TW and when they excluded areas with wave power density of 5 kW/m and potentially ice-covered areas the net power resource was found to be about 3 TW.

In an article published in 2012, Gunn and Stock-Williams analysed data collected from NOAA WaveWatchIII over a 6-year period and calculated the energy flux across a "buffer line" 30 nautical miles offshore of the global land mass (excluding small islands) [6]. They estimated the theoretical global wave power resource to be 2.1 TW (roughly 18500 TWh per year). This estimate was compared with other assessments of the global wave power resource and was found to agree well with most estimates including that of Kinsman [4] and Panicker [3].

To put the previous figures into perspective let us consider the contribution of renewable energy sources to the annual production of electric power, according to the energy policy network REN21's renewables global status report of 2018 [7] the estimated renewable energy share of global electric power production at the end of 2017 is 2195 GW which is enough to supply 26.5% of the global electric power production. This figure is distributed among renewable energy sources as follows: 16.4% from Hydropower, 5.6% from Wind power, 2.2% from Bio-power, 1.9% from Photo Voltaic Solar power and only 0.4% of the global power production comes from Ocean, concentrated solar power and geothermal power combined which amounts to only about 1 % of the global wave power resource estimated in the aforementioned studies. This shows that wave power has the potential to cover a significant portion of the renewable resources contribution to the global power production. However, wave power cannot solely provide the global power needs.

2.2 Extracting energy from ocean waves

The immaturity of the wave energy conversion field compared to other commercialized renewable energy sources and reflected by the poor contribution to the global power production as mentioned in the previous section may mislead the reader into thinking that wave energy extraction is a relatively new concept. On the contrary, the idea of harnessing energy from ocean waves has been around for a long time. In fact, the first known patent of a device that uses waves to produce energy dates back to 1799. Currently, there are more than 3000 inventions [1] for extraction of energy from ocean waves yet wave energy conversion devices is still not commercialized, which raises the question: why is wave energy lagging behind other renewable energy sources despite the idea being around for so long?

To answer this question we first need to know how wave energy can be extracted, the different concepts that are available for wave energy extraction, and what is the level of technical maturity of the existing devices. Exploiting ocean wave energy can be done in a variety of ways like converting the motion response of a structure resulting from wave action into electric energy using a power take-off system or other form of useful energy or using wave power to pressurize sea water and run it through a reverse osmosis process for desalination. This work concerns itself only with wave energy converters (WECs).

Unlike other renewable energy sources such as wind and solar energy which have reached the commercialization stage through wind turbines and solar panels, wave energy is yet to reach this level of maturity. Consequently, there is a wide variety of working principles for wave energy converters. This variation ranges from very simple ideas like heaving buoys making use of vertical motion due to wave action to generate electricity through electric generators to complex ideas like using bulge waves and flexible bodies.

In 2010, Falcao addressed this issue in a review of WECs technologies that emerged since the 1970s. The review covered topics like the characterization of wave energy resource, theoretical background of wave energy conversion, WECs classification, prototypes and specific equipment for WECs, most of the work was dedicated to reviewing different WECs concepts. WECs can be classified in various ways including their location with respect to shore (on shore, near shore and offshore) and their size and orientation with respect to waves (point absorbers, attenuators and terminators). Another classification suggested by Falcao is to classify WECs according to their working principles as shown in Figure 2.1, this classification is based on working principles that reached prototype stage or were object to extensive development effort.

In the following subsections different working principles of WECs are reviewed following Falcao's classification and then other non-conventional WEC concepts are briefly discussed. These principles are illustrated through representative wave energy conversion project examples given throughout this review. After that, hydrodynamic performance of different WEC principles is assessed through literature. Finally, this section ends with highlighting the current status of WEC projects around the world and the main factors hindering the wave energy conversion field development.
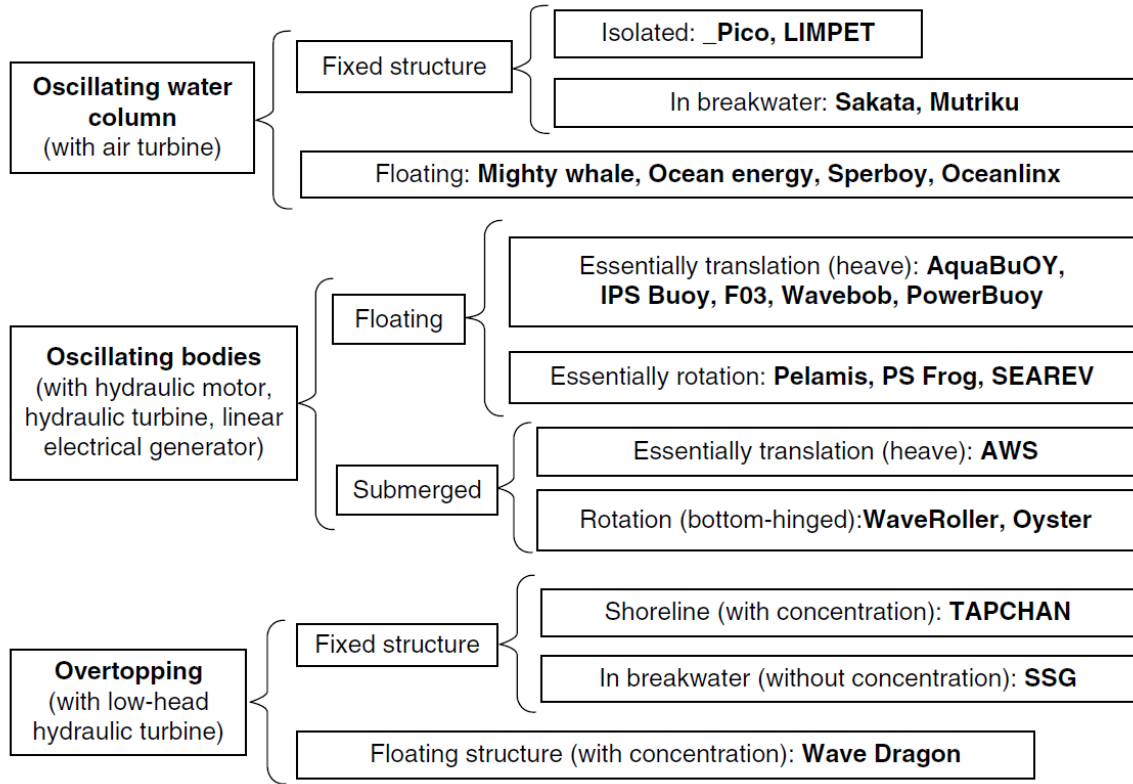
Figure 2.1 Falcao's classification of WECs working principles [8]

2.2.1 Oscillating Water Columns (OWCs)

Oscillating water columns or OWCs are devices that uses water surface to trap air inside a structure (fixed or floating) much like a piston in an internal combustion engine, as the water level falls and rises in the structure due to wave action, the air is forced in and out through a self-rectifying turbine (the most commonly used is the Wells turbine which has symmetric airfoil blade sections to ensure that the turbine will always rotate in one direction) generating electricity as shown in Figure 2.2.
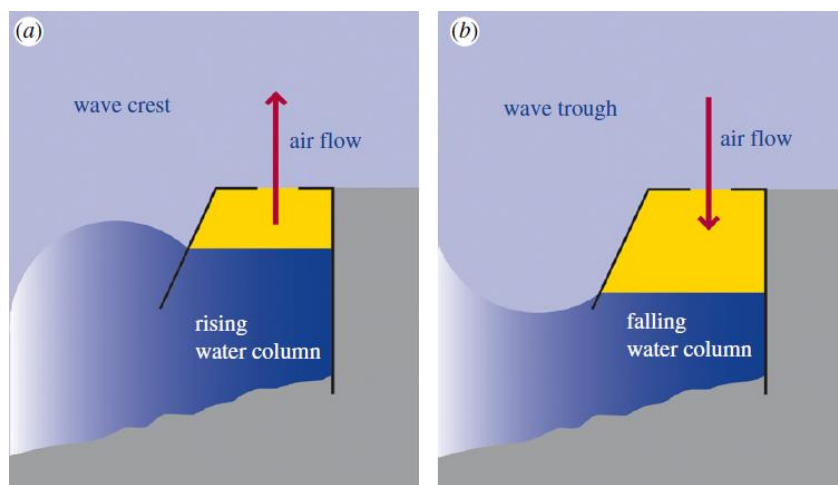
Figure 2.2 Oscillating Water Column principal schematic [9]

6

In his review, Falcao distinguished between fixed and floating structure OWC devices. He described the fixed OWC WECs as first generation devices which is a term used to describe devices that are built on shore since the most early wave energy conversion devices were located on piers and breakwaters. He mentioned several full-sized OWC projects both fixed like the LIMPET plant built on Islay Island, Scotland and floating like the Mighty Whale deployed near the mouth of Gokasho Bay, in Mie Prefecture, Japan in 1998. The power output of the full-sized projects covered in Falcao's review ranged from 60 kW to 2000 kW [8].

In 2000, Heath covered the historical background of OWC development on Islay Island and the conception of the LIMPET plant. The LIMPET (Land Installed Marine Energy Transformer) started after Professor Trevor Whittaker at the Queens University of Belfast had proved the oscillating water column principle using a 75 kW prototype built in Islay in 1991, the prototype showed that OWC structures could be built on an exposed shoreline. Having proven the soundness of the concept, a 500 kW full-sized power plant was built on the island in 2000 with the following purposes: connect the plant to the local electricity grid and operate as a prototype power station; instrument the plant to monitor environmental loads, power performance and the quality and quantity of delivered power; experiment with different control settings to optimise the matching of the plant to different sea states; and compare full scale performance with the predictions of mathematical and wave tank models. The project was considered as a success since it demonstrated that a wave energy extracting power plant can be built in adverse conditions on an exposed cliff edge and operate with reliability as an unmanned unit [10].

The LIMPET plant continued operation for 12 years registering 60000 hours in 2012 and was mainly used as an air turbine testing facility. The project was shut down in 2013 due to the company's shift of focus towards current turbines [1, 9].

In an opinion piece on OWCs technology, Heath mentioned the various advantages of the OWC principle that makes them stand out among other wave energy conversion technologies. These advantages included the following [9]:

- The turbine is the only moving part with no moving parts in the water which improves the reliability of the device
- The adaptability of the concept and its capability to be implemented on a range of collector forms placed on the coastline, nearshore or floating offshore
- Eliminates the need to use gearboxes due to the use of air turbines

However, the concept does have some drawbacks mainly because the size of the required structures and the power take-off system, which raises the following issues [1]:

- High initial civil engineering costs
- Aesthetic problems with large scale projects
- Dependence on the relatively poor performance of air turbines

2.2.2 Oscillating (wave-activated) Bodies

This class of WECs include a very wide variety of technologies, nevertheless, the main principle is always the same: the relative motion between an oscillating structure (floating or submerged) and a fixed frame or other oscillating structures is exploited to generate electricity using power take-off (PTO) mechanisms.

Falcao further classified this family of WECs according to whether they are floating or submerged and whether they depend essentially on translational or rotational motion as shown in Figure 2.1 [8]. This can be somewhat confusing since some devices may rely on different modes of motion or have both submerged and floating parts.

Babarit used a different approach to categorize this class of WECs in his book *Ocean Wave Energy Conversion* published in 2017. He distinguished between two different types of oscillating bodies showing very different hydrodynamic properties: devices based mainly on vertical motion and devices based mainly on horizontal motion [1]. This approach will be employed here since it separates between two types of WECs with very different hydrodynamic performances and properties as pointed out by Babarit in his book.

2.2.2.1 Wave energy converters mainly based on vertical motion

This subclass of devices converts the vertical motion of one or more floating buoys, resulting from wave-action, into electric energy using a PTO mechanism which can be a direct-drive generator (mostly linear) or a hydraulic cylinder driving a generator through a hydraulic motor. Perhaps the simplest principle of a wave energy conversion device is the heaving buoy which consists of an axisymmetric float, with a vertical axis, floating on the surface of water or suspended below it, the float is connected to a mooring point via a cable with the PTO system inserted between the cable and the mooring point or between the cable and the float. In case of deep waters where seabed can't be feasibly used as a fixed reference, the device must be self-referenced, meaning that the float should be moving relative to another float or multiple floats and the PTO system is inserted between them. For multiple floats with articulated joints the relative motion exploited is essentially rotational (mainly pitch) not translational vertical motion (heave) yet Babarit argues in his book that these devices still fall under the same category as heaving buoys since they essentially consist of large-sized horizontal floats subject to vertical efforts of which the motion of the centre of gravity is, at first order, also vertical [1].

A well-known example of the heaving buoy principle is the Ocean Power Technologies (OPT) Powerbuoy. The Powerbuoy, as described by Meckhiche and Edwards of Ocean Power Technologies in their paper in 2014 [11], consists of a torus-shaped float oscillating along a floating spar connected to a submerged plate at its lower end which is moored to the seabed as shown in Figure 2.3. The relative translational heave motion between the float and the spar is converted to rotational motion via a mechanical actuator which drives an electric generator to produce electric energy which in turn is transmitted to shore by the means of underwater cables. The concept was under development since 1994 with various prototypes deployed in the United States, United Kingdom, Spain and Hawaii. The PB40 prototype deployed in Hawaii in 2009 registered 4400 h of operation in August 2010. A pre-commercial 3 kW Powerbouy (PB3) was deployed in 2016 to supply sensors and isolated offshore systems [1].
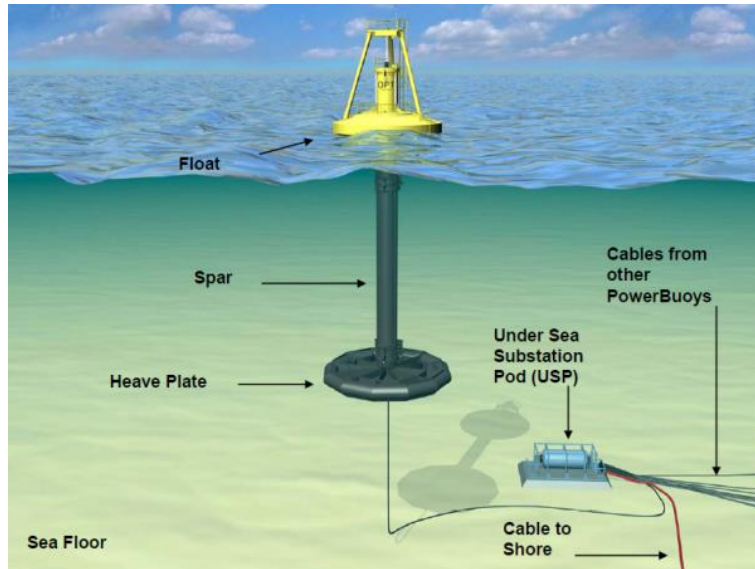
Figure 2.3 OPT Powerbuoy system [11]

Another very famous example both for its success and its unfortunate demise is the Pelamis wave energy converter developed by Ocean Power Technology Ltd founded in 1998. In 2000, Yemm, Henderson and Taylor described the development of the Pelamis WEC program. Designed with survivability as the key objective, the Pelamis device is made up of articulated semi-submerged cylindrical sections with their axes aligned with wave propagation direction and linked together by hinged joints that are designed to induce a tuneable resonant response to increase power production across several sea states, these joints resist the motions of the cylinders due to waves using hydraulic rams which pump high pressure oil through hydraulic motors via smoothing accumulators, in turn the hydraulic motors drive electrical generators which produce electric energy. Electricity produced from all joints, possibly from multiple devices, travel to a junction on the seabed by an umbilical cable, then to shore by another cable as shown in Figure 2.4 [12].
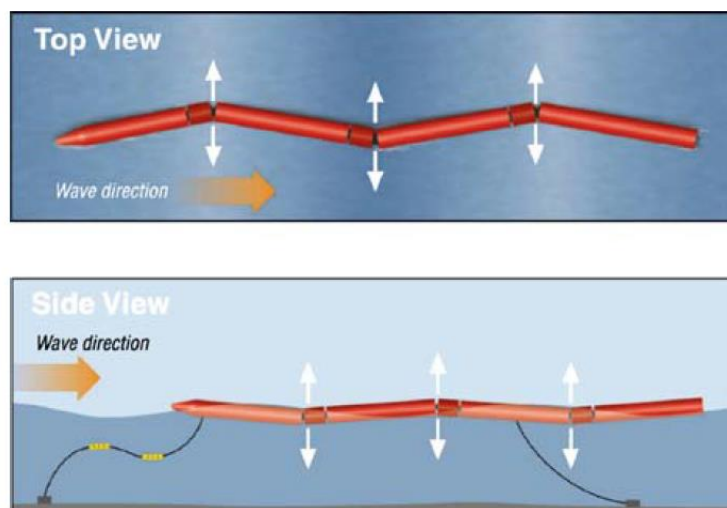
Figure 2.4 A schematic of the Pelamis WEC [13]

9

Several model tests have been conducted along with numerical simulations prior to deploying the first full-scale prototype Pelamis P1 in 2004 in Orkney Islands in Scotland, the device was 120 m long and 3.5 m in diameter. Within the following 3 years, from 2004 to 2007, the company developed the second generation of the device the Pelamis P2 which measured 180 m in length and 4 m in diameter and an installed power of 750 kW. The Pelamis P2 made history when it became the world's first wave power machine to be purchased by a utility company in 2009 and was installed at European Marine Energy Centre's (EMEC) Billia Croo wave test site in 2010. Despite being hailed as the first commercially available WEC, the award winning company wasn't able to secure funding and went into administration in November 2014 and its assets are now owned by Wave Energy Scotland [14].

2.2.2.2 Wave energy converters mainly based on horizontal motion

At first sight waves might seem like a predominantly vertical phenomenon as one may perceive the sea surface to be oscillating up and down, however, in reality water particles in waves have horizontal velocity of the same order as their vertical velocity and may be even higher in shallow waters. WECs that exploit this horizontal motion to absorb wave energy are often referred to as Oscillating Wave Surge Converters (OWSCs), these devices usually consists of a flap or a floating structure that oscillates back and forth relative to a seabed-fixed or moored frame of reference. This concept is analogous to wave makers in wave tanks if run in reverse [1].

The Oyster WEC developed by Aquamarine Power Ltd in 2005 is a typical example of OWSCs. The original design of the Oyster WEC that operated at 12 m water depth was described by Whittaker et al. in 2007. The 350 kW device consisted of an 18 m wide, 10 m high buoyant flap hinged to a sub-frame which is pinned to seabed by tensioned anchors as shown in Figure 2.5. The surging forces from waves makes the flap oscillate, the oscillation of the flap compresses and extends two hydraulic cylinders, located between the flap and the sub-frame, pumping high pressure water through a pipeline to shore. A hydro-electric plant on shore made out of a turbine driving a variable speed electric generator coupled to a flywheel. The output power flow is regulated using hydraulic accumulators, a spear valve and the flywheel [15].
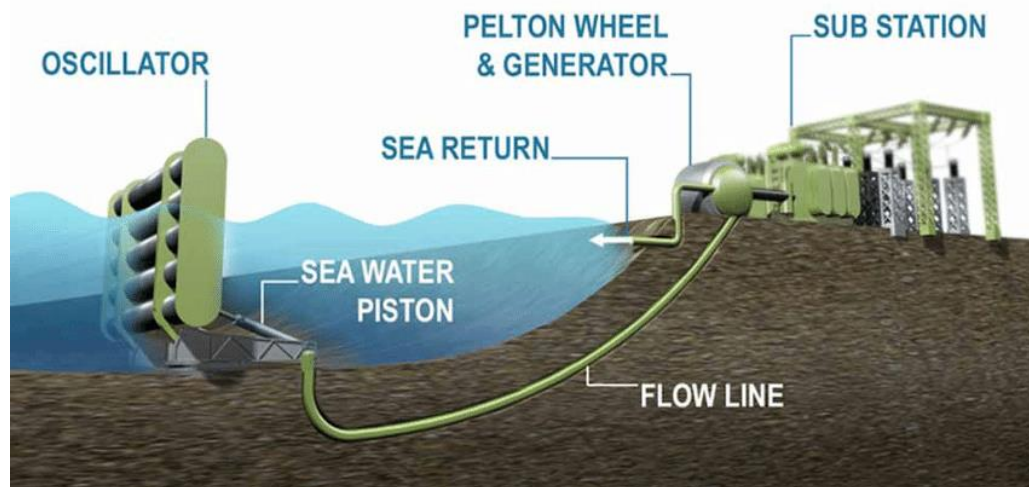
Figure 2.5 General arrangement of Oyster [15]

Two full-scale prototypes of Oyster have been deployed, the Oyster 1 which generated 315 kW with an 18 m wide flap was installed in 2009 at EMEC's wave test site, and later in 2011 the device was replaced with Oyster 800 which generated 800 kW with a 26 m flap and registered 20000 hours of operation in 2014. Unfortunately, like Pelamis, Aquamarine Power went into administration in 2016 [1, 16].

Oscillating bodies offer a wide range of options for wave energy conversion and their ability to tap into the larger more energetic regions of the oceans makes their potential supersede other working principles. Nonetheless, their development faces some difficulties especially regarding survivability and optimal control. This is a result of their dependence on multiple moving parts which entails the need for end stops in high seas in addition to the highly chaotic nature of the sea waves which makes their prediction for optimal control very difficult [1].

2.2.3 Overtopping devices

Overtopping devices make use of the accumulation of sea water due to wave breaking to fill a reservoir above sea level converting wave energy into potential energy, water is then drained through a low head turbine at the bottom of the reservoir to generate electricity.

The Danish WEC Wave Dragon, invented by Erik Friis-Madsen of Löwenmark Consulting Engineers, can be considered as the archetype of this class of WECs [17]. The device is comprised of two wave reflectors for wave-focusing, a ramp to lead waves to the reservoir for over topping and low head turbines to convert the flow due to static head into electricity as shown in Figure 2.6.
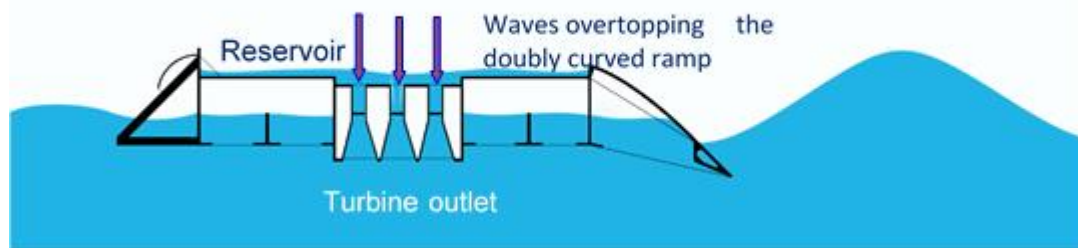
Figure 2.6 Wave Dragon WEC schematic [18]

Wave Dragon concept was tested from 2003 to 2005 and from 2006 to 2007 using a 237 tonnes floating prototype deployed at test site of the Danish Wave Energy Test Center in Nissum Bredning. The prototype was designed as a full-scale model relative to the wave climate at the test site which corresponds to 1:45 scale for North Sea deployment. Tests verified the Wave Dragon energy capturing capabilities with 20,000 hours of continuous operation [18].

Like Oscillating water columns, overtopping devices have the advantage of simplicity regarding their mechanical design since the only moving part is the low head turbines. Moreover the low head turbines have high efficiency and the ability of the device to store water plays an important role in smoothing the power output. Be that as it may, the devices depend critically on the beach slope as it determines the type of wave breaking.

2.2.4 Other principles for wave energy conversion

Other non-conventional WEC working principles that do not fall in the categories described in the previous sub-sections include making use of deformable bodies and lifting surfaces. The following illustrates some wave energy conversion technologies that make use of such principles.

The ANACONDA WEC, as presented by Chaplin et al. in 2007 [19], takes advantages of bulge waves travelling along submerged rubber tubes to capture wave energy. The idea is analogous to the process by which the heart pumps blood through arteries. The pressure fluctuation caused by a wave passing above the tube excites a bulge wave of water to travel along the flexible rubber tube to the stern of the tube where it is captured by the hydraulic PTO mechanism which consists of a one way valve, hydraulic accumulators and unidirectional hydraulic motor [20]. A single ANACONDA device is a sea-snake like rubber tube which is 200 m in length and 5.5 m in diameter filled with water and positioned just below the sea surface and is projected to generate 1 MW which is enough to power over 1000 households, Figure 2.7 shows the ANACONDA WEC.

Figure 2.7 The ANACONDA WEC [19]

Wave energy can be converted into forms of energy other than electricity like using it to generate extra thrust for seagoing ships in rough weather, this concept is referred to as "Wave propulsion" or "Wave devouring propulsion". In their paper T.M. Ahmed, Y. Welaya and S.M. Abdulmotaleb [21] showed that by using bow-mounted hydrofoils on a 90 m platform supply vessel advancing in regular head waves to generate thrust by exploiting wave induced motion, namely heave and pitch, an average thrust deduction of 34 to 42 % of the calm water resistance of the vessel at three different forward speeds was obtained. Those results were validated using the experimental results of a similar vessel published by Steen and Bockmann of NTNU [22].

12

2.2.5 An Overview of the current status of WECs and the challenges facing their development

In an extensive review of wave energy technologies Babarit highlighted several demonstration projects that have been carried out for a number of wave energy conversion devices. Table 2.1 summarizes WECs that showed technical maturity according to Babarit's criteria: the devices have undergone full-scale demonstration, have been continuously deployed for more than a year, and the trial end date is not related to a catastrophic failure [1].

Table 2.1 List of successful Wave energy converters demonstration projects from 1898 to 2016 [1]

Name	Country	Principle	Power (kW)	Period	Deployment time (years)	Energy Production (MWh)	Project outcome
Wave motor	US	Oscillating water column	?	1898-1910	12	?	Decommissioned in 1910
Navigation buoys	JP	Oscillating water column	1	1945-?	>20?	?	Marketed
Islay OWC	UK	Oscillating water column	75	1991-2000	9	?	Replaced by LIMPET
McCabe Wave Pump	IRL	Articulated Heaving Bodies	?	1996	?	?	Hydraulic circuit fault
Mighty Whale	JP	Oscillating water column	110	1998-2000	2	84	Decommissioned in 2000
Pico OWC	PT	Oscillating water column	500	1999; 2006-2016	9	>84	Turbine fault in 1999 Operational from 2006 to 2016
Limpet	UK	Oscillating water column	500	2000-2012	12	?	Stopped
Pelamis P1	UK	Articulated Heaving Bodies	750	2004-2007	3	?	Decommissioned
PB40	US	Heaving Body	40	2005-2006; 2007-2008; 2009-2011	>1	?	Decommissioned
Seabased	SE	Heaving Body	?	2006-?	>1	?	Operating
Wavestar	DK	Articulated Heaving Bodies	110	2009; 2010-2013	>3	?	Decommissioned in 2016
Pelamis P2 (2x)	UK	Articulated Heaving Bodies	820	2010-2014	>1.5	>250	Decommissioned
Mutriku	ES	Oscillating water column	259	2011-?	>5	>1300	Operating
Oceanus 1 (3x)	UK	Heaving Body	?	2011; 2012-2013	>1	?	Decommissioned
Lifesaver	UK	Heaving Body	400	2012-2013	1	4.64	Decommissioned
CETO 5 (3x)	AU	Heaving Body	240	2014-2016	>1	?	Decommissioned
Oceanus 2	UK	Heaving Body	162	2014-2015;2016-?	>1	?	Operating
W1	ES	Heaving Body	200	2014-?	>1	?	In operation
PH4S version 1	FR	Oscillating wave surge converter	1.5	2015-2016	>1	?	Decommissioned
Sharp Eagle 1 Wanshan	CN	Oscillating wave surge converter	100	2015-?	>1	>30	In operation
ISWEC	IT	Oscillating wave surge converter	100	2015-?	>1	?	In operation
Jeju islan	KR	Oscillating water column	500	2015-?	>1	?	In operation
PH4S version 2	FR	Oscillating wave surge converter	5	2016-2018	>1	?	In operation
OBREC	IT		2.5	2015-?	>1	?	In operation
Seabased (36x)	SE	Heaving Body	30?	2016-?	>1	?	Pilot farm

It is obvious that the problem with commercializing wave energy is not technical per se as a lot of devices have already successfully generated power from waves for prolonged time periods. Nevertheless, the cost of the energy extracted from these devices are relatively high due to costly installation and maintenance operations. According to the International Renewable Energy agency report of 2014 the cost of wave energy is of the order 0.33-0.63 €/kWh, comparing that figure to electricity pricing around the world which is roughly valued at 0.1-0.3 €/kWh clarifies the reason why wave energy is struggling in competing in the global energy market [23]. Consequently, wave energy converters need to be designed with robustness, easy maintenance and low initial costs in mind which prompted the conception of Wavergy, a novel device for wave energy conversion. The Wavergy device is still in the preliminary design stage and this work deals with the initial assessment of its hydrodynamic performance.

2.3 Hydrodynamic performance and optimisation of WECs

In 2005, Babrit and Clément [24] optimised the geometry of the SEAREV wave energy converter. The device consisted of an enclosed hull with an off-centre cylindrical inner mass (Pendulum) that is free to rotate about its axis, the relative motion between the hull and the inner mass caused by wave action is used to drive a generator via a hydraulic pump. The shape of the device was optimised using a two layer multi-objective optimisation scheme in which the first layer used genetic algorithms to optimise the geometry of the hull which was the first use of genetic algorithms in optimising WECs according to the authors' knowledge and the second inner layer employed a gradient based method to find the optimal Pendulum for each hull. Mean annual extracted power was calculated for Yeu Island, on the west coast of France as a test case site with mean annual power flux of about 23 kW/m. The objectives were to maximize the absorbed power and minimize the displacement of the device. First, a parallelepipedic shape was considered with 4 parameters for optimisation namely the length, beam, draft and vertical position of the centre of gravity, after that two more shapes were considered: a cylindrical hull and a semi-cylindrical hull with a keel to house the inner cylinder. It was found that for a given family of geometric shapes the values of the characteristic lengths (parameters) were significant for design optimisation and that the efficiency of the device depended on its shape. The shape that provided the best performance was the semi-cylindrical hull. Another important insight is the fact that as the displacement of the optimal device on the pareto front increases, the length and draft of the device remain constant (10 and 20 m respectively) meaning that the optimum geometries favour draft over length.

An optimisation methodology for the geometry of wave energy collectors using parametric description of bi-cubic B-spline surfaces was presented by McCabe, Aggidis and Widden in 2010 [25]. The optimisation procedure involved repeated runs of a genetic algorithm for a fixed number of generations then the optimisation is restarted with the best candidates. The device subject to this methodology had two degrees of freedom namely surge and pitch and one or two axes of symmetry in the horizontal plane. The cost function of optimisation aimed to maximize power and penalized large displacements and high velocities. Absorbed power was calculated for a number of incident regular waves, assuming the PTO system is tuned to give maximum power in such waves. Finally, the performance of the candidates was compared to the following benchmark collector shapes: hemisphere, cylinder and cuboid. Initially, 180 runs were performed assessing half a million shapes for the collector with only 11 candidates giving cost function values better than the benchmark shapes of which 9 were unisymmetric and 2 were bisymmetric, i.e. the solution space consisted of a vast majority of bad solutions with few relatively good solutions. Secondly, the optimisation was

14

restarted with the two runs that had the best cost functions among the unisymmetric and bisymmetric collector shapes at the previous stage. The unisymmetric collector shapes showed substantial increase in the cost function over ten independent restarts while less improvement was observed for the bisymmetric collector. The best cost function belonged to a unisymmetric collector shape with a bulbous body and wings that slope backwards from the bottom.

In a study of a selection of WECs in 2012, Babrit et al. [26] estimated the mean annual absorption of a selection of devices with various working principles. The selected working principles were: small bottom-referenced heaving buoy, bottom-referenced submerged heaving buoy, floating two-body heaving converter, bottom-fixed heave-buoy array, floating heave-buoy array, bottom fixed oscillating flap, floating three-body oscillating flap device and a floating oscillating water column. All the devices' PTO systems were assumed to be tuned to give maximum power at every sea state. A wave to wire model was developed for each device using the equation of motion to generate power matrices and hence calculate the mean annual power absorption at 5 different representative wave sites along the European coast with power resource ranging from 15 to 88 kW/m. Four measures were derived to assess the devices' performance: absorbed energy per characteristic mass [kWh/kg], per characteristic surface area [MWh/m^2] and per root mean square of PTO force [kWh/N]. While the absorbed power varied widely between the devices, from 2 to 800 kW, the difference in performance measures were much smaller implying that there was no favourable working principle among the selected devices and justifying the existence of a wide range of WEC concepts since there are no clear best solution to the problem of capturing energy from ocean waves. An interesting finding of this study is the fact that a more powerful wave site does not necessarily mean that more energy is absorbed by the device as some devices show reduced power in more energetic wave sites.

McCabe [27] developed in 2013 a systematic method using genetic algorithms for optimising the shape of a WEC with only one degree of freedom (surge) and one plane of symmetry. The geometry of the collector was described in a manner similar to the one used in the aforementioned study by McCabe et al. in 2010 [25], i.e. using bi-cubic B-spline surfaces. The power absorbed by the device in the North-East Atlantic Ocean wave site was calculated assuming the device is tuned to each sea state. Three cost functions were used to assess the performance of candidate shapes namely: mean absorbed power, mean absorbed power per unit characteristic length of the device and per unit displacement of the device, the three functions are distinguishable through the severity of the penalty put on the device's size with the first one having no penalty at all and the third one with maximum penalty. The optimisation process was subject to four constraint configurations defined by two power limits (2.5 and 5 MW) and two surge displacement limits (5 and 10 m). The results showed an obvious pattern, where the devices with the best first cost function (with no size penalty) favoured large simple collector shapes with the solution slowly evolving to the upper size limits bounded by a hemisphere of radius 12.5 m, the surge displacement limit had only a moderate effect and the power limit had very little effect. This was not the case for the third cost function (with the most severe penalty on size). The shapes with the best values for this function tended to be small and have more complicated geometries and were close to the lower size limit. Shapes with the largest second cost function (with intermediate penalty on size) lied in between the two previous categories. They didn't push the limits on either boundaries of size and were quite sensitive to the displacement and power constraints. A comparison with a benchmark box-shaped device showed that the optimum shapes had a slightly improved percentage using the first cost function, 50% using the second cost function and up to 200 to 300 % using the third cost function. This suggests that

taking both size and mean power into account through the optimisation procedure would significantly improve the performance of the device.

Kurniawan and Moan dealt with optimising the geometries of WECs oscillating about a fixed submerged horizontal axis in 2013 [28]. The multi-objective optimisation was done using genetic algorithms with the purpose of minimizing the two following ratios: wetted surface area to mean absorbed power and PTO reaction force to mean absorbed power. These ratios were integrated over a range of uniformly distributed regular waves with unit amplitude and a wave frequency range of 0.4 to 1.3 rad/s. The body was not allowed to take any shape like the previous studies by McCabe et al.[25]   and McCabe [27]. Instead, four geometric shapes with simple cross-sections were considered and the seven following configurations were tested: a thin vertical flap without eccentricity of the axis of rotation, a thin vertical flap with eccentricity of the axis of rotation, an inclined flap, a curved flap, a surface piercing circular cylinder, a submerged circular cylinder, and a submerged elliptical cylinder defined with 4 different radii as parameters. Among all the geometries considered, the elliptical cross-section results showed the best performance minimizing the two cost functions. Eccentricity of the axis of rotation and inclination of vertical flaps did not improve performance. The Asymmetry of the elliptical cross-section in the wave propagation direction was found favourable by the optimisation algorithm with more volume occupying the downstream part of the absorber. Different constraints were applied to the body motion displacement and it was shown that the more conservative the constraints the smaller the optimal dimensions of the device become. It was also deduced that changing the frequency range would have an effect on the optimal configurations where short incident waves favoured smaller device dimensions and vice versa.

In their paper in 2014, Goggins and Finnegan [29] put forth a general methodology for optimising the geometry of a WEC in order to maximize the response of the device for a specific wave energy spectrum. The methodology entailed describing the geometry of the device using two variables: the shape of the device and its radius. In order to vary the shape of the device, a library of families of geometric shapes is introduced and each family has a draft that is proportional to the specified radius. A radius range and a wave spectrum is inserted as input to the optimisation process in which an array list of Response Amplitude Operators (RAOs) corresponding to a specific radius and shape is filled. The RAOs are then used to calculate the dynamic response spectrum and the associated significant velocity for every combination of shapes and radii. After that the radius and geometry that provide the maximum response can be determined. This method was applied to a case study of a vertical axis-symmetric heaving device deployed in the Atlantic marine energy site, off the west coast of Ireland. The average annual wave spectrum of the wave site and a radius range of 1 to 25 m was used as input with 5 geometric shapes: a truncated cylinder, a truncated cylinder with a 45º linear chamfer, a half-immersed sphere, a truncated cylinder with a hemisphere attached to its base and a truncated cylinder with a quarter in-circle chamfer, in addition to different draft to radius ratios. Overall, the truncated cylinder with hemisphere attached to its base having a radius 8 m and a draft to radius ratio of 2.5 gave the highest response, however, other shapes showed higher responses over specific radius ranges. Finally the power matrix of the device was evaluated by using the optimum damping coefficient for the PTO system for each sea state and the mean annual absorbed power was calculated by multiplying the probability of occurrence of each sea state from the wave site's scatter diagram to the absorbed power of this sea state and was found to be 392 kW. In order to avoid excessive loads from slamming a cut-off significant wave height of 6 m was imposed and was found to reduce the power by 4.74% of its value without restriction.

The influence of various parameters affecting the power absorption capabilities of the Pelamis WEC was investigated in 2014 by Shengnan, Liping and Jianxun [30]. The version of Pelamis used in this study consisted of seven cylindrical sections joined together with hinges and moored to seabed with four mooring lines. The parameters chosen for the study included diameter of the sections, section form, draft and PTO hinge stiffness and damping. The effect of each parameter was studied by varying it separately from the benchmark values and calculating the annual mean absorbed power for Zhejiang Province in Eastern China using frequency domain statistical hydrodynamic analysis. The results showed that power increases monotonically with increasing diameter and that elliptic section form with larger major to minor axis ratios also gives higher power levels. The draft of the device had very little effect on the power performance and it was suggested to use a draft to diameter ratio of 0.5 to 0.6 for stability. The hinge stiffness of the PTO had little effect on power below a certain value of 10^5 N.m/rad beyond which the power level rises a little then drops for high stiffness values. On the other hand, power was very sensitive to the PTO hinge damping and a peak occurs at around $1.5*10^6$ to $4*10^6$ N.m.s/rad. The accuracy of the methodology used were verified using the experimental results of the 20th scale model of the Pelamis performed at Glasgow University.

In 2015, Babarit [31] reviewed the hydrodynamic power performance of a wide variety of WEC working principles through available published results in literature. Power matrices of different devices were either already available in literature or had to be derived or estimated by linear interpolation. A database was created containing information about the WEC type (OWC, overtopping, heaving devices, fixed OSWCs, floating OSWCs), its capture width ratio (*CWR*), its characteristic dimension, the wave resource, the method by which its performance was evaluated and the reference of the information. Initially 156 *CWR* measurements were considered, however, some of the values were believed to be unrealistic or unreliable. Therefore they were discarded leaving only 90 measurements to be included in the database. After analysing the database, it was found that power performance highly depends on the WEC type and that the least efficient types of WECs are the floating OWSCs and the overtopping devices and the most efficient are the fixed OWSCs, lying in between are the heaving devices and OWCs. It was stressed that the *CWR* is a measure of the hydrodynamic power efficiency only and does not reflect economic performance. Other factors like the efficiency of the PTO mechanism or fabrication and operation costs may result in the most hydrodynamically efficient device being a poor choice from the economic point of view.

The optimal sizing and power rating of a WEC in a 20 MW wave energy farm was investigated from a techno-economic perspective through a case study based on CorPower's heaving buoy device by de Anders et al. in 2016 [32]. To be able to compare WEC devices to other renewable energy technologies, a levelized cost of energy (LCOE) model, incorporating the capital expenditure of the 250 kW prototype of the device, was established owing to its wide use in the energy production industry. The operational expenditures (OPEX) were estimated in two different ways: as a percentage of CAPEX and using a failure/repair model taking into account failures of individual WECs in the array. Due to the low technology readiness level (TRL) of WECs, some assumptions regarding: the scaling of the prototype results and costs, the effects of interaction between WECs and the availability of information of operational costs and the life-cycle of the project needed to be made to simplify the study. Generally, results indicated that low to medium power ratings (100 to 250 kW) are optimum, nevertheless, this conclusion depends on the assumptions that were made. Evaluation methods of the CAPEX and OPEX were found to be very

important since different methods resulted in completely different optimal sizing. Five different European wave-sites were chosen to examine the effect of various locations of the techno-economic performance and it was concluded that the sizing is relatively independent on the deployment site given that all the chosen locations had similar resource levels.

A systematic procedure using design of experiments (DOE) method to optimise the geometry of a single-body heaving WEC was presented by Shadman et al. in 2017 [33]. The aim of the procedure was to find the optimal WEC geometry that maximized energy absorption through the largest range of frequencies and to have a natural frequency that is as close as possible to the predominant wave frequency of the design wave site. This was achieved in four steps. The first step was determining the characteristics of the wave site which was chosen to be a nearshore location off the coast of Rio de Janeiro and was described using a five-year wave hindcast based on the WAVEWATCH III wind wave model. Secondly, upper and lower bounds were set to the geometric parameters of the WEC, namely the diameter and the draft. Within these bounds a set of design points was determined. In the third step, the objective functions of the optimisation represented in the natural heave frequency, the resonance bandwidth and the mean power are calculated using a frequency domain hydrodynamic analysis and then the DOE method is applied. Finally, the optimal float geometric parameters are selected based on statistical analysis of the design space. Using DOE method greatly reduces the number of runs required for the optimisation process and gives a better understanding of the behaviour of the objective functions over the domain of the optimisation through graphical representation of the results using contour diagrams and surface plots and further frequency domain and time domain analyses with the optimal design parameters can be used for verification of the results.

In 2018, Al Shami et al. [34] applied the Taguchi method used in the 1950s for optimising industrial chemical processes to optimise the hydrodynamic performance of a two-body WEC. This method investigates the effects of varying different, often correlated, input parameters of a system on the response of the system output by means of statistical analysis which examines the sensitivity of the output variables to the input parameters which then can be tuned to generate more desirable system outcomes. A two-body WEC consisting of a heaving float and a submerged reference body was the subject of this study with seven input parameters: PTO damping; PTO stiffness; diameter of the float; shape and volume of the submerged body; depth of the submerged body; and the draft of the float. The main objectives were to maximize the mean absorbed power and bandwidth of the power-frequency curve, defined as the difference between the frequencies at which the power is half the maximum power, in addition to lowering the resonance frequency of the device to suit the relatively low operating frequency of the Australian oceans which was the deployment site of the device. In order to examine the sensitivity of the output to the input parameters, each input parameter had two levels, and eight design configurations made up of different combinations of these levels were analysed and performance measures were derived. The most effective parameter on captured power was the shape of the submerged body followed by the diameter of the float, the depth of the submerged body and PTO damping with the rest of the parameters having lower effects. The resonant frequency was most sensitive to the volume of the submerged body while the effects of other parameters were negligible. As for the bandwidth, almost all the parameters had an effect with the body shape and PTO stiffness having the largest effect and the PTO damping had negligible effect. The two designs that gave the highest absorbed power and the largest bandwidth were tuned according to the results of the sensitivity analysis to enhance their performance.

Chapter 3 : Theoretical Background

This chapter covers the theory behind the calculations and numerical simulations used throughout this work. The chapter is divided into three sections, the first section deals with the modelling of small-amplitude wave-body hydrodynamic interaction. In the second section, expressions for power absorption and performance measures of WECs are derived. Finally, the methodology used for the hydrodynamic optimisation of the WEC under investigation is briefly outlined.

3.1 Hydrodynamics of wave-body interactions

This section follows the presentation of the numerical modelling of WECs given in Folley [35], similar presentations can be found in Falnes [36].

This hydrodynamic problem can be handled using potential flow theory where the fluid is assumed to be ideal, i.e. inviscid and irrotational. This assumption is justified due to the fact that viscous effects are relatively small and can be neglected for high Reynolds number flows like the interaction between ocean waves and a body (e.g. a WEC) given that the wave and the motion of the body have small amplitudes This condition is true most of the time except when the body encounters extreme waves in which case viscous effects become significant and motions of the body become highly nonlinear and consequently potential flow theory becomes invalid. However, this is out of the scope of this work which focuses on the interaction between waves and WECs in normal operating conditions. In the following subsections, an overview of the potential flow theory and its use in solving the hydrodynamic problem is given, then the derived velocity potentials are used to calculate the forces acting on a WEC in an incident wave field and finally the equation of motion of the WEC is derived in both frequency and time domains.

3.1.1 Application of the potential flow theory to the hydrodynamic problem

Assuming the flow is incompressible, which is acceptable for liquids, the continuity equation takes the following form:

$$\vec{\nabla} \cdot \vec{V} = 0 \tag{3.1}$$

where V is the fluid velocity vector, and since the flow is assumed to be irrotational the curl of the velocity vector is zero hence:

$$\vec{\nabla} \times \vec{V} = 0 \tag{3.2}$$

This allows us to express the velocity vector as a gradient of a scalar function, $\phi(x, y, z, t)$, as follows:

$$\vec{V} = \vec{\nabla}\phi \tag{3.3}$$

Substituting Eq. (3.3) into Eq. (3.1) gives:

$$\nabla^2 \phi = 0 \tag{3.4}$$

Ergo, an incompressible, irrotational and inviscid fluid domain must satisfy Eq. (3.4) which is a second-order partial differential equation known as Laplace's equation. Besides Laplace's equation, the velocity potential of the fluid domain of water waves interacting with an oscillating body has to satisfy the set of boundary conditions given below:

- The water free surface boundary condition
- The seafloor surface boundary condition
- The body surface boundary condition
- The radiation boundary condition
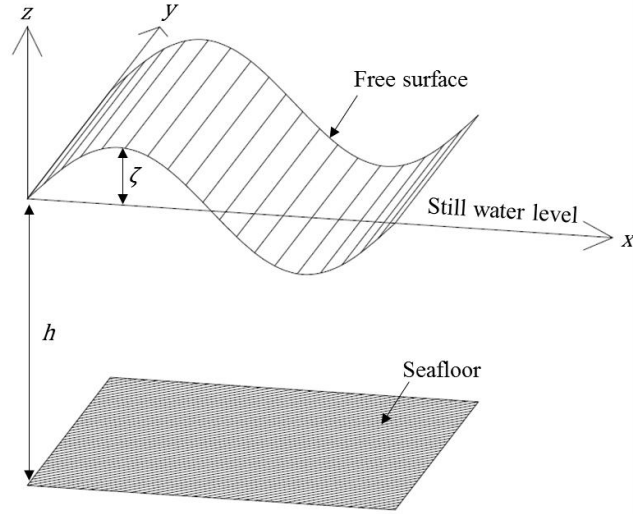
Figure 3.1 Coordinate system

The water free surface has both dynamic and kinematic boundary conditions. The dynamic boundary condition is due to the pressure being constant on the free surface and is given by applying Bernoulli's equation on the free surface:

$$\frac{\partial \phi}{\partial t} + \frac{1}{2}(\nabla \phi)^2 + \frac{p_o}{\rho} + g\zeta = Constant \quad , \text{on } z = \zeta(x, y, t) \tag{3.5}$$

where p_o is the atmospheric pressure, ρ is the water density, ζ is the elevation of the free surface from the mean water level, being positive above the undisturbed water surface as shown in Figure 3.1. If the constant is set to be equal to p_o/ρ, Eq. (3.5) becomes:

$$\frac{\partial \phi}{\partial t} + \frac{1}{2}(\nabla \phi)^2 + g\zeta = 0 \quad , \text{on } z = \zeta(x, y, t) \tag{3.6}$$

The kinematic condition of the free surface requires the fluid velocity component normal to the free surface to be equal to the velocity of the free surface itself, it follows that:

$$\frac{\partial \zeta}{\partial t} = \frac{\partial \phi}{\partial z} + \frac{\partial \phi}{\partial x}\frac{\partial \zeta}{\partial x} + \frac{\partial \phi}{\partial y}\frac{\partial \zeta}{\partial y} \quad , \text{on } z = \zeta(x, y, t) \tag{3.7}$$

20

Both of Eqs (3.6) and (3.7) contain second order terms, hence are nonlinear. These equations can be linearized by applying linear wave theory where the wavelength is assumed to be much larger than the amplitude (waves are not steep) which will result in the second-order terms being of much smaller order than the other terms and therefore can be neglected. The linearity assumption also means that the boundary conditions at the free surface can be applied at the undisturbed water surface rather than the instantaneous surface. The linearization of Eqs (3.6) and (3.7) results in:

$$\frac{\partial \phi}{\partial t} + g\zeta = 0 \quad , \text{on } z = 0 \tag{3.8}$$

$$\frac{\partial \zeta}{\partial t} = \frac{\partial \phi}{\partial z} \quad , \text{on } z = 0 \tag{3.9}$$

Introducing Eq (3.9) into the time derivative in Eq (3.8) gives us the final form of the free surface boundary condition:

$$\frac{\partial^2 \phi}{\partial t^2} + \frac{\partial \phi}{\partial z} = 0 \quad , \text{on } z = 0 \tag{3.10}$$

The seafloor boundary condition is simply due to the impermeability of the seafloor and assuming a flat seafloor of depth h, this condition is given by:

$$\frac{\partial \phi}{\partial z} = 0 \quad , \text{on } z = -h \tag{3.11}$$

The fluid-body interface boundary is also impermeable and thus the fluid velocity normal to the body surface must be equal to the body velocity component in the same direction (v_n):

$$\frac{\partial \phi}{\partial n} = v_n \tag{3.12}$$

Finally the radiation boundary condition states that the wave field far from the oscillating body must be undisturbed or similar to the incident wave field. This implies that the potential that satisfies this condition must decay as the distance from the body increases. Applying the conservation of energy principle results in the magnitude of the potential decreasing with the inverse square root of the distance from the body as follows:

$$\phi \propto (kr)^{-\frac{1}{2}} e^{-ikr} \quad , as \ r \to \infty \tag{3.13}$$

where r is the radial distance from the body and k is the wave number (or the spatial frequency of the wave), see Figure 3.2 for properties of monochromatic regular sinusoidal waves. For water of infinite or finite uniform depth the velocity potential that satisfies the aforementioned boundary conditions takes a sinusoidal form:

$$\phi(x, y, z, t) = \text{Re}\{\hat{\phi}(x, y, z)e^{i\omega t}\} \tag{3.14}$$

where $\hat{\phi}$ is the complex amplitude of the potential function and ω is the wave frequency.

Since the equations that govern the wave-body interaction problem are linear, the solution of the velocity potential can be decomposed as follows:

$$\phi = \phi_I + \phi_s + \phi_r \tag{3.15}$$

where ϕ_I, ϕ_s, ϕ_r are the velocity potentials of the incident, the scattered (or diffracted) and the radiated wave fields respectively. The incident wave velocity potential has to satisfy only the free surface and the seafloor boundary conditions illustrated by Eqs (3.10) and (3.11). In light of Eq (3.14) the complex amplitude of the incident wave velocity potential becomes:

$$\hat{\phi}_I = \frac{ig\zeta_a}{\omega} \frac{\cosh[k(z+h)]}{\cosh kh} e^{ik(x\cos\beta + y\sin\beta)} \tag{3.16}$$

where ζ_a is the wave amplitude and β is the angle between the incident wave propagation direction and the positive x-axis. This velocity potential oscillates in both time and space as illustrated in Figure 3.2, where the temporal and the spatial frequencies are related through the dispersion relation given below:

$$\frac{\omega^2}{g} = k\tanh kh \tag{3.17}$$
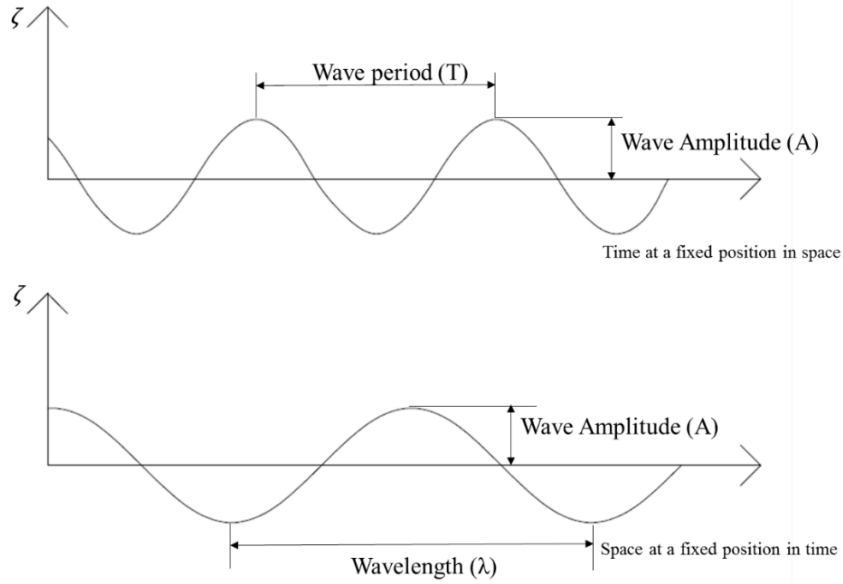
Figure 3.2 Temporal and Spatial elevation variation of sinusoidal incident waves

The scattered wave velocity potential satisfies the body surface body condition assuming the body is fixed in place, the free surface boundary condition and the seafloor boundary condition. The scattered wave field is generated by the interaction of the incident wave and the motionless body, this means that adding the scattered and the incident wave potentials must eliminate the velocity component normal to the body's surface at its equilibrium position, hence:

$$-\frac{\partial\hat{\phi}_s}{\partial n} = \frac{\partial\hat{\phi}_I}{\partial n} \tag{3.18}$$

The final component of the total velocity potential is the radiated potential which represents the wave field generated by the motions of an oscillating body in the absence of the incident wave field. The radiated potential must respect the boundary condition of the body's surface as it oscillates in any degree of freedom (DOF). Thus, this potential takes the form of a superposition of the velocity potentials of the wave fields radiated by each degree of freedom of the body:

$$\hat{\phi}_r = i\omega \sum_{j=1}^{N} \hat{\xi}_j \varphi_j \qquad (3.19)$$

where N is the number of degrees of freedom , $\hat{\xi}_j$ is the complex amplitude of the harmonic motion in mode j and φ_j is a complex coefficient of proportionality corresponding to the complex amplitude of the radiation potential due to motion in mode j with unit amplitude. In case of rigid body motion, j can be one of the six degrees of freedom illustrated in Figure 3.3.
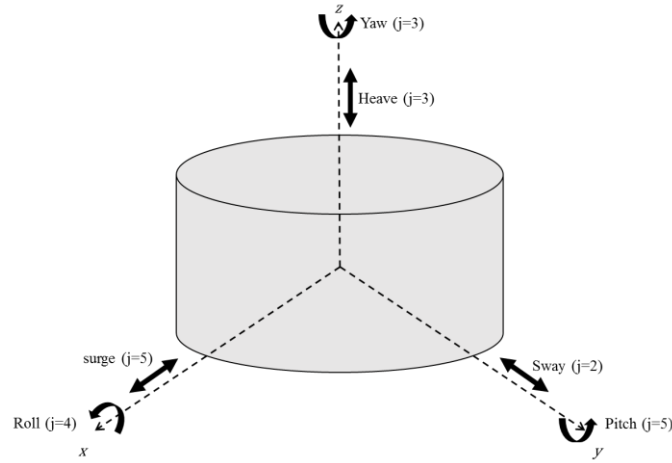
Figure 3.3 Degrees of freedom of a rigid body in space

3.1.2 Formulation of the Equation of Motion of a WEC

The modelling of the hydrodynamic wave-body interaction is based upon Newton's second law where the inertial forces of the body are balanced by the summation of external forces acting on the body. These external forces can be split into the hydrodynamic/hydrostatic forces and reaction forces. The hydrodynamic/hydrostatic forces consist of: the hydrostatic forces caused by the variation of hydrostatic pressure on the submerged part of the body, the excitation forces due to the action of incident waves on a static body, and the radiation forces which results from the radiated wave field caused by the oscillation of the body. The reaction forces may include power take-off (PTO) system's reactions and mooring or foundations reactions WEC. This system is analogous to a mass-spring-damper system as the one shown in the schematic in Figure 3.4, where the stiffness is due to the hydrostatic forces, the damping is due to the radiation forces and the excitation is due to incident waves, in addition to the extra stiffness and damping forces resulting from the accompanying systems like PTO or mooring. Consequently the equation of motion is given by:

$$m\ddot{\xi}(t) = F_P(t) + F_{Re}(t) \qquad (3.20)$$

23

where m is the mass of the body, ξ is the degree of freedom in which the WEC oscillates and the double dots indicates a second derivative with respect to time, i.e. $\ddot{\xi}$ is the acceleration, F_P is the sum of the hydrostatic and hydrodynamic forces due to the interaction of the WEC with waves, and F_R is the reaction forces of the systems attached to the WEC (e.g. PTO and Mooring). This equation can be solved, in order to find the responses of the WEC to an incident wave field, in both Frequency and Time domains as illustrated in the following subsections.
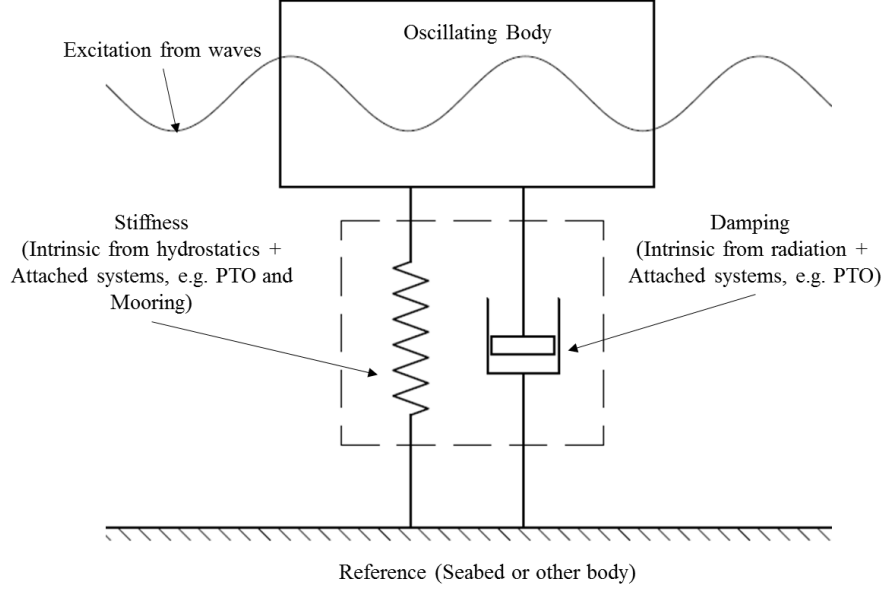
Figure 3.4 Representation of a Generic WEC

3.1.2.1 Frequency-domain solution of the equation of motion

In the frequency domain, if all the forces are linearized and sinusoidal variation of the incident wave field and the body responses is assumed, then the body response in Eq. (3.20) can be described with a complex amplitude and a sinusoidal time-dependent term as illustrated in the following equation:

$$\xi(t) = \text{Re}\left\{\hat{\xi}(\omega)e^{i\omega t}\right\} \tag{3.21}$$

The velocity and acceleration vectors of the body are thus given as:

$$\dot{\xi}(t) = \text{Re}\left\{i\omega\hat{\xi}(\omega)e^{i\omega t}\right\} \tag{3.22}$$

$$\ddot{\xi}(t) = \text{Re}\left\{-\omega^2\hat{\xi}(\omega)e^{i\omega t}\right\} \tag{3.23}$$

where the, ˆ, denotes the complex amplitude. After dividing all the terms by the time dependent term the equation of motion takes this form:

$$-\omega^2 m\hat{\xi}(\omega) = \hat{F}_P(t) + \hat{F}_{Re}(t) \tag{3.24}$$

The first term in Eq. (3.24), $\hat{F}_P$, can be split into two components the hydrostatic force, $\hat{F}_{hs}$, and the hydrodynamic force, $\hat{F}_{hd}$ as given below:

$$\hat{F}_P(t) = \hat{F}_{hs} + \hat{F}_{hd} \tag{3.25}$$

The hydrostatic force results from the imbalance between weight and buoyancy forces due to the body motions, so it tends to restore the body to its equilibrium position. This force can be calculated by integrating the hydrostatic pressure over the wetted body surface. In case of small amplitude motion this force can be linearized to take the following form:

$$\hat{F}_{hs} = -C\hat{\xi} \tag{3.26}$$

where C is the hydrostatic stiffness coefficient, which can be interpreted as the stiffness coefficient of a spring which relates the displacement of the spring from its equilibrium position to the restoring force in the spring. For instance, the restoring force in heave motion is related to the heave displacement through the following hydrostatic coefficient:

$$C_{33} = \rho g A_w \tag{3.27}$$

where A_w is the water plane area of the heaving body.

The hydrodynamic force in Eq. (3.25) is calculated from the velocity potential derived in the previous subsection by integrating the dynamic pressure over the mean wetted surface of the body. The dynamic pressure is obtained from Bernoulli's equation, after neglecting the second order terms and is given by:

$$p = -\rho\left(\frac{\partial\phi}{\partial t}\right) \tag{3.28}$$

Hence, the linear hydrodynamic force will be:

$$F_{hd} = \int_{Sb} pn \, dS_b = \rho \int_{Sb} \left(\frac{\partial\phi}{\partial t}\right) n \, dS_b \tag{3.29}$$

where S_b is the body surface and n is a unit vector normal to the body surface. Following the decomposition of the velocity potential into incident, scattered and radiated potentials, the hydrodynamic force can be further split into two force. Thus the complex amplitude of the hydrodynamic force becomes:

$$\hat{F}_{hd} = \hat{F}_e + \hat{F}_r = i\omega\rho \int_{Sb}(\hat{\phi}_I + \hat{\phi}_s)n \, dS_b - \omega^2\rho \int_{Sb} \hat{\phi}_r n \, dS_b \tag{3.30}$$

where $\hat{F}_e$ is the complex amplitude of the wave excitation force which results from the effect of the incident wave field on the body and $\hat{F}_r$ is the complex amplitude of the radiation force resulting from the radiated wave field due to body motions.

As can be seen in Eq. (3.30) the wave excitation force integral contains the two velocity potentials of the incident wave field and the scattered wave field. This can be interpreted as dividing the excitation forces into two components. The first one is the Froude-Krylov F_{FK} force which is the force that acts on a transparent motionless body due to the incident wave field. The second force is the diffraction force F_s due to the scattered wave field which results from reflection and diffraction of the incident wave on the motionless body. Thus the total excitation can be written as:

$$\hat{F}_e = \hat{F}_{FK} + \hat{F}_s = \mathrm{i}\omega\rho \int_{Sb} \hat{\phi}_I n \, dS_b + \mathrm{i}\omega\rho \int_{Sb} \hat{\phi}_s n \, dS_b \qquad (3.31)$$

The second part of the hydrodynamic force in Eq. (3.30) is the radiation force which is caused by the displacement of water adjacent to the body due to the motion of the body. The complex amplitude of this force is given by:

$$\hat{F}_r = \mathrm{i}\omega Z \hat{\xi} \qquad (3.32)$$

where Z is the radiation impedance and according to Eq. (3.30), it is given by:

$$Z = \mathrm{i}\omega\rho \int_{Sb} \hat{\phi}_r n \, dS_b \qquad (3.33)$$

Eq. (3.33) is analogous to the electric impedance in AC circuits in the sense that it includes the effects of power dissipation or resistance (from resistors) and energy storage or reactance (from inductors and capacitors). Like the electric impedance, the hydrodynamic radiation impedance takes a complex form where the real part represents the resistive effect and the imaginary part represents the reactive effect like illustrated by the following equation:

$$Z = \mathrm{i}\omega\rho \int_{Sb} \hat{\phi}_r n \, dS_b = B + \mathrm{i}\omega A \qquad (3.34)$$

where B is the hydrodynamic damping coefficient which represents the energy dissipated from the motion of the oscillating body to the water via radiating waves from the body, and A represents the added mass coefficient which essentially represents an increase in the inertia of an accelerating body due to the fact that fluid particles in the vicinity of the body are accelerated as well. Thus, the final form of the complex amplitude of the hydrodynamic radiation force is:

$$\hat{F}_r = -\mathrm{i}\omega B \hat{\xi} + \omega^2 A \hat{\xi} \qquad (3.35)$$

where the first term is the dissipative force which is proportional to the body's velocity and the second term is the inertial force proportional to the body's acceleration.

The velocity potentials that are used for the evaluation of the hydrodynamic forces are impossible to obtain analytically from the boundary value problem described in the previous subsection with the exception of very simple geometries. Instead, numerical approaches are implemented by using

boundary element method (BEM) software (e.g. ANSYS AQWA, WAMIT and NEMOH) that numerically solve the boundary-integral equation formulated using Green's function which satisfies the linear boundary conditions outlined previously. For further information about using Green's function to solve the boundary value problem the reader is referred to [37] and [38].

In the context of wave energy conversion extra forces arising from the attached systems like the PTO mechanism and mooring must be included in the equation of motion for the calculation of the responses of the WEC. For convenience, these forces are represented in a form similar to the previous hydrostatic and hydrodynamic forces were a constant coefficient multiplied by the body's complex motion amplitude to calculate the force like the following equations:

$$\hat{F}_{PTO} = -\mathrm{i}\omega B_{PTO}\hat{\xi} - C_{PTO}\hat{\xi} \tag{3.36}$$

$$\hat{F}_M = -C_M\hat{\xi} \tag{3.37}$$

where $\hat{F}_{PTO}$ is the complex amplitude of the PTO reaction, B_{PTO} and C_{PTO} are the PTO system damping and stiffness coefficient respectively, $\hat{F}_M$ is the complex amplitude of the mooring reaction and C_M is the mooring stiffness coefficient. Therefore, the total reaction force F_{Re} in Eq. (3.20) is the summation of these two forces.

Now we can rewrite the equation of motion in the frequency domain to take the following form:

$$[-\omega^2(m + A) + \mathrm{i}\omega(B + B_{PTO}) + C + C_{PTO} + C_m]\hat{\xi} = \hat{F}_e \tag{3.38}$$

More generally for a WEC oscillating in multiple degrees of freedom the equation becomes:

$$[-\omega^2(\mathbf{M} + \mathbf{A}) + \mathrm{i}\omega(\mathbf{B} + \mathbf{B_{PTO}}) + \mathbf{C} + \mathbf{C_{PTO}} + \mathbf{C_m}]\hat{\boldsymbol{\xi}} = \hat{\mathbf{F}_e} \tag{3.39}$$

where the bold font indicates a matrix or vector of the corresponding values in Eq. (3.38) for different degrees of freedom. Finally the WEC's response to a harmonic sinusoidal wave of unit amplitude is given by:

$$\frac{\hat{\boldsymbol{\xi}}}{\zeta_a} = \hat{\mathbf{f}_e}[-\omega^2(\mathbf{M} + \mathbf{A}) + \mathrm{i}\omega(\mathbf{B} + \mathbf{B_{PTO}}) + \mathbf{C} + \mathbf{C_{PTO}} + \mathbf{C_m}]^{-1} \tag{3.40}$$

where ζ_a is the wave amplitude and $\hat{\mathbf{f}_e}$ is a vector containing the complex amplitudes of the excitation forces of the body for a wave of a unit amplitude in multiple degrees of freedom. The ratio between the displacement of the body and the incident wave amplitude is usually referred to in hydrodynamics as the response amplitude operator or RAO.

The frequency-domain model is suitable in the early design stages of WECs since its computational time is relatively small, thus it is used in situations where a large number of configurations has to be assessed as in case of optimising the geometry of the WEC. The main drawback of this method is that it assumes linearity and gives only the steady-state solution of the equation of motion of the WEC, meaning that it cannot handle the nonlinearities arising, for example, from extreme waves or the control strategy of the PTO mechanism or mooring and moreover it does not give any information about the transient motions of the WEC which is crucial to later design stages.

27

To be able to introduce nonlinearities in different stages of the energy conversion process, we resort to solving the equation of motion in time-domain.

3.1.2.2 Time-domain solution of the equation of motion

The time-domain formulation of the equation of motion used here is based on the Cummins equation presented in 1962 [39]. For a generic floating WEC under the influence of wave excitation F_i^{wav} and other external forces (e.g. PTO and mooring) F_i^{ext}, and assuming an inertial reference system centred on the WEC's initial position, the Cummins equation of motion in the $'i'$ direction is written as:

$$\sum_{j=1}^{6}\left((M_{ij} + A_{ij}^{\infty})\ddot{\xi}_j(t) + \int_{-\infty}^{t} K_{ij}(t-\tau)\dot{\xi}_j(\tau)d\tau + C_{ij}(\xi_j)\right) = F_i^{wav} - F_i^{ext}(\xi, \dot{\xi}, t) \qquad (3.41)$$

where M_{ij} and C_{ij} are elements of the mass and stiffness coefficient matrix respectively and A_{ij}^{∞} is the added mass at infinite frequency given by:

$$A_{ij}^{\infty} = \lim_{\omega \to \infty} A_{ij}(\omega) \qquad (3.42)$$

where A_{ij} is the frequency-dependent added mass coefficient evaluated in the frequency-domain. $K(t)$ is the radiation impulse response function which represents the memory effects due to the past motions of the body and is given by:

$$K_{ij}(t) = \frac{2}{\pi} \int_0^{\infty} B_{ij}(\omega)\cos(\omega t)d\omega \qquad (3.43)$$

where B_{ij} is the frequency-dependent radiation damping coefficient evaluated in the frequency domain. Once the impulse response function is known the convolution integral given in Eq. (3.41) can be computed at every time step using either direct numerical integration or state-space representation method. Details about these methods can be found in [35] and [40].

Evidently, this particular time-domain model still use the linearity assumptions since it depends on the hydrodynamic coefficients evaluated in the frequency-domain. Nevertheless, it can still handle the nonlinearities of the restoring forces, the PTO forces and the Mooring forces, all of which are dependent on the WEC motion and can be evaluated at each time step.

3.2 Mathematical description of ocean waves as a power resource

In the previous section, the responses of a WEC were derived for regular sinusoidal waves. However, such waves do not exist in real ocean environment. The real irregular ocean waves can be represented by the superposition of regular sinusoidal waves using wave energy spectra which are defined so that the area bounded by a frequency range is proportional to the total energy per unit area of sea surface of all the regular wave components within that range as shown in Figure 3.5. Thus, the total area under a wave energy spectrum curve represents the energy per unit area of sea surface of a certain sea state [41].
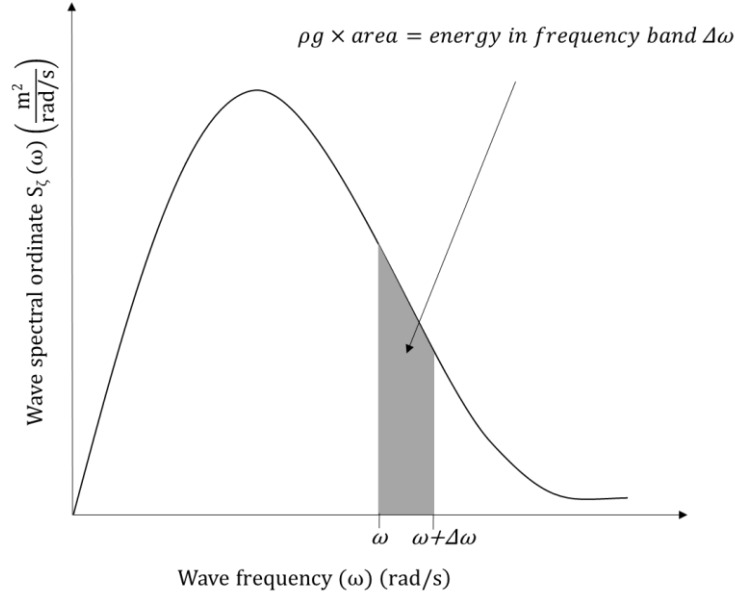
Figure 3.5 Wave spectrum example

Wave energy spectra can be either derived directly from an analysis of irregular wave records or from idealized spectra such as the Joint North Sea Wave Project or JONSWAP spectrum which will be used to represent sea states in the following chapters. The JONSWAP spectrum is defined by three parameters [42]:

- The significant wave height (H_s), defined as the mean value of the highest third of wave heights in an irregular wave height record
- The peak wave frequency (ω_p) (or period (T_p)), which is the dominant wave frequency or period in a certain sea state
- The peak enhancement factor (γ), which relates to the bandwidth of the spectrum, where:

$$S_{JS}(\omega) = \frac{\alpha g^2 \gamma^a}{\omega^5} \exp(-\frac{5\omega_p^4}{4\omega^4}) \tag{3.44}$$

where S_{JS} is the JONSWAP spectral density, and α and a are determined by the following equations:

$$\alpha = (\frac{H_s}{4})^2 / \int_0^\infty \frac{g^2 \gamma^a}{\omega^5} \exp(-\frac{5\omega_p^4}{4\omega^4}) d\omega \tag{3.45}$$

$$a = \exp\left(-\frac{(\omega - \omega_p)^2}{2\sigma^2 \omega_p^2}\right) \tag{3.46}$$

$$\sigma = \begin{cases} 0.07 & ,when\ \omega \le \omega_p \\ 0.09 & ,when\ \omega > \omega_p \end{cases} \tag{3.47}$$

29

The mean wave power flux $\bar{J}$ transported by a unit width of a wave crest for a JONSWAP spectrum in deep water is given by [1]:

$$\bar{J} = 0.4 H_s T_p \tag{3.48}$$

Finally, to characterize a specific wave site, scatter diagrams are used, which contains the probability of occurrence of various sea states, represented by a peak wave period and a significant wave height in a specific site, as the one used later in chapter 4.

3.3 Performance evaluation of WECs

As illustrated in the last section in the previous chapter, several measures were used in literature to evaluate the performance of WECs at early design stages. The simplest of these measures is the mean power absorbed by a WEC which can be calculated from the following equation:

$$\bar{P} = \frac{1}{T} \int_0^T B_{PTO} \dot{\xi}^2 dt \tag{3.49}$$

where $\dot{\xi}$ is the velocity of the WEC in the power capturing DOF. Assuming sinusoidal waves, Eq. (3.49) can be rewritten in the frequency-domain:

$$\bar{P} = \frac{1}{2} B_{PTO} \omega^2 |\hat{\xi}|^2 \tag{3.50}$$

Using mean absorbed power solely as a performance measure can be misleading, especially when comparing different WECs, since it disregards other aspects of the WECs like their size, their principle of operation and their deployment site. This led to the derivation of other measures to assess and compare the performance of WECs, these measures basically rely on normalizing or relating power to other characteristics of the WEC.

The first method of normalizing absorbed power is relating it to the available wave power resource by using non-dimensional coefficients like capture width ratio (*CWR*) and capacity factor (CF). The capture width ratio, which can also be perceived as the hydrodynamic efficiency of a WEC, is defined as the ratio of the power absorbed by the WEC to the power flux per unit length of wave-front multiplied by a characteristic length of the device known as the active width of the device as follows [43]:

$$CWR = \frac{\bar{P}}{\bar{J} * width_{active}} \tag{3.51}$$

The characteristic length or the active width is defined, for all except heaving WECs, as the width of all the device components actively in the primary absorption process of the energy from waves. For heaving devices the active width can be calculated by [31]:

$$width_{active} = \sqrt{\frac{4 A_w}{\pi}} \tag{3.52}$$

30

where A_w is the maximum horizontal cross-sectional area of the device.

As for the capacity factor, it measures the ability of the WEC to capture energy in different sea states at a given site and is given by:

$$CF = \frac{\sum_{SS}^n \bar{P}_{SS} * \eta_{SS}}{Maximum(\bar{P}_{SS})} \tag{3.53}$$

where $\bar{P}_{SS}$ is the mean absorbed from a certain sea state (SS) and η_{SS} is the probability of occurrence of this sea state obtained from the scatter diagram of a specific wave site [43].

The second method of normalizing absorbed power is by simply relating it to another characteristic of the WEC like dividing the absorbed power by: the total volume or wetted surface area, or the reaction force of the PTO, or the maximum motion displacement of the device, or the maximum velocity of the device. The purpose of using these measures for evaluating and optimising WECs' performance is to penalize the high costs correlated with large sizes and high loads resulting from large reaction forces and high velocities and affecting the survivability of the devices.

3.4 Optimisation methodology

The optimisation process used thereafter is based upon Response Surface Method (RSM). This method was presented by Box and Wilson [44] in 1951. This method entails using Design of Experiments (DOE) method to explore the effects of various input variables on one or more output variables, this is done by establishing a design space that consists of design points that represent different combinations of values of the input parameters within predefined limits. After evaluating the output parameters at each design point, full second-degree polynomial response surfaces are generated for every output parameter, which are used to find the input parameters values that give the most desirable output. The values of input parameters of the chosen design points are then verified by direct evaluation of the output values at these points. Furthermore, a gradient based optimisation scheme could be used to ensure local superiority in the design space of the chosen design points. Similar optimisation procedure was used in [33].

Chapter 4 : Modelling Methodology of Wavergy

The main objective of the modelling procedure outlined in this chapter is to assess the quality of the hydrodynamic performance of Wavergy by comparing it to the performance of another well-established benchmark WEC working principle. The device chosen for this purpose is the Pelamis WEC described in [30]. The two devices are compared by setting Wavergy to have the same resources as the Pelamis benchmark device, so that the two devices will have the same wave site, total volume and total PTO damping coefficient, in other words, the Wavergy device described thereafter can be considered as a reconfiguration of the resources of Pelamis. The hydrodynamic modelling of both Wavergy and Pelamis is performed using the boundary element method (BEM) software ANSYS AQWA.

4.1 Description of the benchmark device

4.1.1 Device configuration

The version of Pelamis used in this work consists of 7 cylindrical sections joined together with hinged joints as illustrated in Figure 4.1 which shows the local hinge axes relative to the global coordinate system. Table 4.1 summarizes the characteristics of this configuration as given in [30].
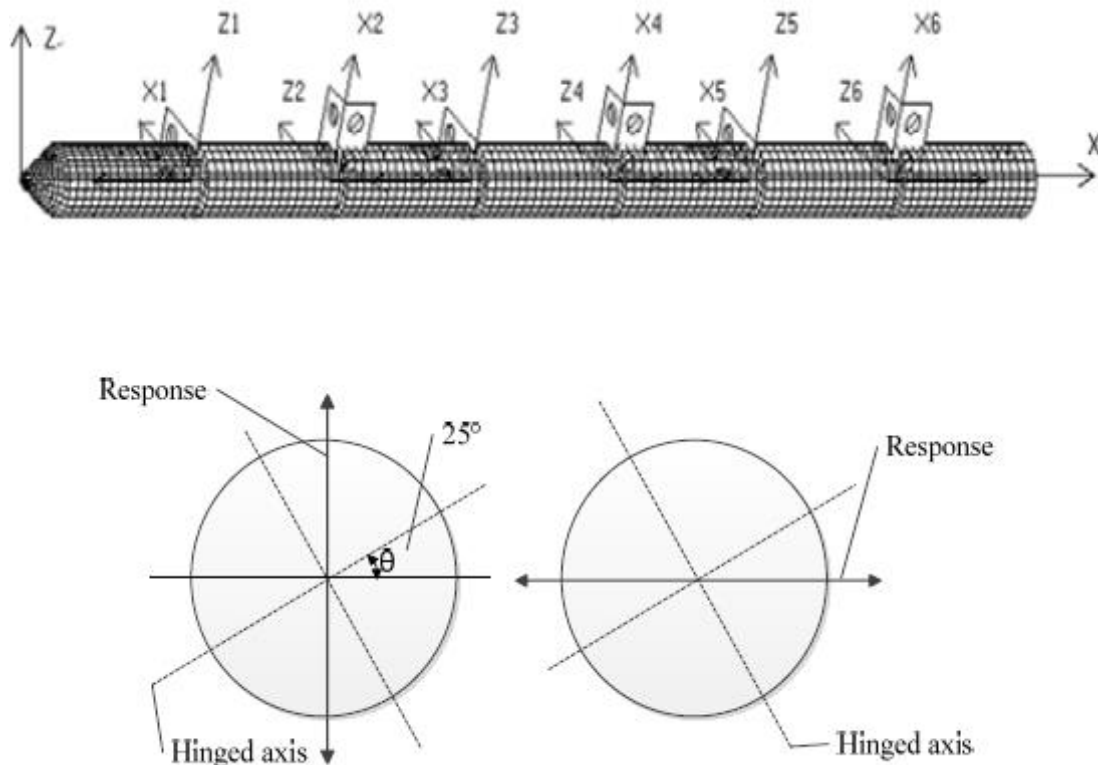
Figure 4.1 Global and Hinge Coordinate systems of the Pelamis benchmark design [30]

Table 4.1 Characteristics of the benchmark Pelamis device [30]

Number of floating bodies	7
Spacing between floating bodies	0.6 (m)
Length of a single floating body	9 (m)
Diameter of cylinders	3.5 (m)
Diameter of front end	0.35 (m)
Draft	2.1 (m)
Total volume	606 (m^3)
Total weight of the device	377.9 (t)
Height of centre of gravity from base	1.75 (m)
Hinge Stiffness coefficient	4.49E6 (N.m/rad)
Hinge Damping coefficient	2.25E7 (N.m/rad/s)
Total Damping coefficient	1.35E8 (N.m/rad/s)
Water depth	37 (m)
Mooring line stiffness	2E6 (N/m)

Taut mooring is used and details of the mooring configuration is shown in Figure 4.2.
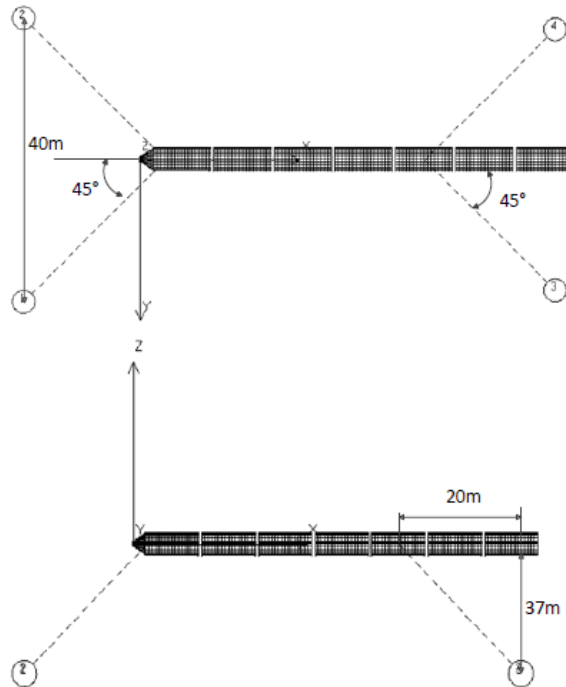
Figure 4.2 Details of Pelamis' mooring configuration [30]

33

4.1.2 Wave site

The design wave site of Pelamis in [30] is Zhejiang province in China which is used for Wavergy as well. The scatter diagram of this site is given in Table 4.2. In the simulations, the wave spectrum for each sea state is represented by a JONSWAP spectrum and is assumed to be unidirectional along the device's length in the positive global x-direction for both Pelamis and Wavergy.

Table 4.2 Pelamis design wave site sea states probability distribution (%) [30]

$T_p(s)$ / $H_s(m)$	5	5.5	6	6.5	7	7.5
0.5	2.05	1.64	0.07	0	0	0
1	1.71	28.89	14.41	0.68	0	0
1.5	0	8.67	20.36	2.94	0.61	0
2	0	0	9.08	3.28	0.34	0
2.5	0	0	0	2.66	0.41	0
3	0	0	0	0.61	0.75	0.14
3.5	0	0	0	0	0.07	0.07
4	0	0	0	0	0.14	0.07
4.5	0	0	0	0	0	0.14

4.2 Modelling Wavergy

In order to reduce computational costs, which are mainly due to the hydrodynamic Diffraction/ Radiation analyses, modelling Wavergy is performed in two stages. The first stage involves modelling only a single energy converting module connected to two submerged fixed points to investigate the effect of the geometric attributes of the device on its power absorption capability. The second stage, full modular configurations that are moored to seabed are modelled and the effects of the size of a single module, longitudinal spacing and transverse spacing between modules are investigated.

4.2.1 Single module modelling

A single Wavergy module consists of a surface piercing elliptical cylinder float connected to two submerged fixed points as shown in Figure 4.3. Two sets of connecting rods that are set not to interact hydrodynamically with the float are used to connect the float to the fixed points. Each connecting rod is attached at the sea level to the float via a hinged joint and since ANSYS AQWA does not allow redundancies in closed loop articulations, one connecting rod is attached to one submerged fixed point with a ball socket joint and the other connecting rod is attached to the second submerged fixed point using a universal joint with its local axes positioned as illustrated in Figure 4.4.
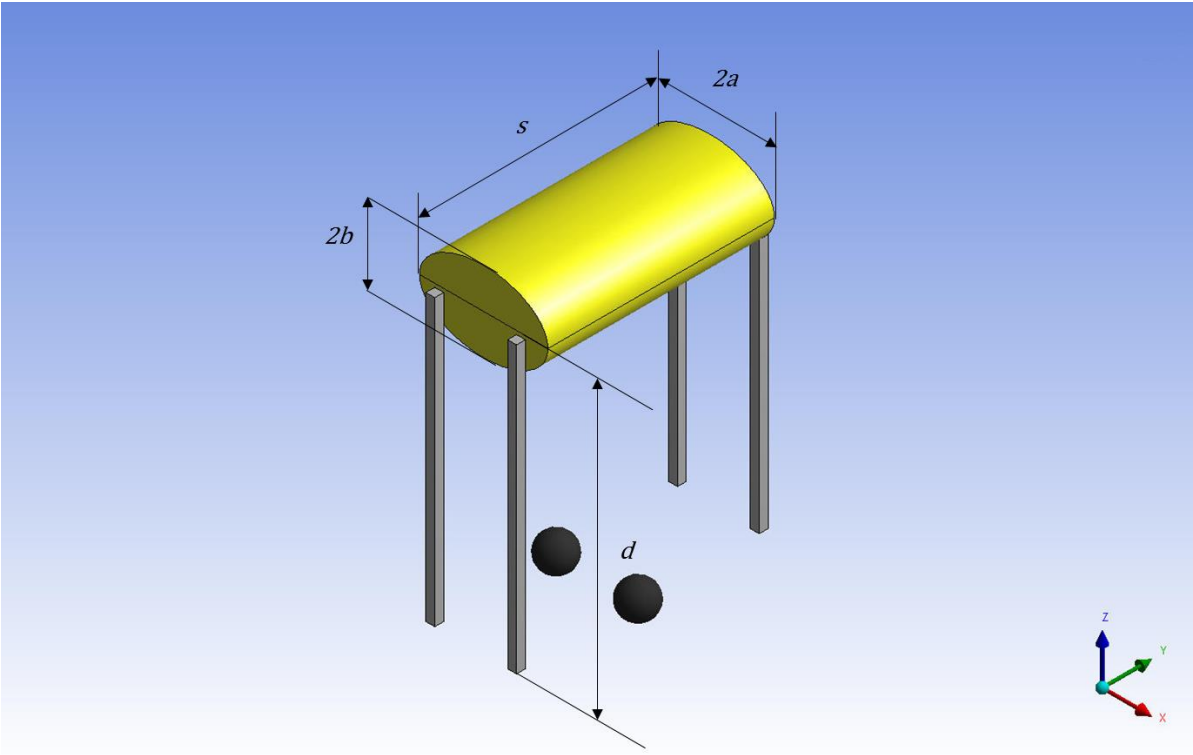
Figure 4.3 Single module Parameters
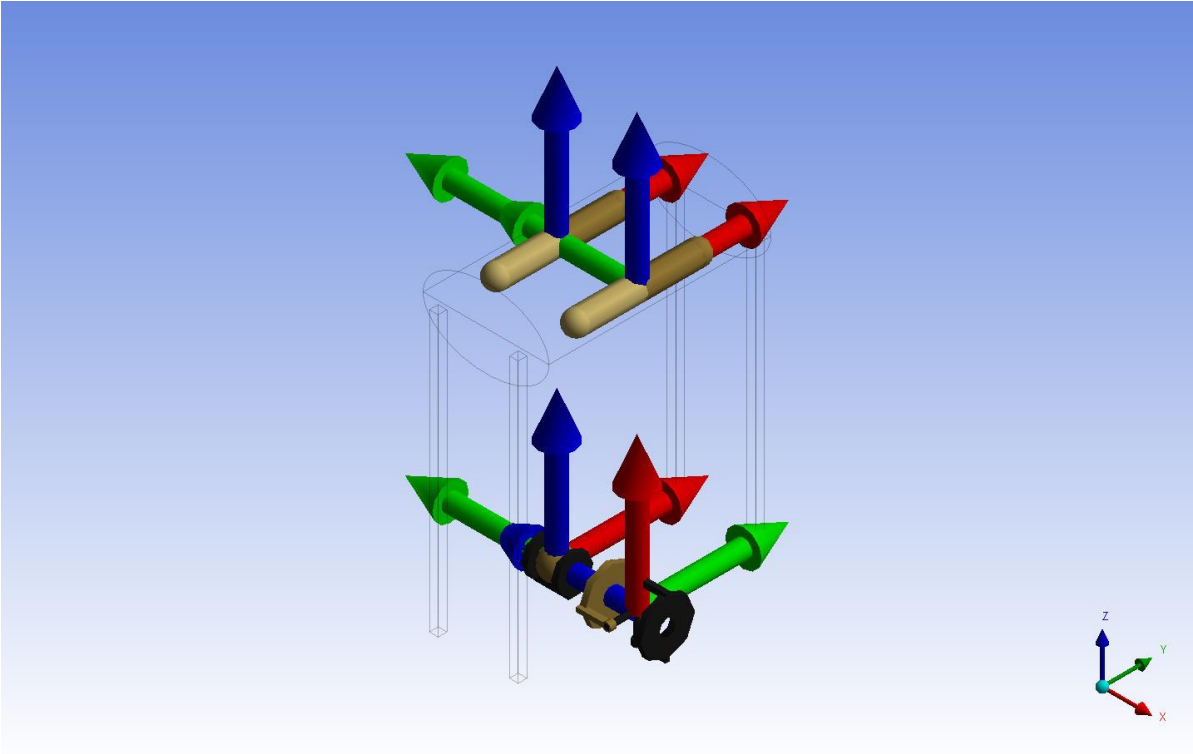
Figure 4.4 Single module joint loop

As previously mentioned, the Wavergy device has the same total volume and total PTO damping coefficient as the benchmark Pelamis device given in Table 4.1, consequently, a single module's volume and damping coefficient values are simply their total values divided by the number of modules (N) in the full modular configuration. The ranges and values of input and derived variables are given in Table 4.3.

Table 4.3 Wavergy single module input parameters

Parameter	Value
Total Number of Modules in full configuration (N)	15, 21, 27
Major semi-axis (a)	1 - 4 (m)
Axis ratio (b/a)	0.25 - 1
Transverse Span (s)	$\dfrac{\text{Total Benchmark volume}}{\pi abN}$ (m)
Submergence depth of fixed points (d)	$3 - 24$ (m)
Single hinged joint damping coefficient (B_{pto})	$\dfrac{\text{Total Benchmark Damping coeff.}}{2N}$ $\left(\dfrac{\text{N.m}}{\text{rad/s}}\right)$

4.2.2 Modular configuration modelling

A modular configuration of Wavergy consists of two layers (or blankets) of staggered arrangement of elliptical cylinders connected with vertical connection bars as shown in Figure 4.5. The upper blanket oscillates mainly in surge relative to the lower blanket which is moored to seabed via taut mooring configuration.
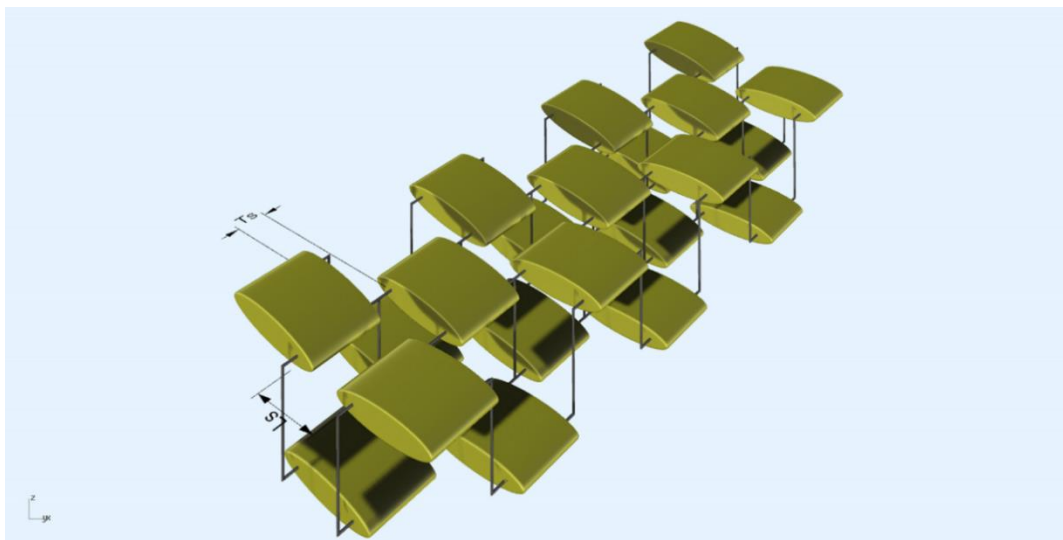
Figure 4.5 A conceptual 3D view of Wavergy WEC staggered arrangement

36

ANSYS AQWA has a maximum limit of 20 hydrodynamically interacting bodies. This means that modelling every single module as a separate hydrodynamic body is impossible. To work around this problem, Wavergy is modelled so that each row of modules is considered as one body. This is justified by the fact that every row acts as a rigid body due to the articulation arrangement illustrated in Figure 4.5. Consequently, a full modular configuration would consist of 6 hydrodynamically interacting bodies (3 rows forming the upper blanket and 3 rows forming the lower blanket) and 4 hydrodynamically transparent connecting bodies to substitute the connecting bars as shown in Figure 4.6. This arrangement allows the reduction of connections to only 12 joints (2 joints or joint lines per each row of modules). Each joint connects a row to a connecting body so that every 2 joints of an upper module row forms a loop with the 2 joints of the corresponding lower module row. For example, Joint lines 1 and 2 which connect the forward upper module row to connection bodies 1 and 2 respectively forms a loop with Joint lines 7 and 8 which connect the lower forward module row to connecting bodies 1 and 2 respectively. In order to avoid redundancies in constrained degrees of freedom, Joints 1 through 6 are hinged joints (with the hinge axis aligned with the global x-axis) and Joints 7 through 12 alternate between universal joints (with the constrained axis of rotation aligned with the global z-axis) and ball and socket joints.
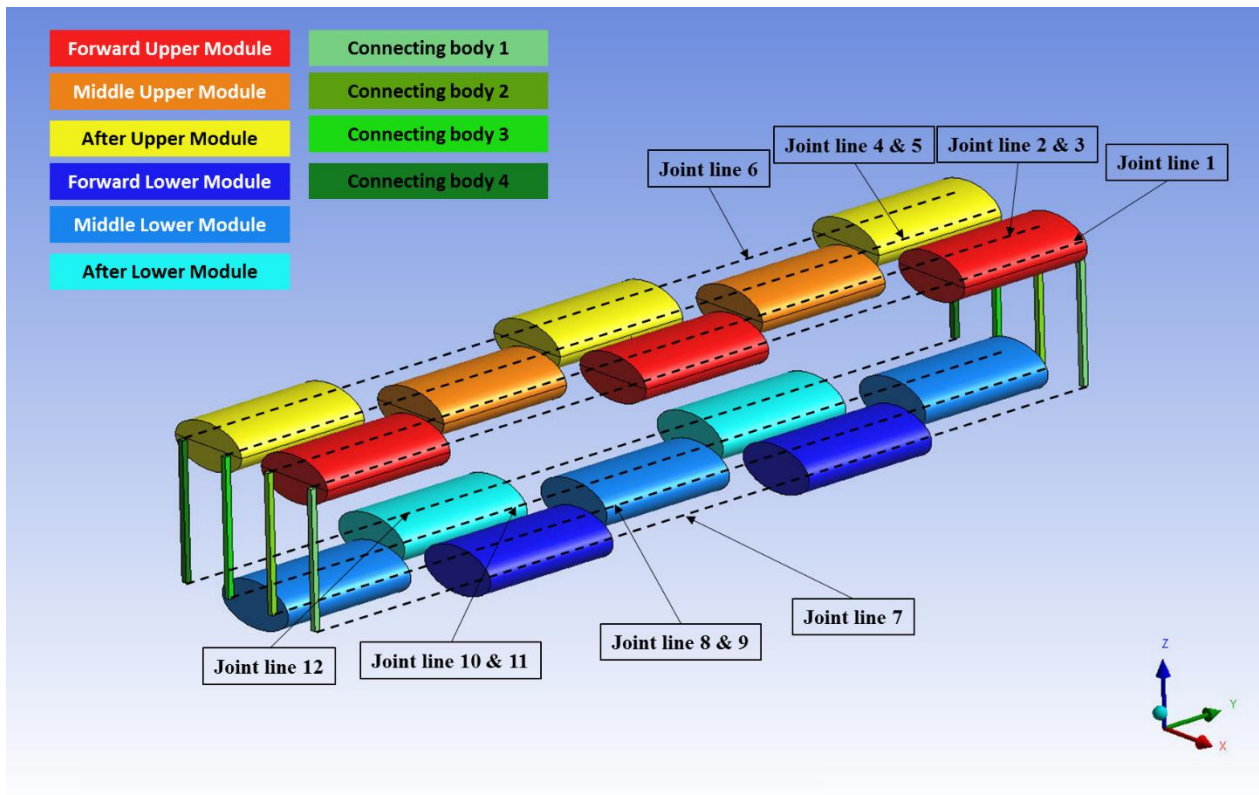
Figure 4.6 Full Modular configuration Wavergy Model with 15 modules

The mooring arrangement of Wavergy is shown in Figure 4.7, where 12 taut mooring lines with four fixed anchoring points are used to keep the device in place and to prevent the modules from overlapping due to pitch motion. Each module row has 4 mooring lines connected to the port and starboard extremities as illustrated in Figure 4.7. Taut mooring lines typically meet the seabed at an angle of 30° to 45° [45], hence, the seabed anchoring points are arranged so that the maximum angle of the mooring lines with sea bed is 45°. The linear stiffness of the mooring lines used in the simulations is the same as that of the benchmark device given in Table 4.1.
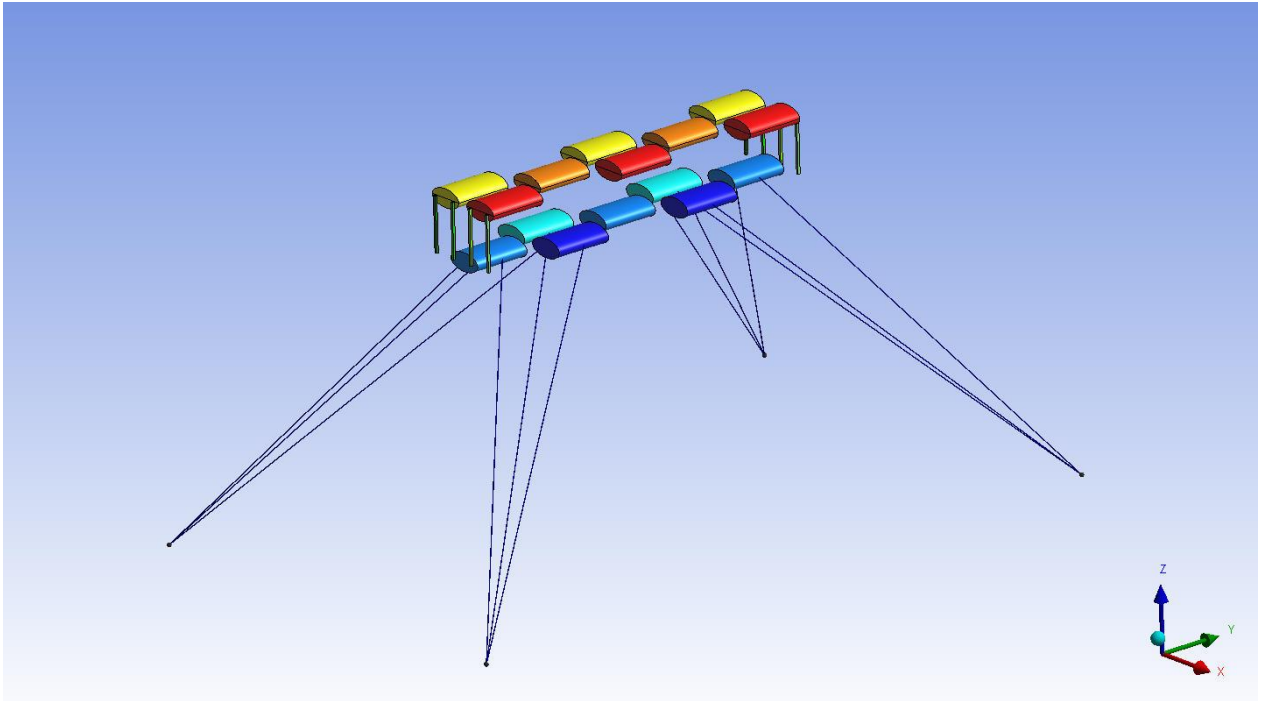
Figure 4.7 Wavergy Mooring Arrangement

Parameters of the Wavergy modular configuration is given in Table 4.4, the total joint damping coefficient is distributed among the joints according to the number of modules every joint line passes through. The geometrical parameters of the elliptical cylinders are taken from the previous single module analysis results. The weight of each single module is equivalent to half the total weight of water displaced by its volume and the radii of gyration are calculated for elliptical cylinders assuming homogeneous mass distribution.

Table 4.4 Wavergy modular configuration input parameters

Parameter	Value
Total Number of Modules in full configuration (N)	15, 21, 27
Longitudinal joint spacing to major axis ratio ($L_s/2a$)	0.55 - 0.95
Minimum transverse spacing between modules to span ratio (T_s/s)	0.1 – 0.5
Submergence depth of Lower blanket (d)	3 – 18 m
Joint damping coefficient about global y-axis (B_{pto}) - for joints (1,2,5,6,9,10)	$\dfrac{\text{Total Benchmark Damping coeff.}}{2N} * \dfrac{N+3}{6} \ (\dfrac{\text{N.m}}{\text{rad/s}})$
Joint damping coefficient about global y-axis (B_{pto}) - for joints (3,4,7,8,11,12)	$\dfrac{\text{Total Benchmark Damping coeff.}}{2N} * \dfrac{N-3}{6} \ (\dfrac{\text{N.m}}{\text{rad/s}})$

4.3 Responses and Power calculations for Wavergy

To calculate the mean absorbed power, the responses of Wavergy are evaluated using frequency domain statistical analysis of articulated structures.

4.3.1 Equation of motion for articulated structures

Ansys AQWA allows four types of articulated joints between structures namely: fixed joints, hinged joints, universal joints and ball and socket joints [42]. If $\vec{X}_{gj}$ and $\vec{X}_{gk}$ are the locations of the centres of gravity of the two connected bodies j and k respectively and $\vec{X}_p$ is the location of the connection point between the two bodies in the global axis system then the relative position vectors between the connection point and the centres of gravity of bodies j and k are given by:

$$\vec{r}_j = \vec{X}_p - \vec{X}_{gj} = (x_j, y_j, z_j) \tag{4.1}$$

$$\vec{r}_k = \vec{X}_p - \vec{X}_{gk} = (x_k, y_k, z_k) \tag{4.2}$$

Furthermore, if the translational and rotational displacement vectors of the jth *and* k^{th} bodies are denoted as $\mathbf{U_j} = (\vec{u}_j, \vec{\theta}_j)$ and $\mathbf{U_k} = (\vec{u}_k, \vec{\theta}_k)$ respectively and the unit vectors of the local articulation axes are written as:

$$\vec{e}_1 = (e_{11}, e_{12}, e_{13}) \tag{4.3}$$

$$\vec{e}_2 = (e_{21}, e_{22}, e_{23}) \tag{4.4}$$

$$\vec{e}_3 = (e_{31}, e_{32}, e_{33}) \tag{4.5}$$

Then the locked constraint conditions of the fixed joint in local articulation axes frame are:

$$\left(\vec{u}_j + \vec{\theta}_j \times \vec{r}_j\right) \cdot \vec{e}_m = \left(\vec{u}_k + \vec{\theta}_k \times \vec{r}_k\right) \cdot \vec{e}_m \quad ,m=1,3 \tag{4.6}$$

$$\vec{\theta}_j \cdot \vec{e}_m = \vec{\theta}_k \cdot \vec{e}_m \quad ,m=1,3 \tag{4.7}$$

Eqs (4.6) and (4.7) can be written in matrix form as:

$$\begin{bmatrix} \mathbf{E^T} & \mathbf{R_j E^T} \\ \mathbf{0} & \mathbf{E^T} \end{bmatrix} \mathbf{U_j} - \begin{bmatrix} \mathbf{E^T} & \mathbf{R_k E^T} \\ \mathbf{0} & \mathbf{E^T} \end{bmatrix} \mathbf{U_k} = 0 \tag{4.8}$$

where:

$$\mathbf{E} = \begin{bmatrix} e_{11} & e_{12} & e_{13} \\ e_{21} & e_{22} & e_{23} \\ e_{31} & e_{32} & e_{33} \end{bmatrix} \tag{4.9}$$

$$R_j = \begin{bmatrix} 0 & z_j & -y_j \\ -z_j & 0 & x_j \\ y_j & -x_j & 0 \end{bmatrix} \tag{4.10}$$

$$R_k = \begin{bmatrix} 0 & z_k & -y_k \\ -z_k & 0 & x_k \\ y_k & -x_k & 0 \end{bmatrix} \tag{4.11}$$

For other joint types Eq. (4.8) is written in the general form:

$$\begin{bmatrix} E^T & R_j E^T \\ 0 & G^T \end{bmatrix} U_j - \begin{bmatrix} E^T & R_k E^T \\ 0 & G^T \end{bmatrix} U_k = 0 \tag{4.12}$$

where **G** determines the type of the articulation joints as given below:

$$G = \begin{bmatrix} 0 & e_{12} & e_{13} \\ 0 & e_{22} & e_{23} \\ 0 & e_{32} & e_{33} \end{bmatrix}, for\ hinged\ joints \tag{4.13}$$

$$G = \begin{bmatrix} 0 & 0 & e_{13} \\ 0 & 0 & e_{23} \\ 0 & 0 & e_{33} \end{bmatrix}, for\ universal\ joints \tag{4.14}$$

$$G = \begin{bmatrix} 0 & 0 & 0 \\ 0 & 0 & 0 \\ 0 & 0 & 0 \end{bmatrix}, for\ ball\ and\ socket\ joints \tag{4.15}$$

Rewriting Eq (4.12) for simplicity:

$$L_j U_j - L_k U_k = 0 \tag{4.16}$$

Finally, if the reaction forces acting on the jth body at the connection point is denoted as F_R the equation of motion for two connected bodies become:

$$\begin{bmatrix} Z_{jj} & Z_{jk} & -L_j^T \\ Z_{kj} & Z_{kk} & L_k^T \\ L_j & L_k & 0 \end{bmatrix} \begin{bmatrix} U_j \\ U_k \\ F_R \end{bmatrix} = \begin{bmatrix} F_j \\ F_k \\ 0 \end{bmatrix} \tag{4.17}$$

40

where $\begin{bmatrix} Z_{jj} & Z_{jk} \\ Z_{kj} & Z_{kk} \end{bmatrix}$ is the total impedance matrix including the inertial, hydrodynamic and hydrostatic coefficients of the two bodies and $\mathbf{F_j}$ and $\mathbf{F_k}$ are the forces and moments acting of the jth and k^{th} bodies respectively without the reaction forces.

4.3.2 Frequency-domain statistical analysis for a WEC in irregular waves

Recall Eq. (3.40) which gives the Response amplitude operators (RAOs) for a WEC in regular waves, this equation can be rewritten to take the following form:

$$\mathbf{U} = \frac{\hat{\boldsymbol{\xi}}}{\zeta_a} = \mathbf{H}\hat{\mathbf{f}}_\mathbf{e} \tag{4.18}$$

where $\mathbf{U}$ is the motion amplitude response vector to a unit amplitude regular wave (RAO) and $\mathbf{H}$ is the reciprocal of the impedance matrix and is given as:

$$\mathbf{H} = [-\omega^2(\mathbf{M} + \mathbf{A}) + i\omega(\mathbf{B} + \mathbf{B_{PTO}}) + \mathbf{C} + \mathbf{C_{PTO}} + \mathbf{C_m}]^{-1} \tag{4.19}$$

For unidirectional waves, the motion response spectral density is given by:

$$S_{U_j}(\omega) = S_{wm}(\omega)|U_j|^2 \ , where \ j = 1,6 \tag{4.20}$$

Similarly, for relative translational motion between two structures (or any two specified nodes in general the motion response spectral density is:

$$S_{u_{rj}}(\omega) = S_{wm}(\omega)|u_{rj}|^2 \ , where \ j = 1,3 \tag{4.21}$$

where u_{rj} is the relative motion response in the global axes and is given as:

$$u_{rj} = [u_{nj}(\omega, \vec{X}_{n1}) - u_{nj}(\omega, \vec{X}_{n2})] \ , where \ j = 1,3 \tag{4.22}$$

where $u_{nj}(\omega, \vec{X}_{n1})$ and $u_{nj}(\omega, \vec{X}_{n2})$ are the nodal motion responses of nodes $\vec{X}_{n1}$ and $\vec{X}_{n2}$.

ANSYS AQWA outputs the significant amplitudes of responses and forces as:

$$R_s = 2\sqrt{m_0} \tag{4.23}$$

where $m_0 = \int_0^\infty S_R(\omega)d\omega$, and S_R is the response or force spectral density. In order to calculate the average value from the significant amplitude [30]:

$$Mean \ response \ or \ force \ value = 1.25\sqrt{m_0} = 0.625R_s \tag{4.24}$$

The mean response values are used to calculate the mean power for each sea state as illustrated in the next subsection.

4.3.3 Power calculation for Wavergy

The power absorbed by a single joint of Wavergy can be calculated by using the following equation:

$$P = B_{PTO}\dot{\theta}^2 \qquad (4.25)$$

where B_{PTO} is the hinge rotational damping about the global y-axis and $\dot{\theta}$ is relative rotational speed between the energy converting module and the connection rod. Each row of upper modules forms an articulation loop with the corresponding row of lower modules as shown in Figure 4.8.
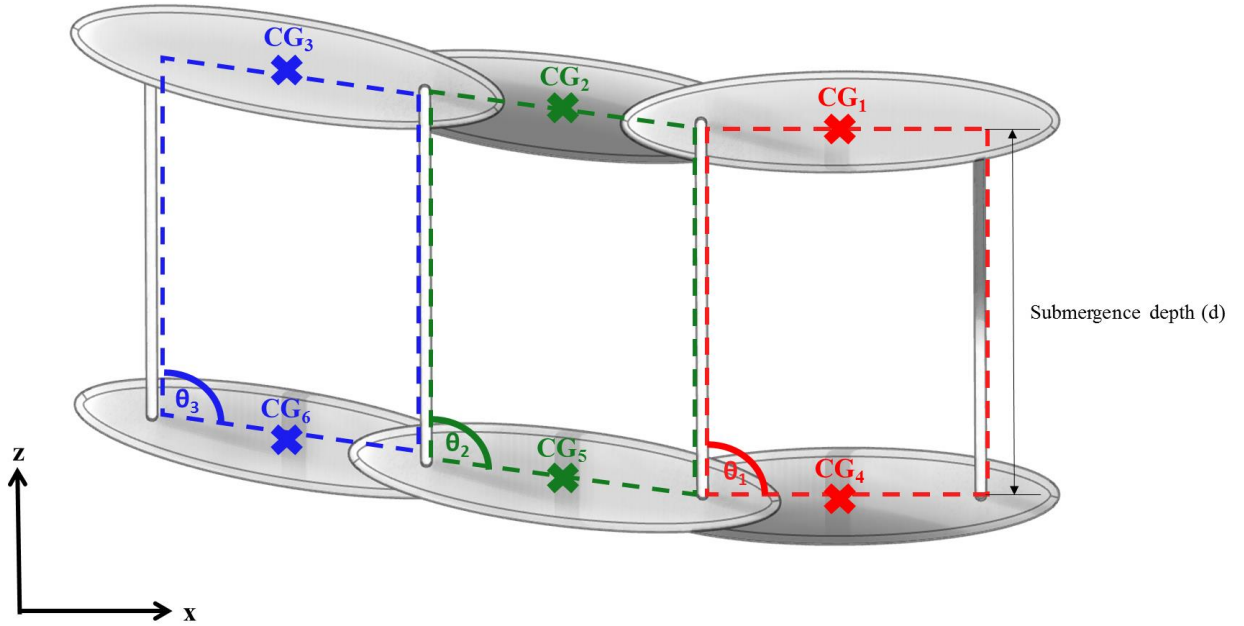
Figure 4.8 Illustration of Wavergy Articulation loop

Each loop keeps a parallelogram shape as illustrated in Figure 4.9 where:

$$d = \sqrt{x_r^2 + z_r^2} \qquad (4.26)$$

$$\cos(\theta + \alpha) = \frac{x_r}{d} \qquad (4.27)$$

where x_r and z_r are the relative surge and heave motion displacements between the upper and lower centres of gravity respectively for each articulation loop, d is the submergence depth and α is the pitch angle of both the upper and lower modules, it follows that:

$$\dot{\theta} = \dot{\alpha} - \frac{\dot{x}_r}{d\sqrt{1 - (\frac{x_r}{d})^2}} \qquad (4.28)$$

42
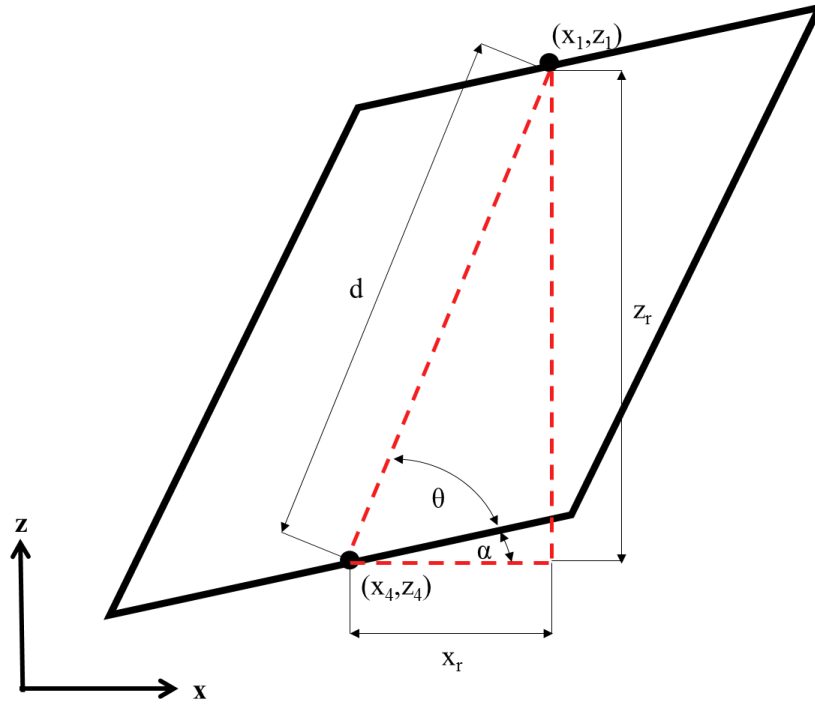
Figure 4.9 Description of the parallelogram motion of a Wavergy articulation loop

Substituting Eq (4.28) into equation Eq (4.25) and assuming small amplitude motion where the relative surge displacement x_r is much smaller than the submergence depth d, then the absorbed power at a single connection point is given by:

$$P = B_{PTO}\left(\dot{\alpha} - \frac{\dot{x}_r}{d}\right)^2 \qquad (4.29)$$

Hence, the total power absorbed by Wavergy is the sum of absorbed power by all six joints. The mean absorbed power from each sea state can then be calculated using the following formula:

$$\bar{P}_{SS} = B_{PTO}\left(\bar{\dot{\alpha}} - \frac{\overline{\dot{x}_r}}{d}\right)^2 \qquad (4.30)$$

where the mean values for the motion responses are evaluated from the aforementioned frequency domain statistical analysis. Finally, the mean annual absorbed power is calculated from the probability distribution of the design wave site:

$$\bar{P} = \sum_{ss=1}^{SS} \eta_{ss}\bar{P}_{SS} \qquad (4.31)$$

where η_{ss} is the probability of occurrence of each sea state. The design wave site used for Wavergy is the one used for the benchmark device and for power calculation only ten sea states with the highest probabilities covering 94% of the time were included.

43

4.4 A comment on the validation of the results

Since the Wavergy device is a novel concept there are no available experimental data or published results to validate the results obtained by the methodology described in this chapter and presented in the next chapter.

Nevertheless, by using a benchmark device with a proven wave energy conversion concept as a guide in the optimisation process and making comparisons with published results for other wave energy converters with various working principles helped put the results obtained for the Wavergy device into context.

Chapter 5 : Results and Discussion

In this chapter, the results of the numerical simulations following the modelling procedure outlined in the previous chapter are presented. In the first section, the performance results of a single surface piercing module of the Wavergy device are reviewed to choose suitable geometric characteristics for the device. The second section uses the results obtained from the single module simulations to model the geometry of the full modular configuration of the Wavergy device. Subsequently, the effects of spacing between modules and the size of individual modules on the power performance are studied and a set of input design parameters are chosen. The results obtained from the frequency-domain statistical analyses in the second section are verified by running time-domain analyses for the chosen Wavergy design in the third section. The fourth section deals with the PTO tuning of the chosen Wavergy design for multiple wave periods to generate the optimal power matrix. Finally, the Wavergy device is compared to a selection of benchmark devices with different working principles in representative wave sites using various performance evaluation measures.

5.1 Single module results

5.1.1 Response surface results

To generate response surfaces, a grid of 80 design points was formulated as illustrated in Figure 5.1. Three parameters were used to define each design point namely: the major semi-axis (a), the axis ratio (b/a) and the submergence depth of fixed points (d). Mean absorbed power and Capture width ratio (CWR) values are evaluated at each design point in the grid and second-degree polynomial surfaces are fitted through these points.

Figures 5.2, 5.3 and 5.4 show the mean absorbed power response surfaces at five different values of (d) for a single module with a total volume equal to the total volume of the full modular configuration (the total volume of the Pelamis benchmark device given in Table 4.1) divided by the number of modules (N), where N = 15, 21 and 27 respectively. Figures 5.5 to 5.7 show the corresponding CWR response surfaces.
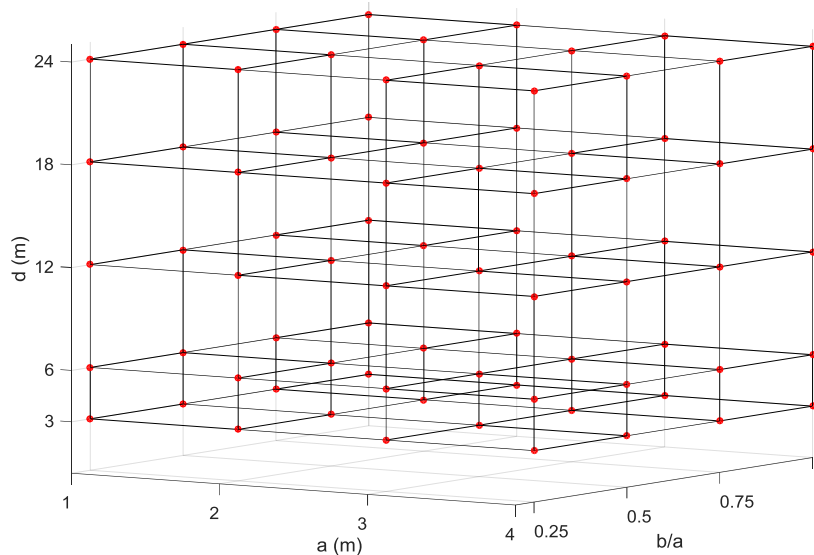
Figure 5.1 Single module response surfaces fitting design grid
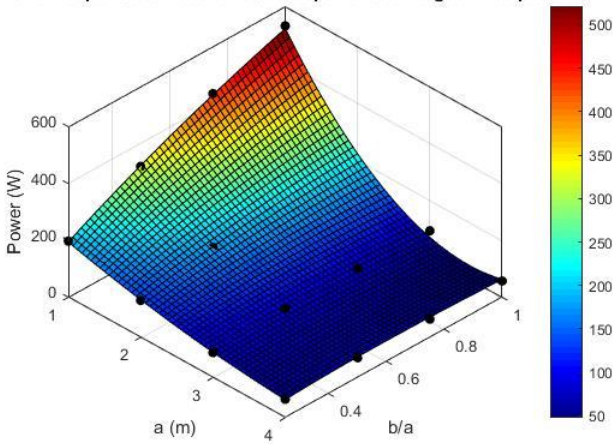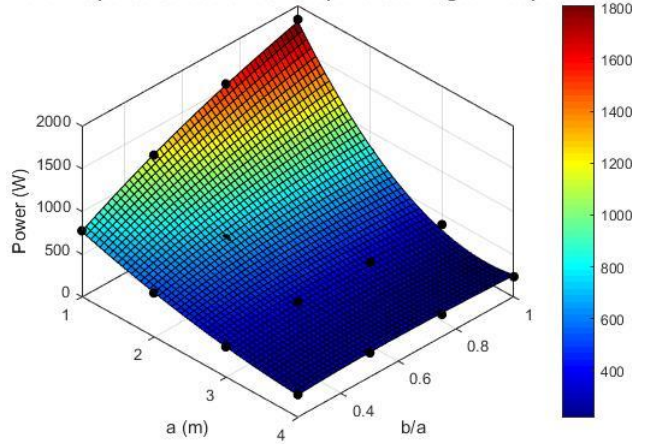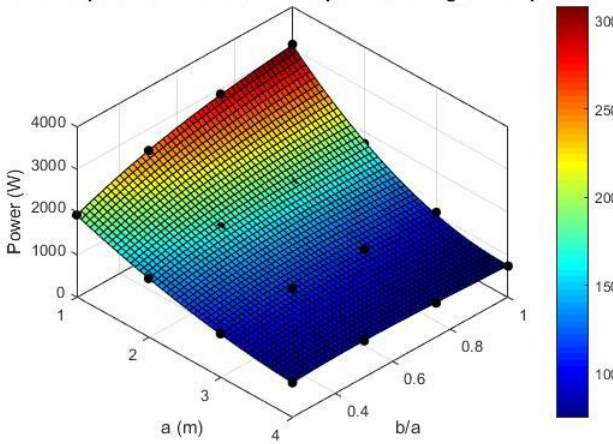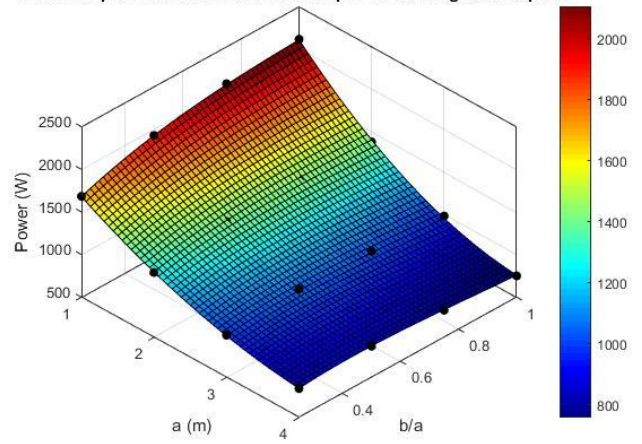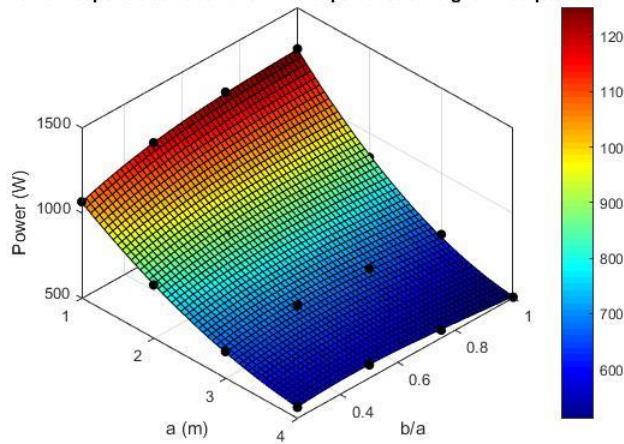
Figure 5.2 Power response surfaces at different values of (*d*) for a single module in a 15 modules configuration (black dots represent the fitting points from the design points runs)
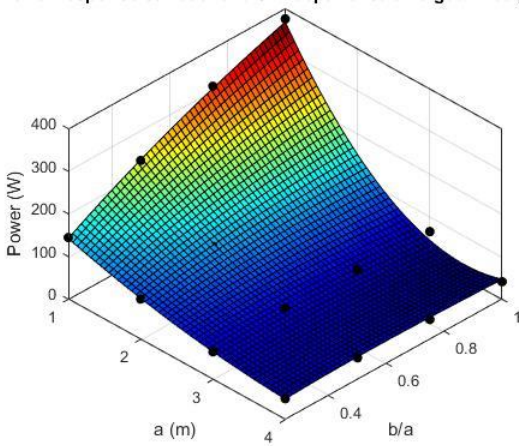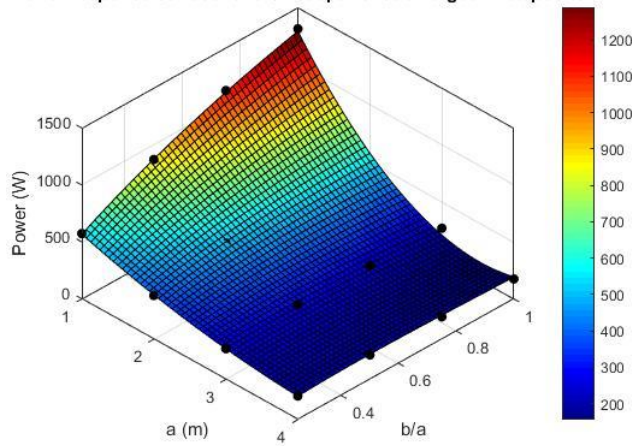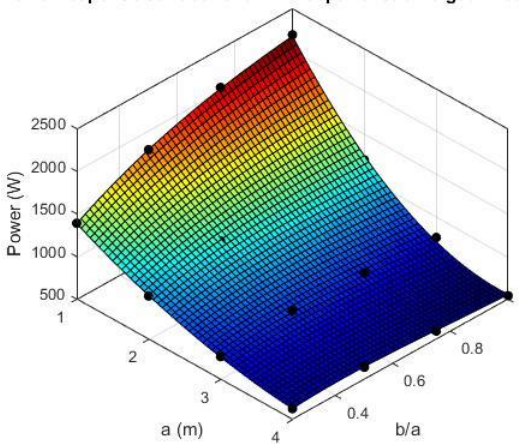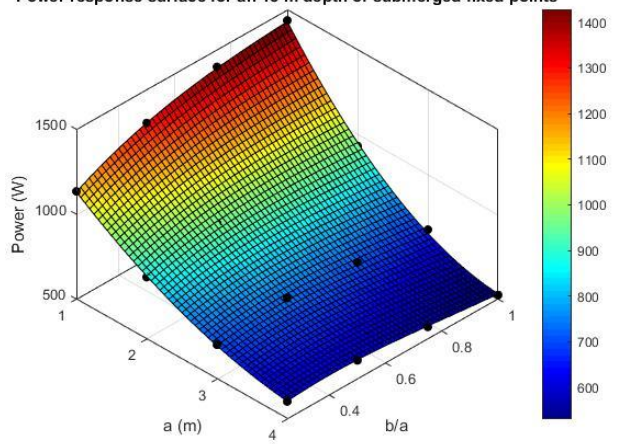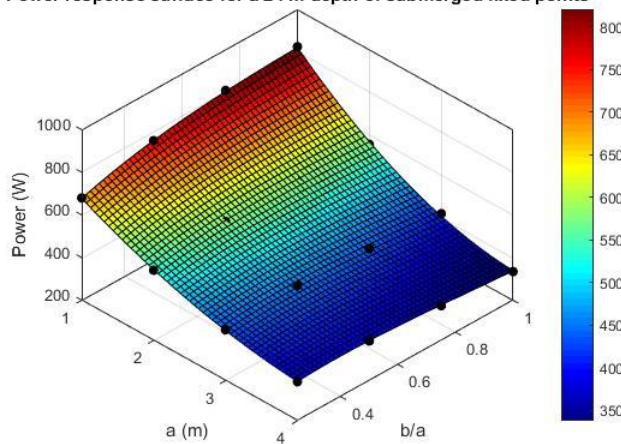
Figure 5.3 Power response surfaces at different values of (*d*) for a single module in a 21 modules configuration (black dots represent the fitting points from the design points runs)
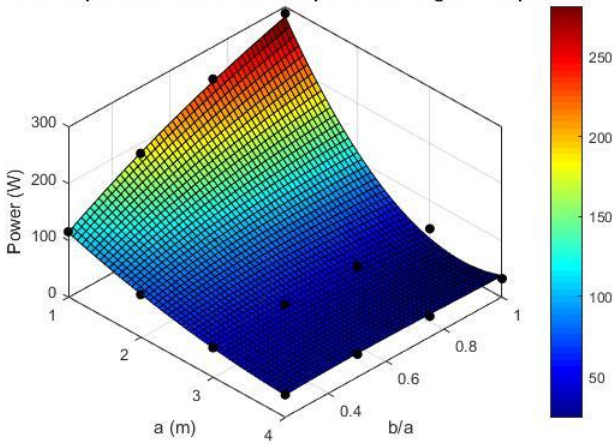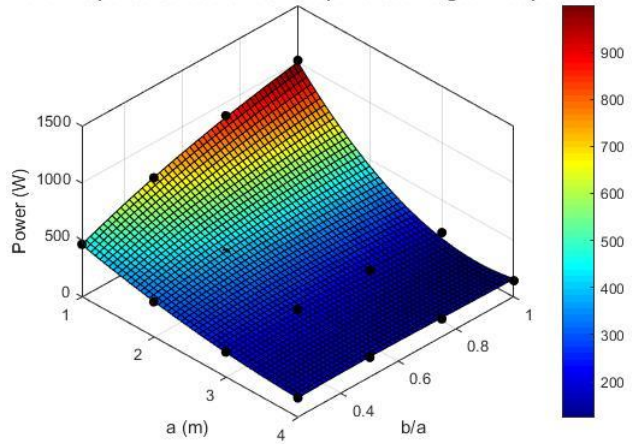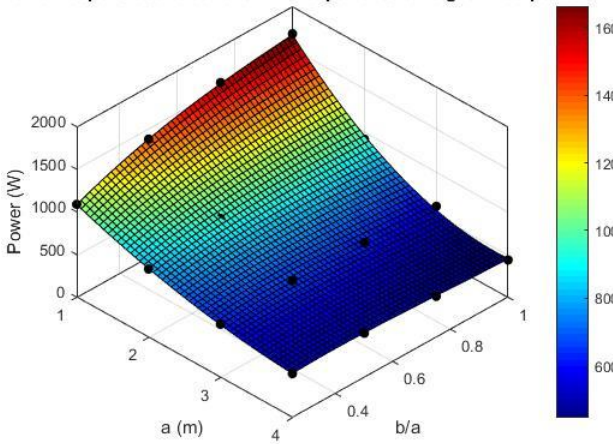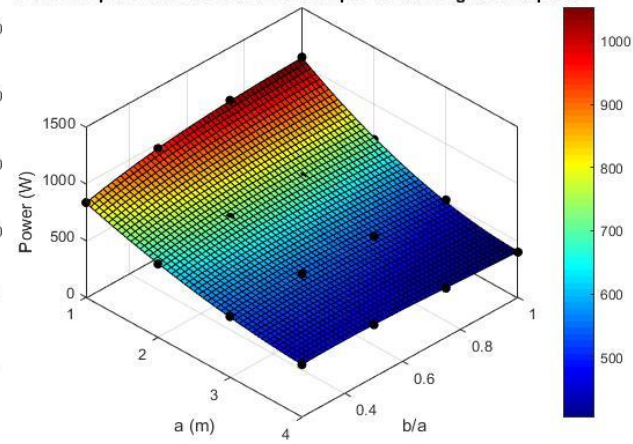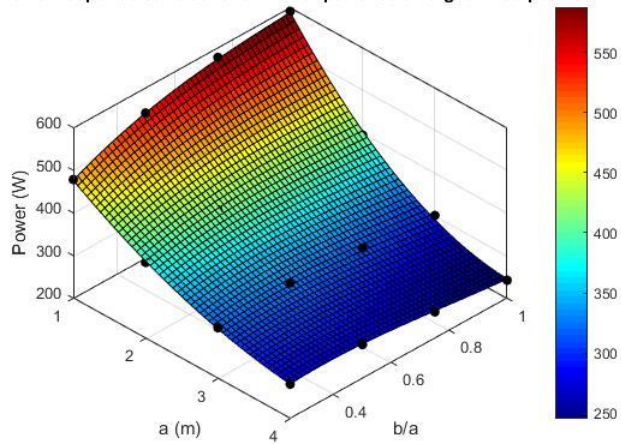
Figure 5.4 Power response surfaces at different values of (*d*) for a single module in a 27 modules configuration (black dots represent the fitting points from the design points runs)
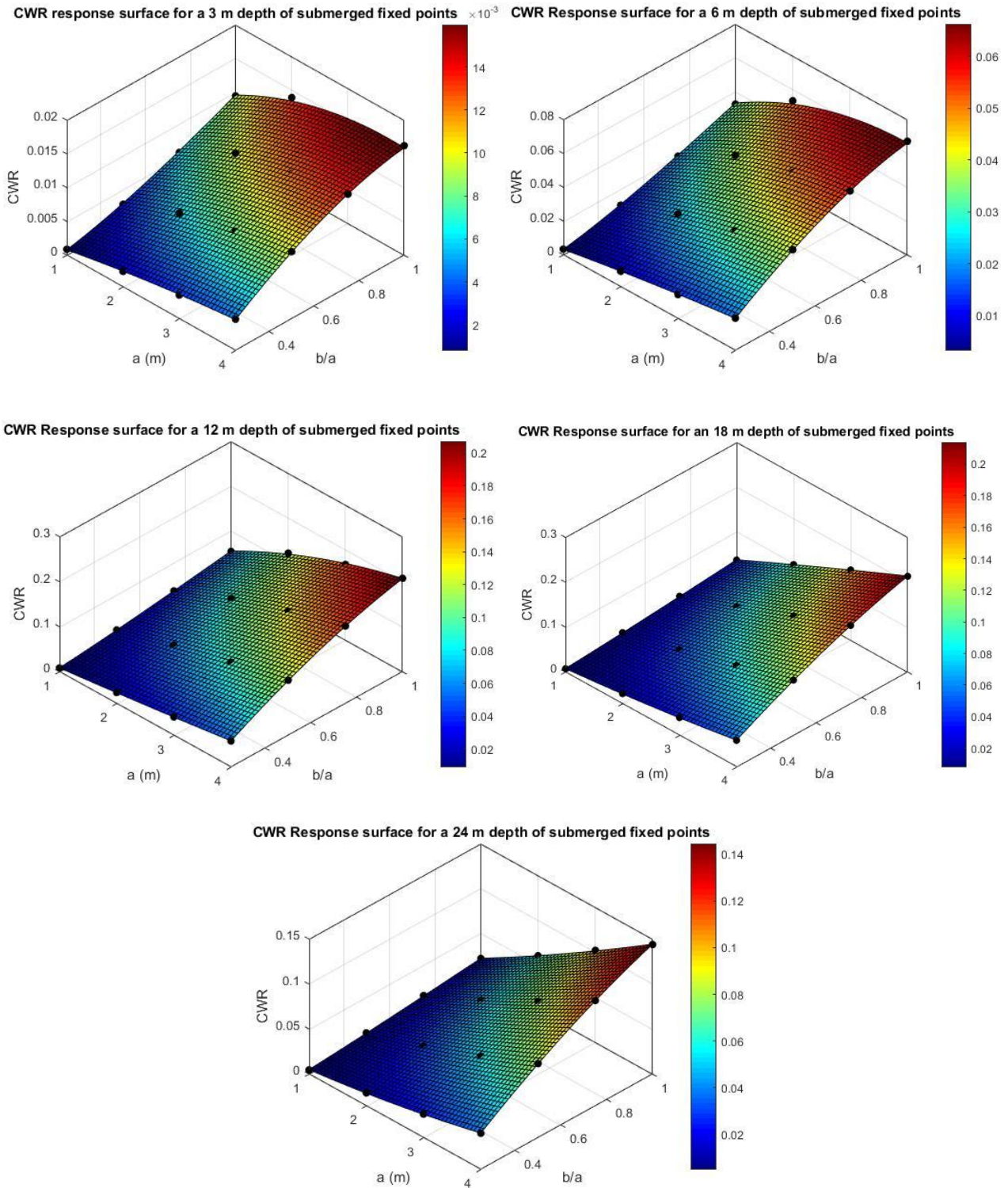
Figure 5.5 CWR response surfaces at different values of (*d*) for a single module in a 15 modules configuration (black dots represent the fitting points from the design points runs)
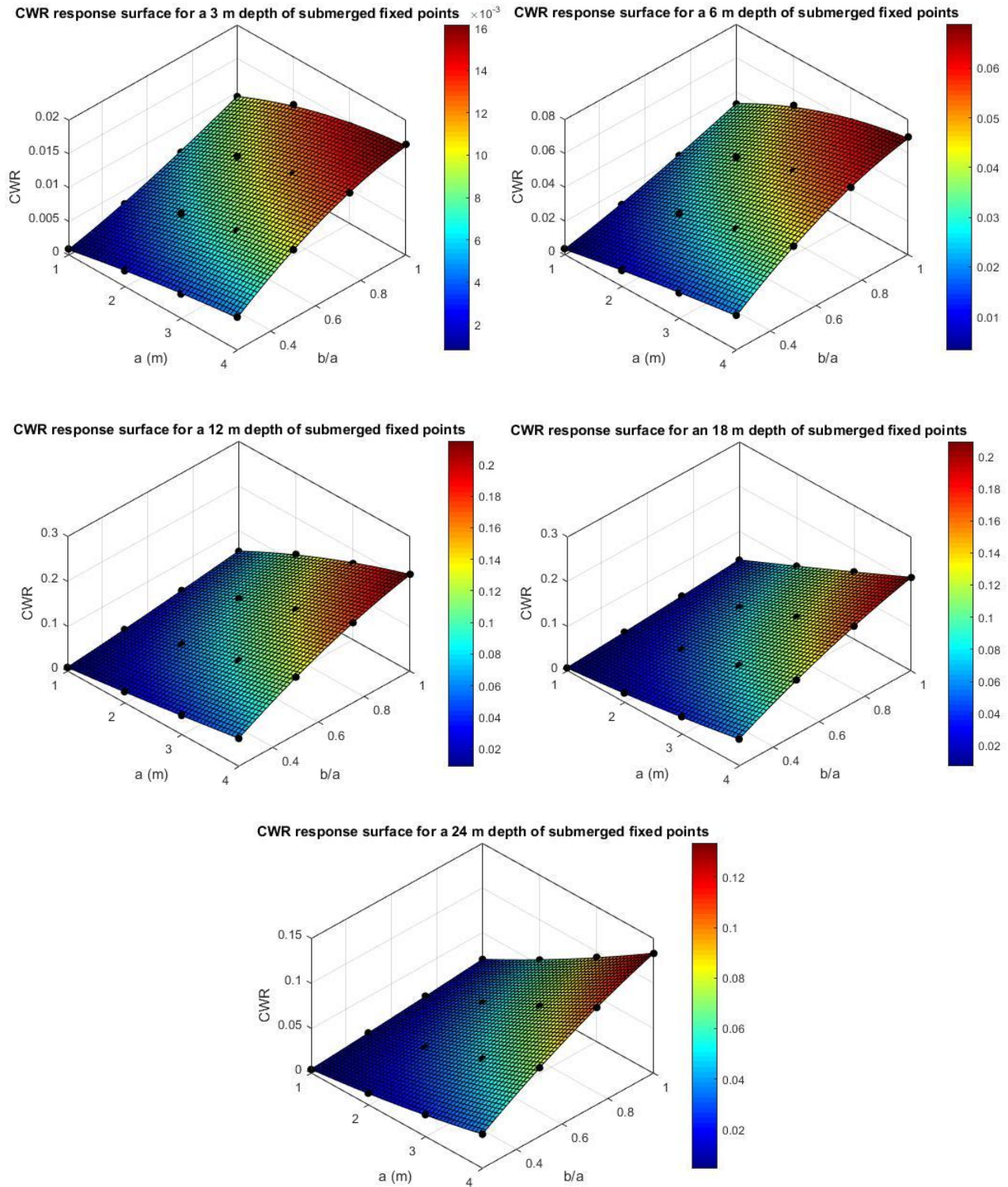
Figure 5.6 CWR response surfaces at different values of (*d*) for a single module in a 21 modules configuration (black dots represent the fitting points from the design points runs)

50
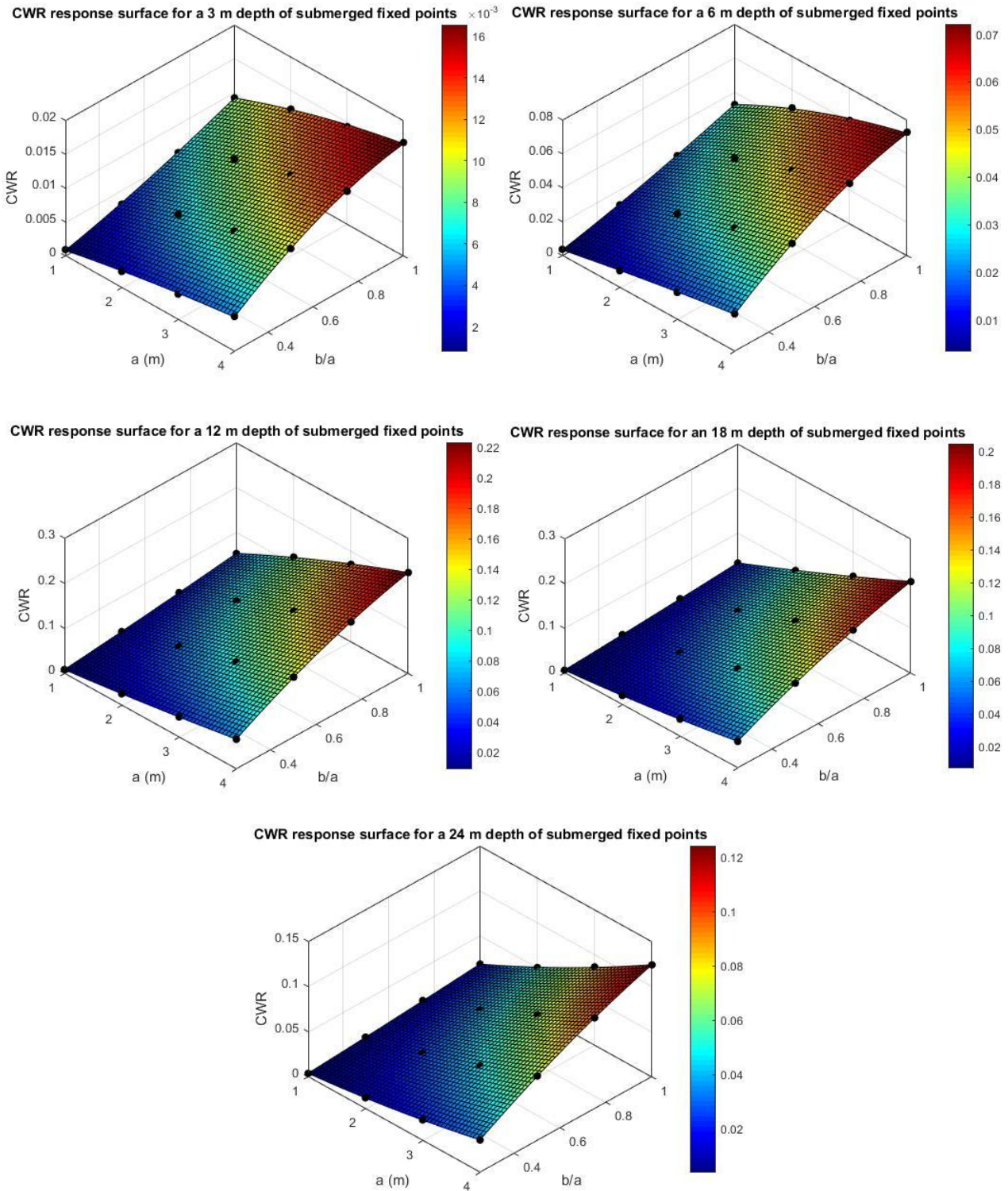
Figure 5.7 CWR response surfaces at different values of (*d*) for a single module in a 27 modules configuration (black dots represent the fitting points from the design points runs)

The mean absorbed power results in Figures 5.2 to 5.4 demonstrate four general trends in all of the three sizes of the single module of the Wavergy device. The first trend is that for maximum mean absorbed power the device favours larger projected lateral area (normal to wave propagation direction). Thus, it tends to maximize the span and the axis ratio while minimizing the major axis. Secondly, the mean absorbed power increases with the depth of submerged fixed points until it reaches a certain value and then starts decreasing for larger submergence depths. Thirdly, the mean absorbed power values increase with the size of the single module. Hence, the single module in a 15-module configuration gives the largest power results. Lastly, the curvature of the response surfaces in the direction of (b/a) decreases with increasing submergence depth of fixed points, meaning that when the depth of submerged fixed points increases the power performance of lower (b/a) values becomes increasingly better compared to the larger (b/a) values at the same submergence depth. The design point with the maximum mean absorbed power is roughly the same for all three sizes with the minimum value of (a) of 1 m, the maximum value of the (b/a) of 1 and a value of (d) of 12 m implying that there is an optimum submergence depth of fixed points close to this value.

Capture width ratios were calculated for the design wave site described in Table 4.2 with only the 10 sea states with the highest probability of occurrence covering 94% of the time and giving a power flux of about 4.37 kW/m. Eq (3.51) shows that to maximize *CWR* for a specific wave site the power has to be maximized and the active width has to be minimized. These two objectives are contradicting as reflected by the *CWR* response surfaces shown in Figures 5.5 to 5.7 where the maximum *CWR* occurs at the maximum (a) and (b/a) values, i.e., the maximum lateral projected area at the minimum span value. Similar to the power results, the maximum value of the *CWR* occurs at the same design point for all of the three sizes with maximum (a) value of 4 m and maximum (b/a) value of 1 and a value of (d) of 12 m. However, unlike the power results, different sizes give similar *CWR* values ranging from about 0.001 to 0.22. The calculated values of *CWR* of the Wavergy device, show agreement with the values of *CWR* of floating oscillating wave surge converters given in [31] which were obtained from the published results of 12 floating OWSC devices and ranged from 0.07 to 0.25.

5.1.2 Optimisation results

In light of the response surface results, optimising the device's geometry by simply choosing the geometry that delivers the maximum mean absorbed power would result in a high aspect ratio cylinder with its axis perpendicular to the wave propagation direction. This configuration will have very low *CWR* and poor stability due to large span and axis ratio and may also be problematic for the arrangement of the internal power take-off equipment. To avoid these problems an additional optimisation objective (in addition to maximizing mean absorbed power) and a constraint were implemented on the optimisation runs. The additional objective is to minimize (b/a) in order to improve the stability of the device. In addition to the this objective, a constraint was imposed on the minimum value of *CWR*, this value was obtained from [31] where the data analysed for 12 floating OWSCs resulted in a fitting line of *CWR* as a function of the active width of the devices with a constant *CWR* value of 0.085 which was used as the lower limit of *CWR* to avoid very large span values.

The response surface optimisation was performed using ANSYS DesignXplorer software and the optimisation scheme used was the screening method. Minimizing (b/a) objective was set to have

lower importance while the mean absorbed power maximization objective was set to have higher importance. The objective importance is determined by weight values assigned to each objective and are multiplied by the normalized objective function to raise or lower the significance of a certain objective. The default value of the weight coefficient is 2/3 this value can be changed to make the objective of lower or higher importance corresponding to weight coefficient values of 1/3 and 1 respectively [46].

The optimisation process was set to generate 20 candidate points for each of the single module sizes (N = 15, 21 and 27) and the results are given in Tables Table 5.1Table 5.3. The results of power and (b/a) are divided into three regions according to the degree to which they satisfy the defined objective, maximizing power and minimizing (b/a). The third with best candidate values is highlighted with green circles, the third with intermediate candidate values is highlighted with yellow triangles and the third with the worst candidate values is highlighted with red diamonds. Candidate points which have yellow triangles for both objectives are considered as a compromise between the objectives, and in particular three similar candidate points show compromise in all of three tables namely candidate point 4 in Table 5.1, candidate point 6 in Table 5.2, and candidate point 3 in Table 5.3. Those three candidate points are chosen for further analyses.

The Screening optimisation method implements a simple sampling and sorting approach which supports multiple objectives and constraints [46]. This method is often used in preliminary design stages. To refine the results and ensure that the chosen design parameter values are the best candidates within the defined constraints an iterative gradient-based optimisation scheme is performed using the results from the screening method as initial values for the input design parameters.

Table 5.1 Response surface optimisation candidate points for N = 15

	a (m)	b/a	d (m)	Power (W)	CWR
Candidate Point 1	1.5595	◆0.965701172	12.1351872	●2130.887676	0.08606238
Candidate Point 2	1.7155	◆0.869021484	13.8635823	●1946.261002	0.08756732
Candidate Point 3	1.9255	▲0.794314453	15.1118676	▲1706.134729	0.09027401
Candidate Point 4	2.2495	▲0.645999023	14.9966413	▲1500.727443	0.09046584
Candidate Point 5	2.4625	●0.571291992	12.3560377	◆1394.679102	0.08797938
Candidate Point 6	1.7635	◆0.904177734	14.9390281	●1842.416165	0.09119335
Candidate Point 7	2.6065	●0.538333008	13.7387538	◆1347.553327	0.0899729
Candidate Point 8	2.3425	▲0.615237305	11.9719499	◆1446.707265	0.08894696
Candidate Point 9	2.3455	▲0.63281543	14.3052833	▲1469.915361	0.0944645
Candidate Point 10	1.8595	◆0.890994141	14.2476701	▲1794.833706	0.09791945
Candidate Point 11	1.7515	◆0.974490234	13.9019911	●1897.274526	0.09898616
Candidate Point 12	2.0215	◆0.811892578	14.1900569	▲1673.788585	0.10003233
Candidate Point 13	1.8235	◆0.943728516	13.2106331	●1850.421283	0.10172423
Candidate Point 14	2.4385	●0.606448242	15.4287401	◆1385.895553	0.09258192
Candidate Point 15	2.9305	●0.489993164	13.8539801	◆1224.596779	0.09235572
Candidate Point 16	2.5585	●0.555911133	11.6646797	◆1313.217501	0.08627695
Candidate Point 17	2.2735	▲0.716311523	12.9225672	▲1520.57171	0.10278466
Candidate Point 18	3.0025	●0.472415039	12.9321694	◆1189.564296	0.08960859
Candidate Point 19	3.2365	●0.429019043	14.1548489	◆1130.705208	0.08903898
Candidate Point 20	2.1775	▲0.698733398	15.918452	▲1495.283436	0.0910306

53

Table 5.2 Response surface optimisation candidate points for *N* = 21

	a (m)	b/a	d (m)	Power (W)	CWR
Candidate Point 1	1.5595	0.965701172	12.1351872	1519.625277	0.0859369
Candidate Point 2	1.7155	0.869021484	13.8635823	1379.605144	0.08609752
Candidate Point 3	1.9255	0.794314453	15.1118676	1200.965129	0.08782277
Candidate Point 4	2.6065	0.538333008	13.7387538	953.9143011	0.08953551
Candidate Point 5	2.4625	0.571291992	12.3560377	984.0959801	0.08842627
Candidate Point 6	2.2495	0.645999023	14.9966413	1055.424439	0.0881576
Candidate Point 7	1.7635	0.904177734	14.9390281	1300.99883	0.08912923
Candidate Point 8	2.3455	0.63281543	14.3052833	1037.203923	0.09284314
Candidate Point 9	2.3425	0.615237305	11.9719499	1019.082546	0.0893477
Candidate Point 10	1.8595	0.890994141	14.2476701	1269.366174	0.09623334
Candidate Point 11	1.7515	0.974490234	13.9019911	1343.863377	0.09778022
Candidate Point 12	1.8235	0.943728516	13.2106331	1311.144924	0.10091272
Candidate Point 13	2.0215	0.811892578	14.1900569	1182.818366	0.09826408
Candidate Point 14	2.9305	0.489993164	13.8539801	873.0746001	0.09264285
Candidate Point 15	3.2365	0.429019043	14.1548489	812.3433039	0.08976192
Candidate Point 16	3.0025	0.472415039	12.9321694	849.0212415	0.09108645
Candidate Point 17	2.4385	0.606448242	15.4287401	975.9725755	0.09019057
Candidate Point 18	2.5585	0.555911133	11.6646797	926.2840457	0.08754961
Candidate Point 19	3.2845	0.411440918	15.5375649	787.7473674	0.08501376
Candidate Point 20	3.1465	0.45538623	13.6235274	828.6558588	0.09284881

Table 5.3 Response surface optimisation candidate points for *N* = 27

	a (m)	b/a	d (m)	Power (W)	CWR
Candidate Point 1	1.5595	0.965701172	12.1351872	1163.300547	0.08503583
Candidate Point 2	1.8775	0.785525391	13.7291516	952.0302213	0.08629999
Candidate Point 3	2.2495	0.645999023	14.9966413	778.4091242	0.08638812
Candidate Point 4	3.0985	0.472964355	12.2408114	644.7275447	0.0946619
Candidate Point 5	3.8845	0.352114746	14.3853016	555.4901382	0.09197505
Candidate Point 6	2.2735	0.716311523	12.9225672	823.4349274	0.10197723
Candidate Point 7	2.4415	0.641604492	11.5398512	767.2065778	0.09734417
Candidate Point 8	2.8825	0.516360352	11.779906	673.1533357	0.09443078
Candidate Point 9	2.1655	0.769045898	12.8073409	859.0666453	0.10259843
Candidate Point 10	2.6785	0.58227832	13.0473957	720.8834015	0.10117491
Candidate Point 11	3.7405	0.382876465	13.6939435	573.2985091	0.09607365
Candidate Point 12	1.9255	0.794314453	15.1118676	876.0905894	0.0853414
Candidate Point 13	3.4765	0.407046387	11.8503221	588.2497136	0.09062592
Candidate Point 14	1.8235	0.943728516	13.2106331	983.4204652	0.09930989
Candidate Point 15	3.3325	0.415835449	11.3894168	594.0027497	0.08625521
Candidate Point 16	3.7885	0.36529834	15.0766596	553.4383196	0.09106743
Candidate Point 17	2.1175	0.795413086	11.4246248	870.2214438	0.10046325
Candidate Point 18	3.5245	0.424624512	13.2330382	595.9932783	0.09952825
Candidate Point 19	2.1895	0.733889648	10.7332668	821.9844216	0.09354284
Candidate Point 20	1.7635	0.904177734	14.9390281	946.2675163	0.0864001

54

The Nonlinear Programming by Quadratic Lagrangian (NLPQL) optimisation scheme was chosen to refine the previous results. The NLPQL method is a gradient-based algorithm to provide a refined, local, optimisation results. It supports a single output parameter objective, multiple constraints and is limited to continuous parameters. The starting point must be specified to determine the region of the design space to explore. The starting design point was taken from the screening optimisation results and the objective was to maximize mean absorbed power with two constraints: an upper limit for (b/a) of 0.65 and a lower limit of CWR of 0.085. Table 5.4 shows the refined optimisation results for all three sizes of the single module. The values of the optimal input design parameters are used in the subsequent analyses for full modular configurations of the Wavergy device in the following section.

Table 5.4 Refined optimisation results

Parameter	N = 15		N = 21		N = 27	
	Starting value	Optimal value	Starting value	Optimal value	Starting value	Optimal value
a (m)	2.25	2.11085	2.25	2.132	2.25	2.16126
b/a	0.65	0.65	0.65	0.65	0.65	0.65
d (m)	15	13.10791	15	12.906	15	13.54341
Power (W)	1500	1649.887	1055	1155.203	778	874.3531
CWR	0.09	0.085	0.088	0.084998	0.086388	0.085001

5.2 Modular configuration results

5.2.1 Response surface results

Similar to the single module design grid, a two dimensional design grid consisting of 25 design points is used to investigate the effects of longitudinal and transverse spacing between modules. The two parameters forming the design grid are the ratio between the longitudinal spacing between joints (L_s) and the major axis of the module ($2a$) (module length along x-axis) and the ratio between the minimum transverse distance between modules (T_s) and the span of the module (s). Figure 5.8 shows the design grid for the multiple configuration response surfaces. This grid is used to generate the mean absorbed power and CWR response surfaces for three different configurations of the Wavergy device. The three configurations have the same total volume but differ in the number of modules in the modular array. Figures 5.9, 5.10, and 5.11 show examples of the mesh used for solving the hydrodynamic diffraction runs for 15, 21 and 27 modules of Wavergy respectively. Only the underwater part of the device was meshed with a maximum element size of 1 m and a defeaturing tolerance of 0.1 m. The connection bodies were set to be hydrodynamically transparent meaning that they do not interact with other bodies in the simulation.

Figures 5.12, 5.14 and 5.16 show the power response surface results for 15, 21 and 27 modules configuration of Wavergy respectively. Figures 5.13, 5.15 and 5.17 show their corresponding CWR surfaces. The active width of the full modular configuration of Wavergy is taken as the total device's width given as: $s/3 (N + (N-3) \times T_s/s)$.
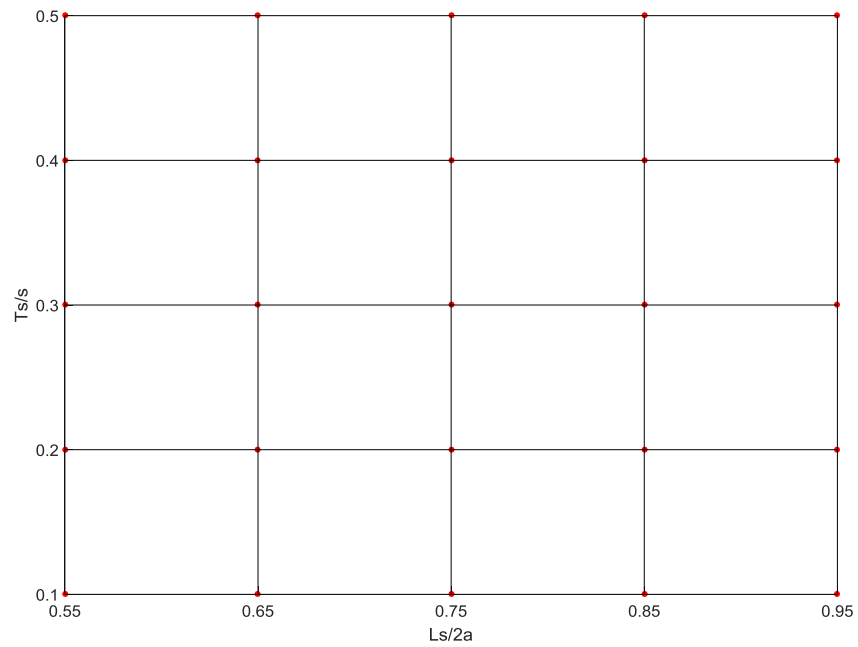
Figure 5.8 Modular configuration response surfaces fitting design grid
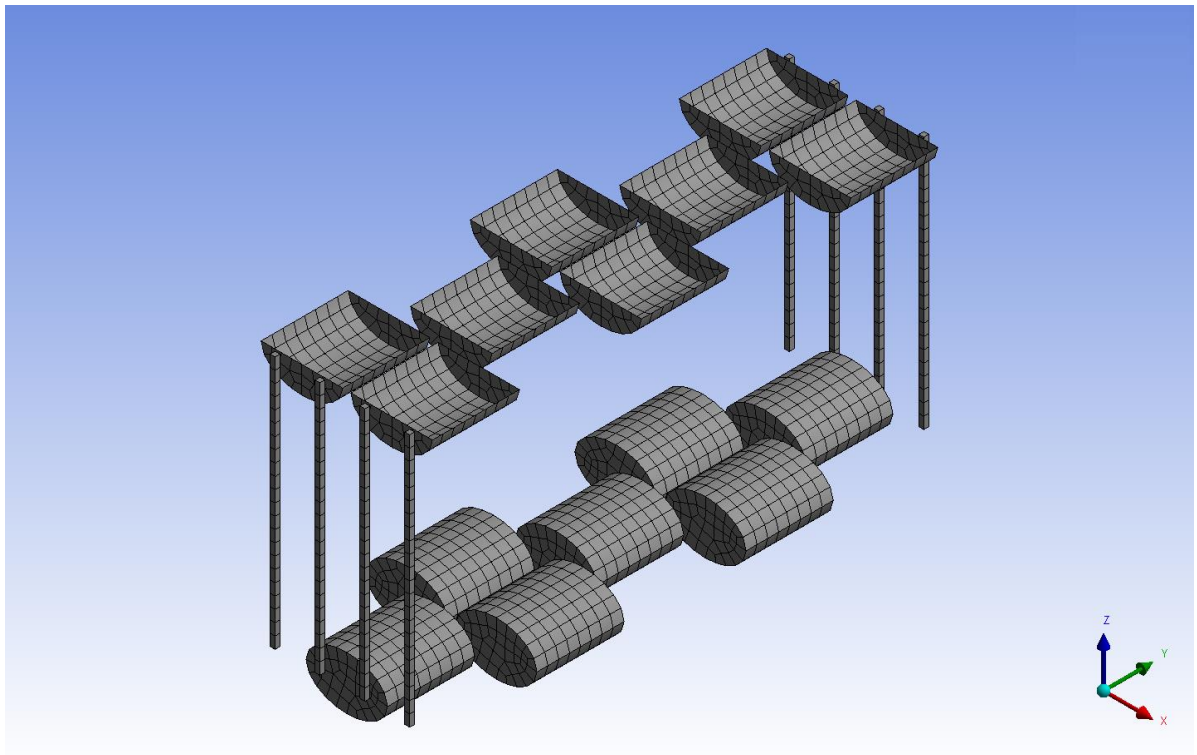
Figure 5.9 An example of the mesh used in hydrodynamic diffraction runs for the 15 modules configuration with 3328 diffracting elements
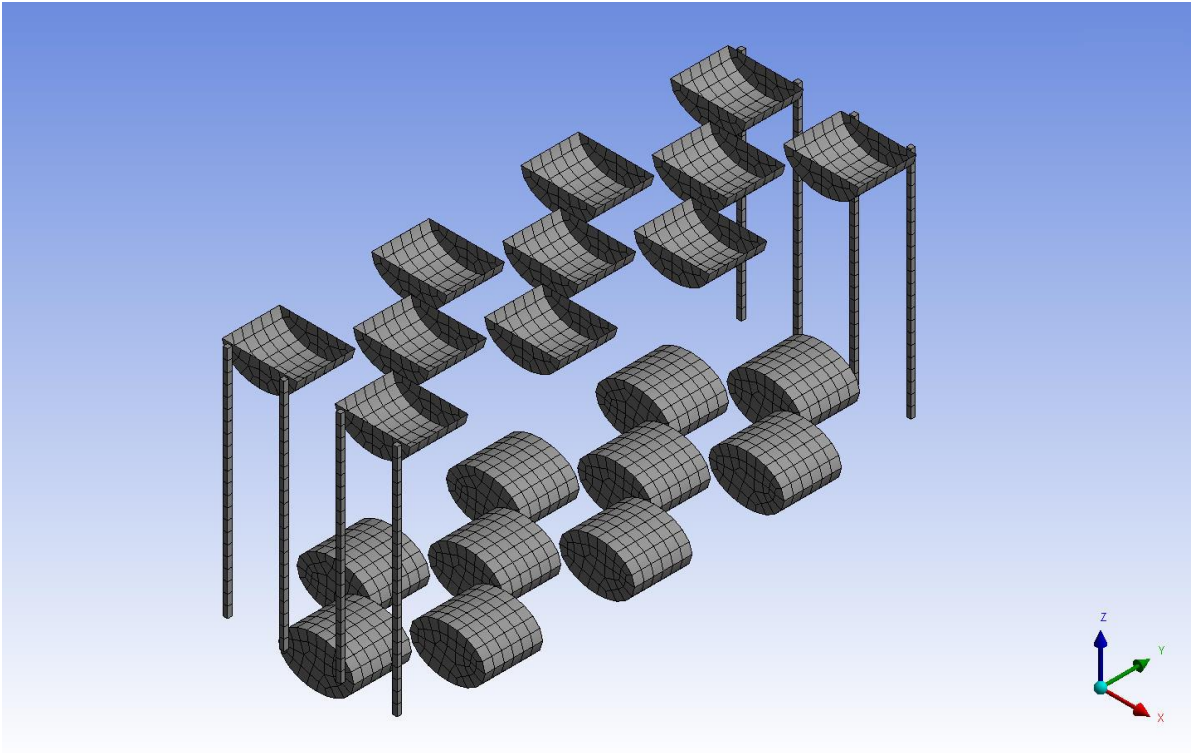
Figure 5.10 An example of the mesh used in hydrodynamic diffraction runs for the 21 modules configuration with 3776 diffracting elements
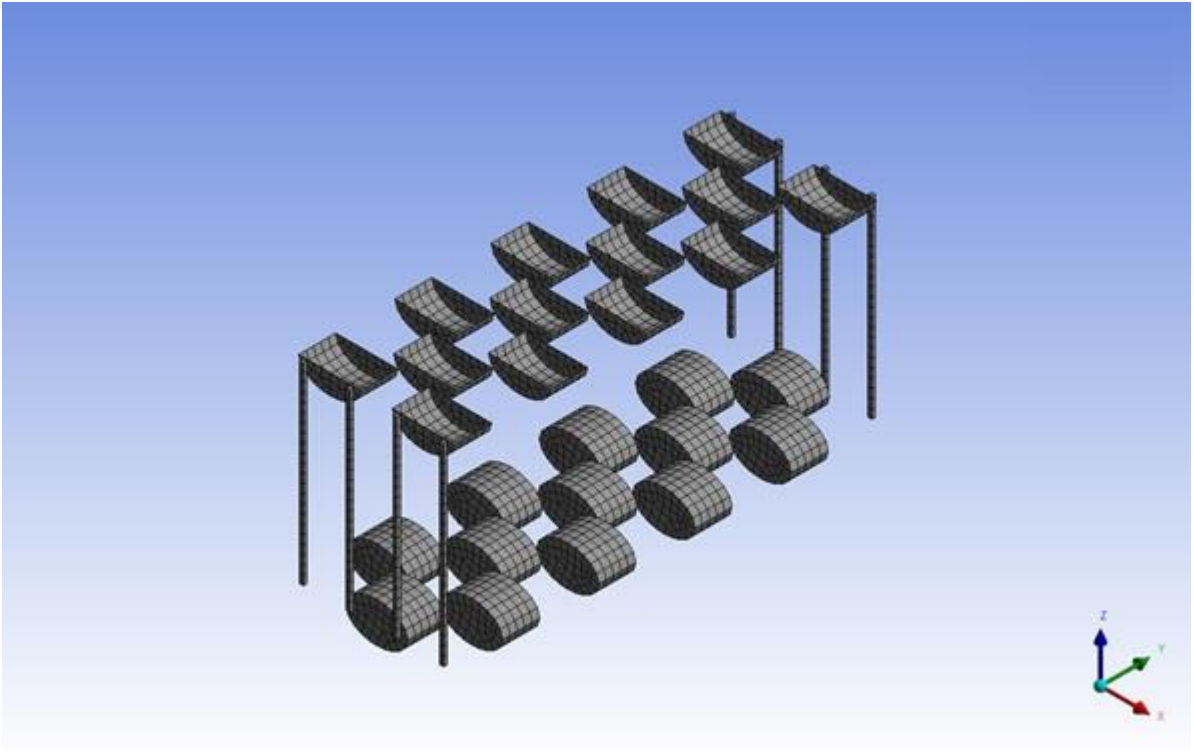
Figure 5.11 An example of the mesh used in hydrodynamic diffraction runs for the 27 modules configuration with 4264 diffracting elements
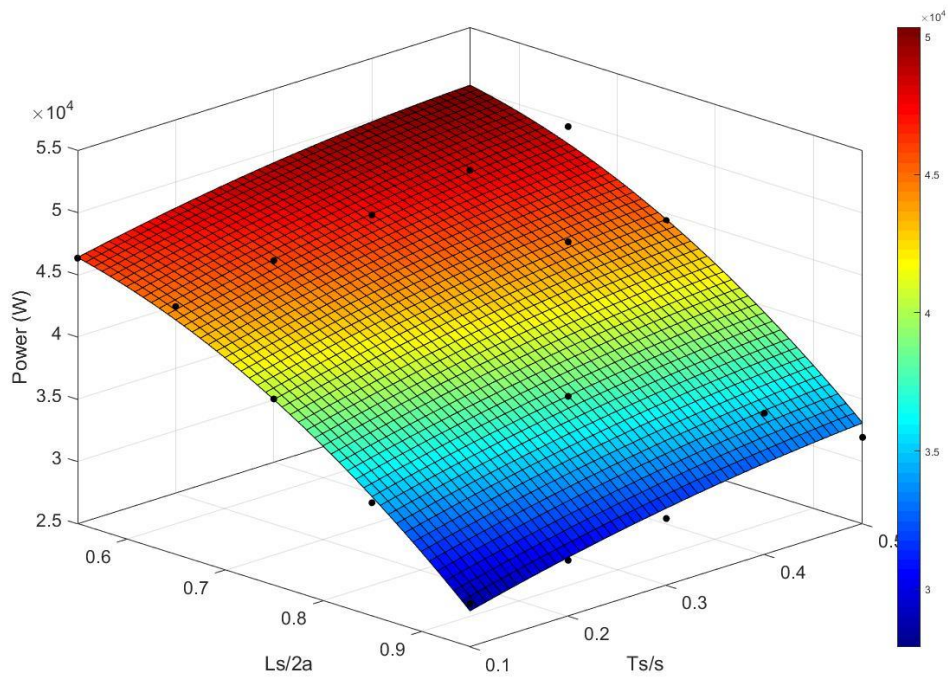
Figure 5.12 Power response surface for 15 Modules with 13 m submergence depth for lower blanket (black dots represent the fitting points from the design points runs)
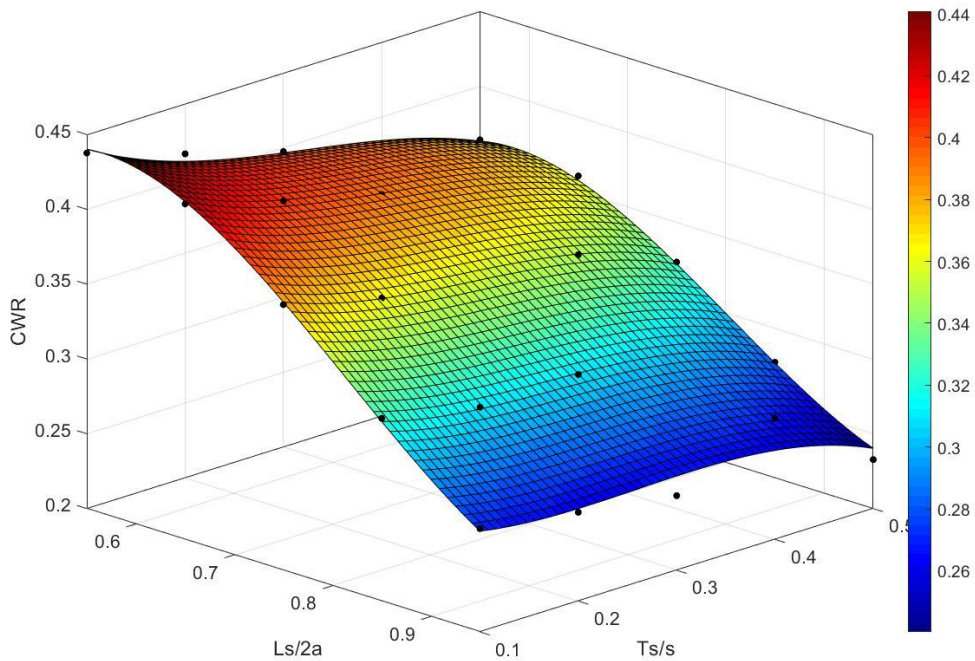
Figure 5.13 *CWR* response surface for 15 Modules with 13 m submergence depth for lower blanket (black dots represent the fitting points from the design points runs)
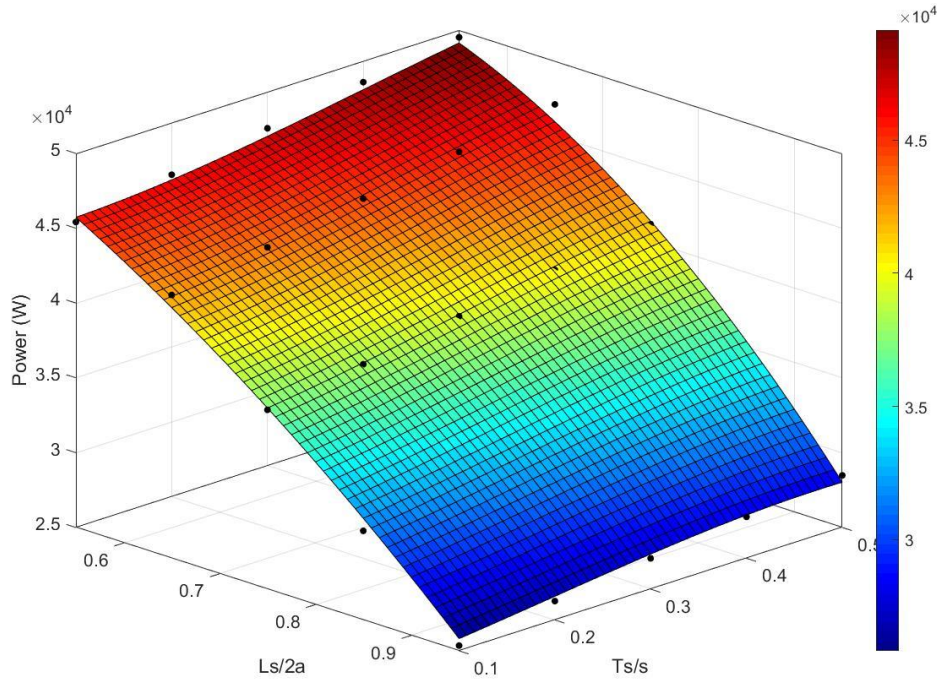
Figure 5.14 Power response surface for 21 Modules with 13 m submergence depth for lower blanket (black dots represent the fitting points from the design points runs)
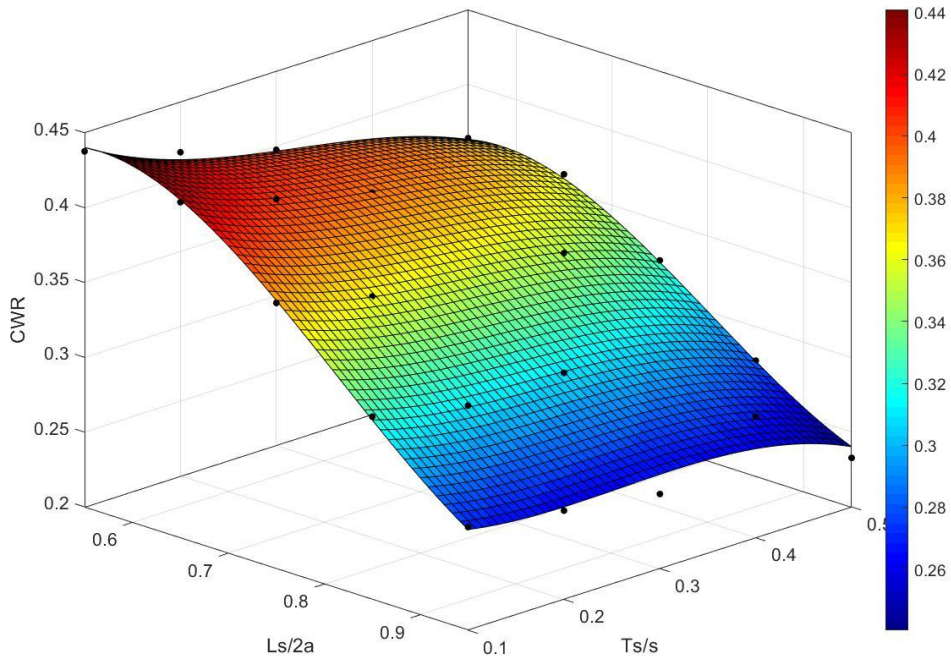
Figure 5.15 *CWR* response surface for 21 Modules with 13 m submergence depth for lower blanket (black dots represent the fitting points from the design points runs)
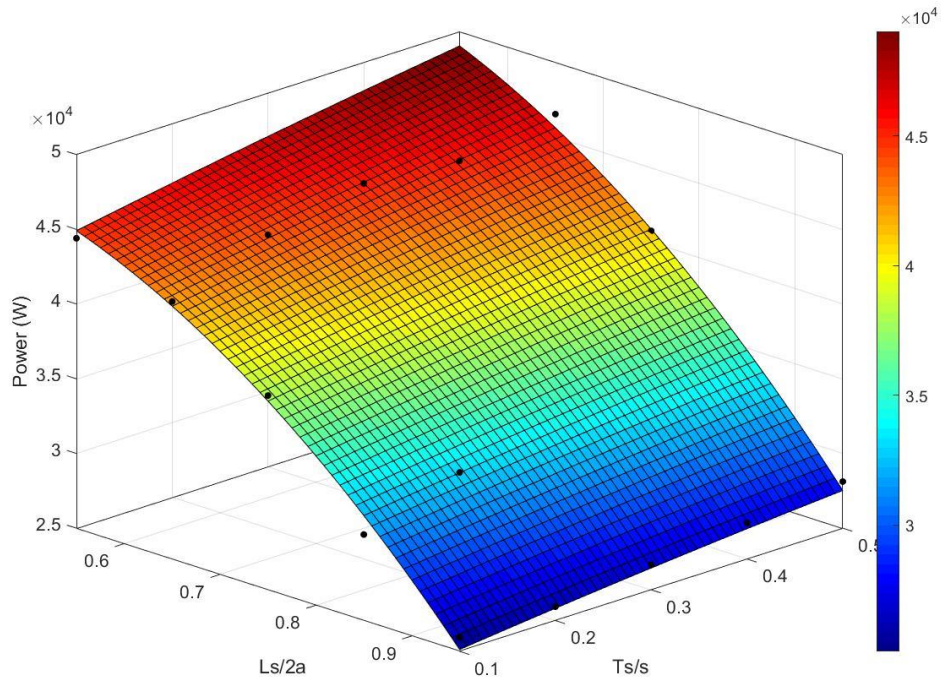
Figure 5.16 Power response surface for 27 Modules with 13.5 m submergence depth for lower blanket (black dots represent the fitting points from the design points runs)
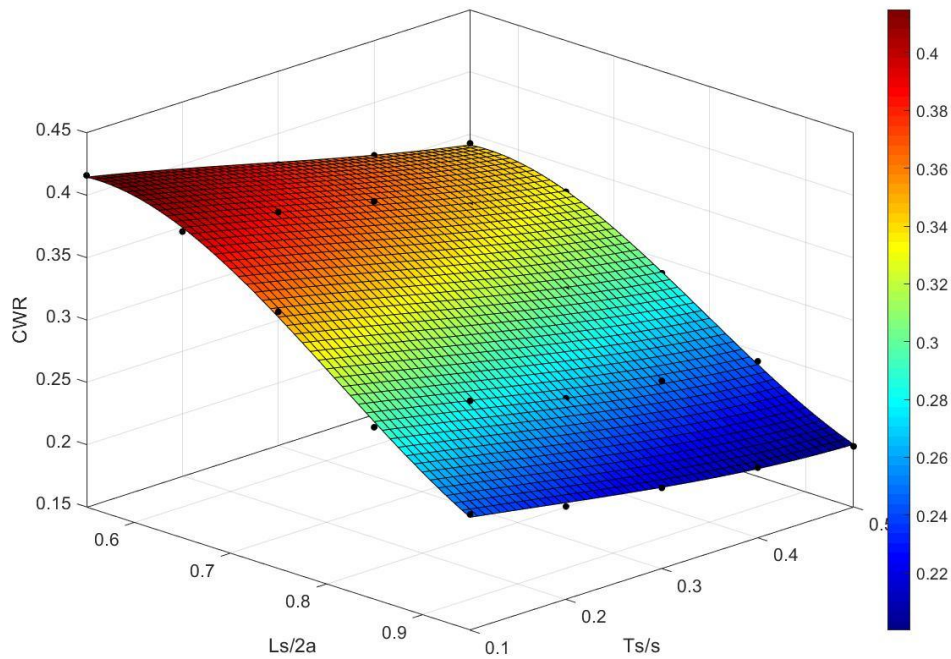
Figure 5.17 *CWR* response surface for 27 Modules with 13.5 m submergence depth for lower blanket (black dots represent the fitting points from the design points runs)

Mean absorbed power increases significantly with smaller longitudinal joint spacing. For a constant (T_s/s) value, the increase in mean absorbed power between the maximum and minimum values of $(L_s/2a)$ is roughly 60 to 80%. Conversely, larger transverse spacing between modules results in higher mean absorbed power. However, the effect of transverse spacing is miniscule compared to longitudinal joint spacing with only 8 to 12% increase in mean absorbed power between the minimum and maximum values of (T_s/s) for a constant $(L_s/2a)$ value.

The *CWR* results behave in the same manner as the mean absorbed power results in the direction of $(L_s/2a)$ where the smallest values of $(L_s/2a)$ gives maximum *CWR* values. On the other hand, unlike mean absorbed power results, *CWR* value decrease with increasing (T_s/s) value due to larger active width of the device. The multiple modules results show significant improvement of *CWR* values ranging from 0.19 to 0.43 over the corresponding single module *CWR* value of 0.085. Another very important remark from the results is the fact that the three configurations of 15, 21 and 27 modules have very close values of mean absorbed power and *CWR*. This suggests that for the same cross-section shape, total volume and total PTO damping coefficient of the device the mean absorbed power is independent of the number of modules of the device.

5.2.2 Effect of submergence depth of lower blanket

Large depths for the lower blanket may compromise the structural integrity of the Wavergy device due to high stresses on the long connection bars and may also be problematic for the installation and maintenance of the device. These effects should be considered in further structural analysis and deployment procedure which is out of the scope of this work. To reduce these effects the submergence depth of the lower blanket is limited to the value that generates the same mean absorbed power as the Pelamis benchmark design given in [30]. Figure 5.18 shows the variation of mean absorbed power with respect to submergence depth of the lower blanket.
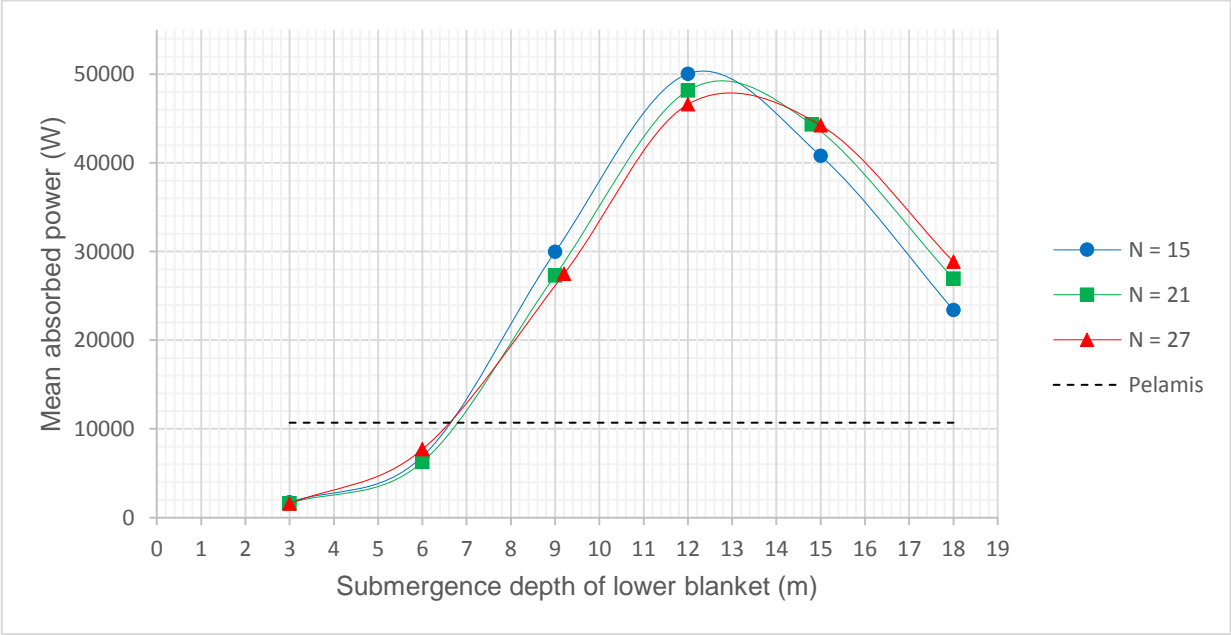
Figure 5.18 Variation of mean absorbed power by Wavergy with submergence depth of the lower blanket

61

Figure 5.18 illustrates that mean absorbed power reaches its maximum value at around 13 m of submergence depth of the lower blanket for all of the three Wavergy configurations. This shows correlation with the single module results which also had an optimum submergence depth of fixed points close to 13 m. The submergence depth of the lower blanket at which the Wavergy device generates the same mean absorbed power as the Pelamis benchmark design is 6.7 m. The final chosen design parameters of the Wavergy device is given in Table 5.5.

Table 5.5 Chosen parameter values for the Wavergy device

Parameter	Value
Total Number of Modules in full configuration (N)	15
Major semi-axis (a)	2.1 m
Axis ratio (b/a)	0.65
Transverse span (s)	4.48 m
Submergence depth of lower blanket (d)	6.7 m
Longitudinal joint spacing to length ratio ($L_s/2a$)	0.55
Minimum transverse spacing between modules to span ratio (T_s/s)	0.5
Total joint damping coefficient	1.35e8 N.m/rad/s
Mooring lines stiffness	2e6 N/m

5.2.3 Variation of mean absorbed power with size

In [30], the effect of the size of the device on mean absorbed power of the Pelamis device was evaluated by increasing the diameter of the cylindrical sections and it was found that power increases with the size of the device. To evaluate the effect of size of the Wavergy device on its power performance the total volume of the chosen Wavergy design is varied by using each of the following approaches:

- Increasing the number of modules (21, 27 and 33 modules)
- Increasing the span of each individual module
- Scaling the modules dimensions

Figures 5.19 and 5.20 show the variation of mean absorbed power and *CWR* with size respectively. It is shown that the effect of increasing the size of the device by adding modules is the most favourable approach in terms of obtaining larger mean absorbed power and *CWR* values. Increasing the span of individual modules of the chosen 15 module configuration to correspond to the total volume of the 21, 27 and 33 module device produces power results close to that of increasing volume by adding modules, however, the difference in *CWR* values is more prominent since increasing the span of the device while maintaining a constant value of (T_s/s) means a larger active width of the device. Finally, increasing the device's size by scaling the modules dimensions has the least effect on power. All of the three methods have more effect on enhancing power performance than increasing the diameter of the Pelamis benchmark device and the first two methods surpass the Pelamis' *CWR* beyond values of 950 and 1090 m^3 respectively.
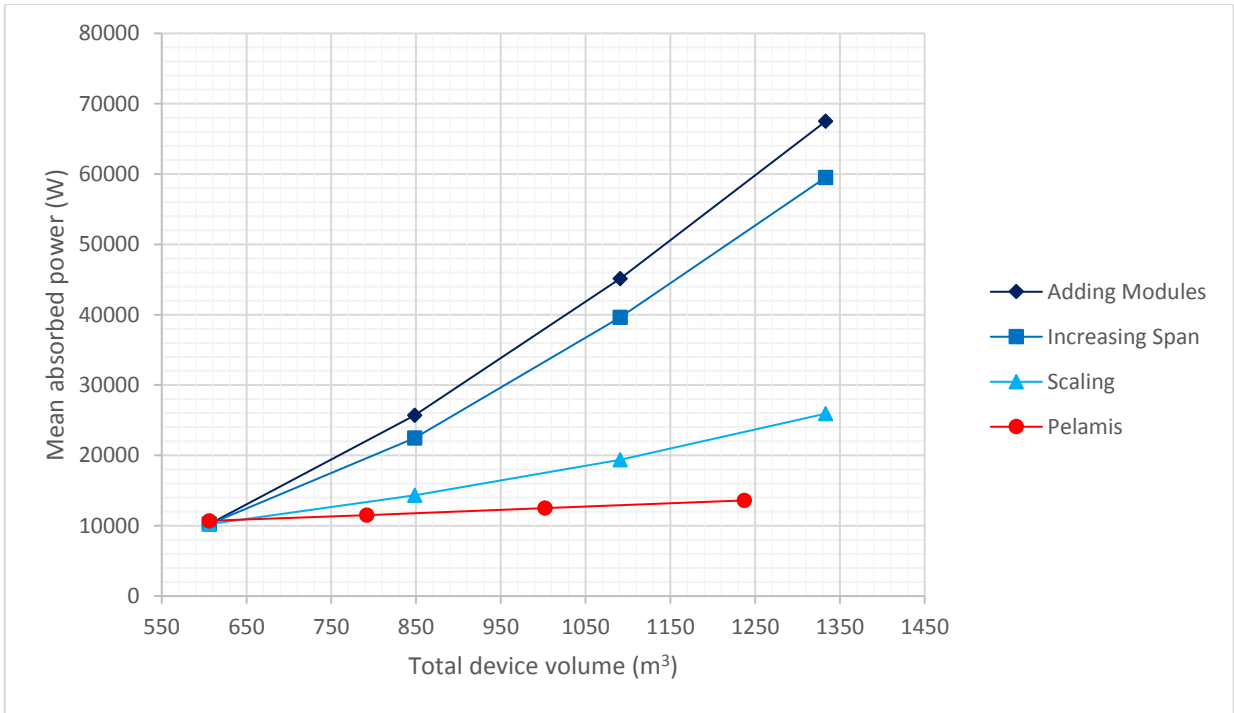
Figure 5.19 Effect of increasing Wavergy's size using different approaches on mean absorbed power
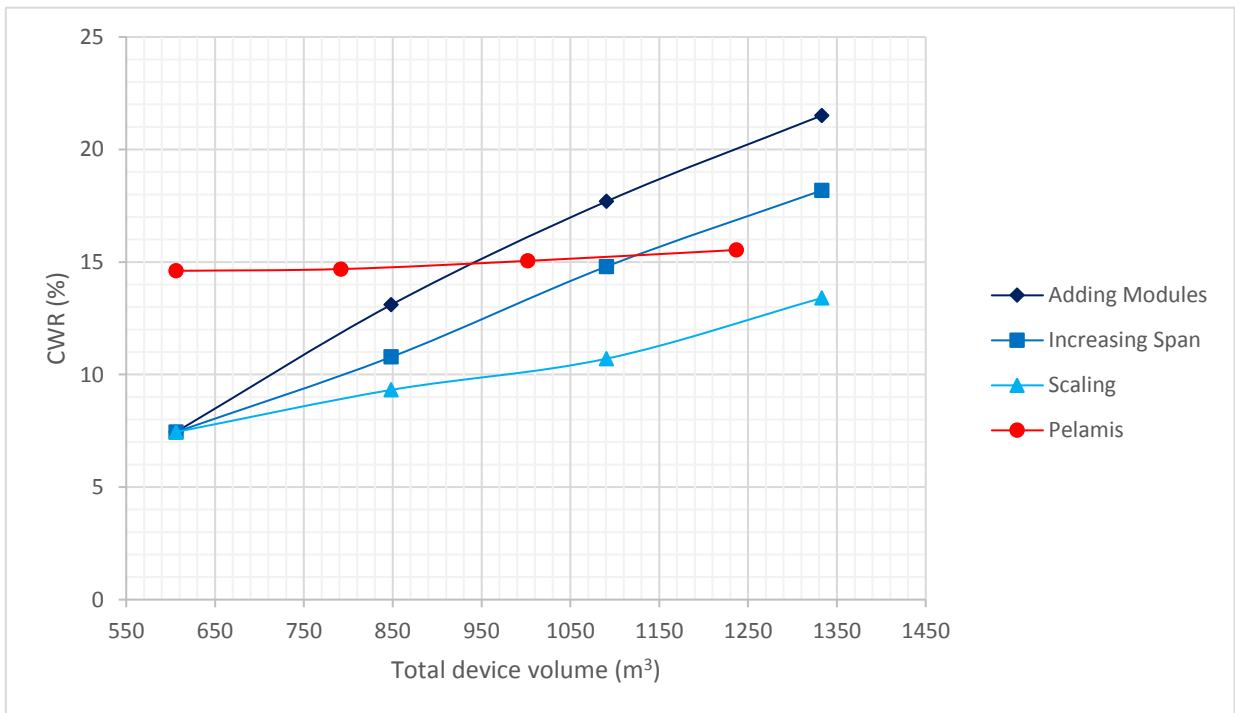
Figure 5.20 Effect of increasing Wavergy's size using different approaches on *CWR*

5.3 Verifying the frequency-domain statistical analysis results against time-domain analysis results

In order to verify the results obtained from the frequency-domain statistical analysis in the previous section, time-domain runs are performed for the chosen Wavergy design at the 10 sea states representing the benchmark wave site and given in Table 5.6.

Table 5.6 Wave site representative sea states

Sea state No.	Significant wave height (H_s)	Peak wave period (T_p)	Probability (η_{ss})
SS1	0.5 m	5 s	0.0205
SS2	1 m	5 s	0.0171
SS3	1 m	5.5 s	0.2889
SS4	1 m	6 s	0.1441
SS5	1.5 m	5.5 s	0.0867
SS6	1.5 m	6 s	0.2036
SS7	1.5 m	6.5 s	0.0294
SS8	2 m	6 s	0.0908
SS9	2 m	6.5 s	0.0328
SS10	2.5 m	6.5 s	0.0266

5.3.1 Removal of suspending standing waves

Applying the potential flow theory to the hydrodynamic problem of the interaction of waves with multiple floating bodies in close proximity may result in large suspending standing waves occurring within the gaps between the interacting bodies [47]. These unrealistic waves occur due to the absence of the viscous flow effects which would dampen them in a real environment. Suspending standing waves can cause sudden jumps at some frequencies in the radiation damping curves which is why it is important to get rid of the effects of these waves especially for time-domain analyses which rely on integrating the radiation damping over a range of frequencies to obtain the radiation impulse response function as stated in Eq (3.43). These sudden jumps could give unrealistic results or even prevent the convergence of the solution.

To simulate the additional damping caused by viscous and separation effects, ANSYS AQWA employs an "external lid" approach which acts as a new damped free-surface boundary condition imposed on the flow potential function between the interacting bodies. The effect of this external lid on suppressing standing waves is determined using two parameters: the damping factor (α_d) and the gap size (d_{gap}). The damping factor ranges from 0 to 1, with 0 giving no damping and 1 giving heavy damping, and is obtained using experimental results or trial measurements. The gap size is the characteristic length of the gap or the smallest dimension between the interacting structures [42]. Figure 5.21 shows the mesh of the chosen Wavergy design used for the time-domain analyses in this section with the external lid added between the upper blanket modules.
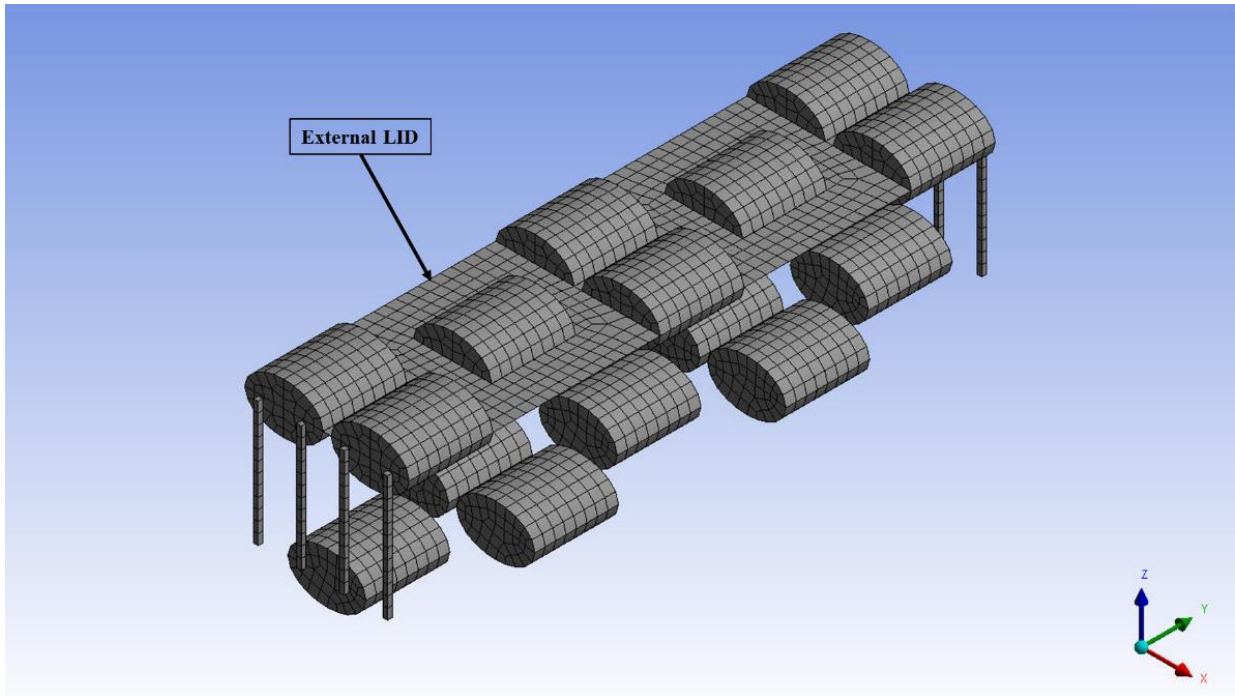
Figure 5.21 An example of the mesh used in the hydrodynamic diffraction runs associated with the time-domain analyses for the 15 modules configuration with 4324 diffracting elements including the external lid with a maximum element size of 1 m

Figures 5.22 and 5.23 show the effect of the damping factor on the surge radiation damping coefficient of the upper forward (and after) row of modules and the upper middle row of modules respectively. Figures 5.24 and 5.25 show the effect of the damping factor on the pitch radiation damping coefficients of the upper forward (and after) row of modules and the upper middle row of modules respectively.

At low damping factor values, the radiation damping coefficients experience abrupt changes at some frequencies for all the upper module rows. This effect is reduced as the damping factor value increases and is virtually eliminated at a damping factor value of 1.

To ensure convergence and that no instabilities would occur in the calculation of the radiation impulse response function by integrating over the frequency range as given in Eq. (3.43) a damping factor value of 1 is used in the following time-domain analyses.

It should be pointed out that for more accurate time-domain results the damping coefficient value at the highest frequency in the analysis should be close to zero. This is, however, hard to achieve because of the limitations on the number of diffracting elements in ANSYS AQWA and the dependence of the maximum frequency in the analysis on the maximum element size, in addition to the fact that the Wavergy device is made up of multiple bodies that are small compared to the size of the entire device. In the following subsection, a mesh refinement study is performed to assess the effect of the maximum element size on the results obtained from the time-domain analysis.

65
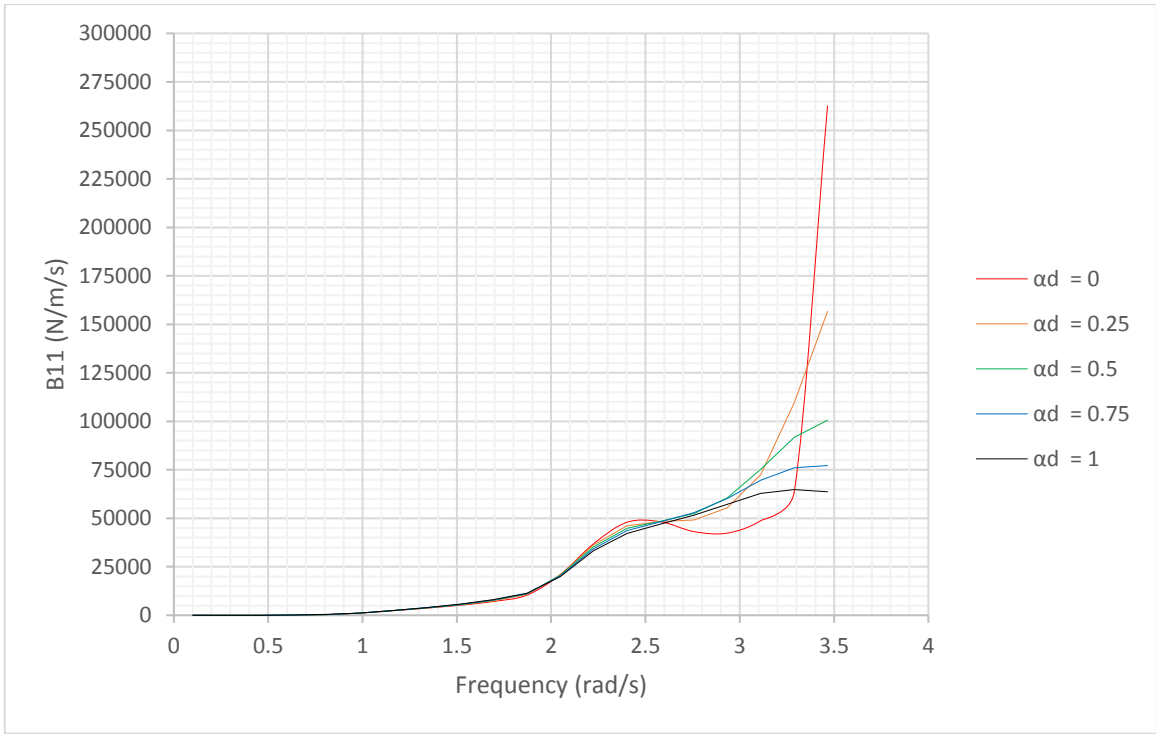
Figure 5.22 Surge radiation damping for the Forward and Aft module rows with various damping factors values
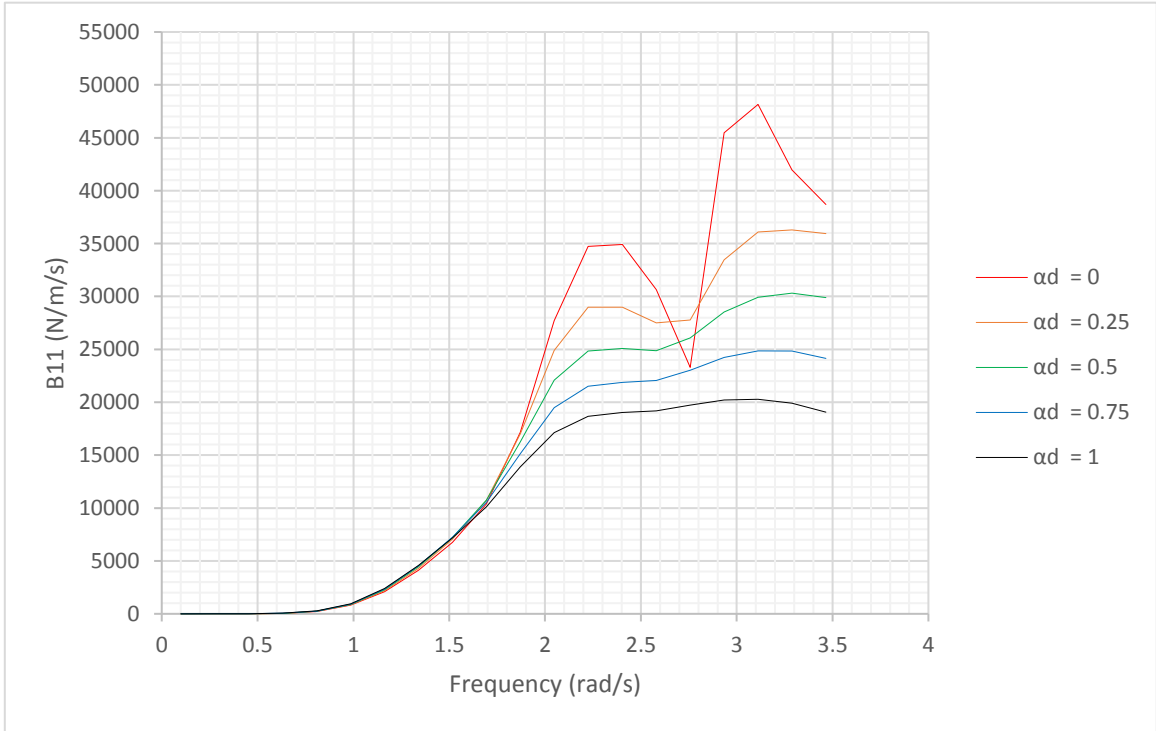
Figure 5.23 Surge radiation damping for the Middle module row with various damping factors values
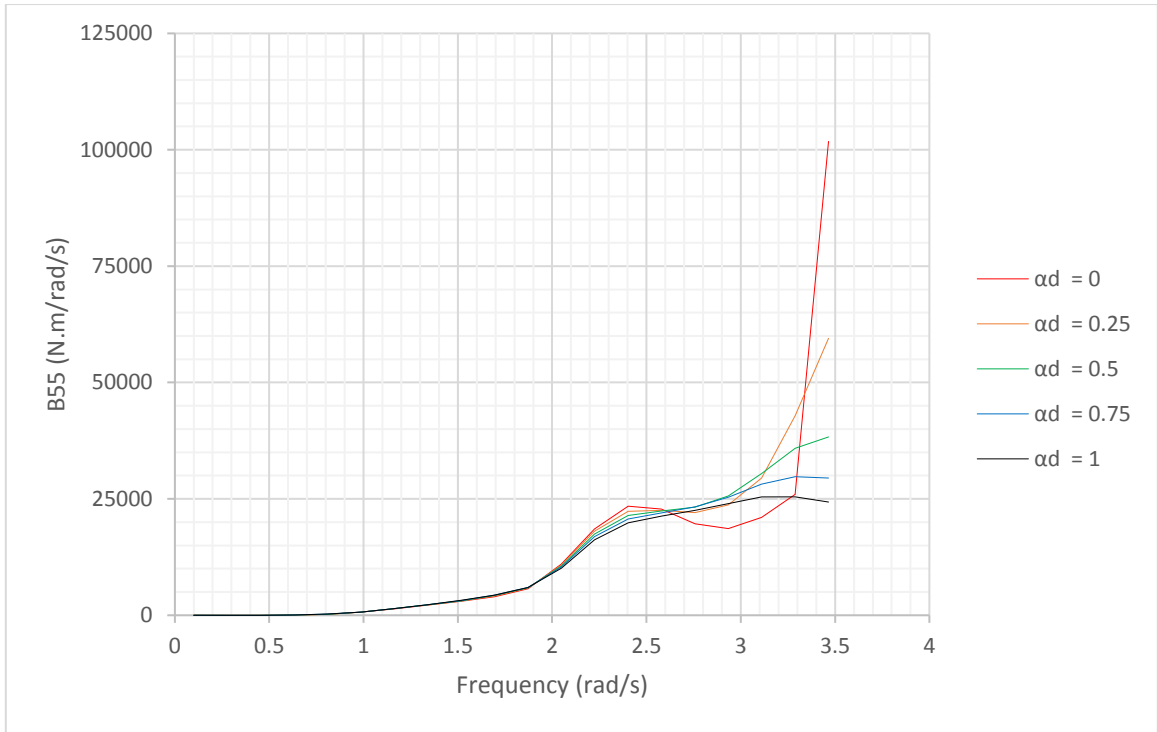
Figure 5.24 Pitch radiation damping for the Forward and Aft module rows with various damping factors values
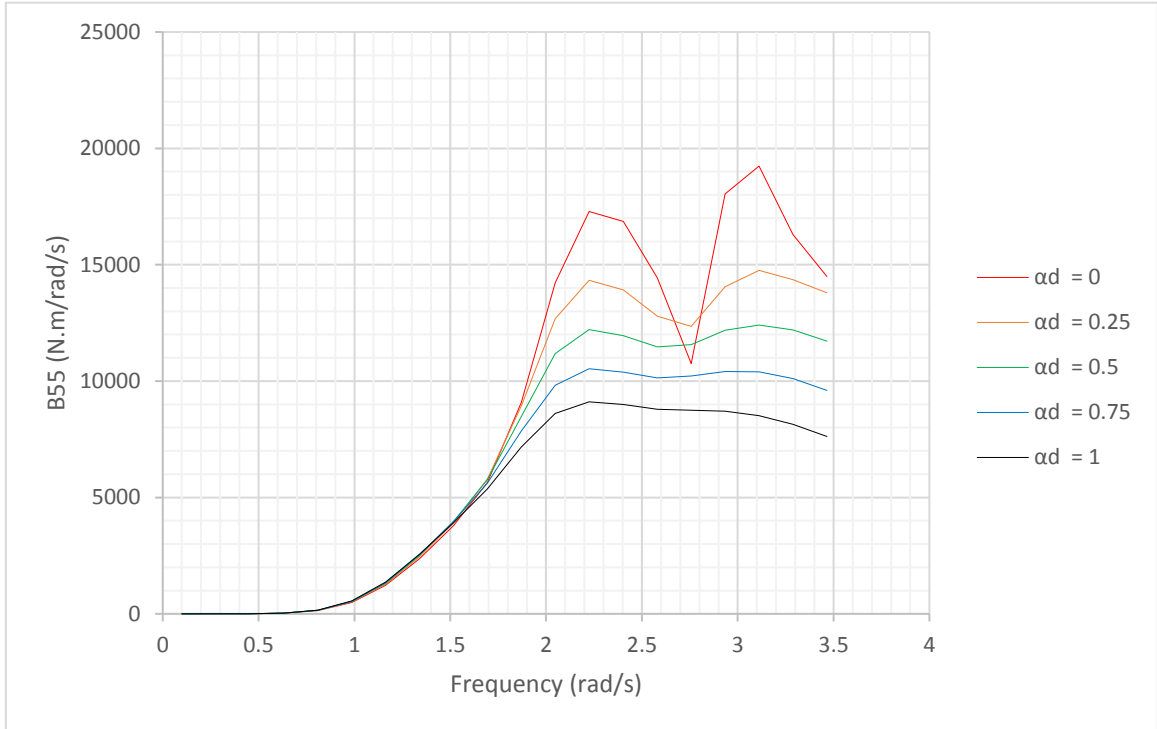
Figure 5.25 Pitch radiation damping for the Middle module row with various damping factors values

5.3.2 Time-domain vs. Frequency-domain results

The mean absorbed power results of the chosen Wavergy design for the ten representative sea states obtained from time-domain runs with durations equal to 125 T_p and a fixed time step of 0.01 s for a max mesh element size of 0.32 m, 0.5 m and 1 m are plotted against the results obtained from the frequency-domain statistical analyses in Figure 5.26.
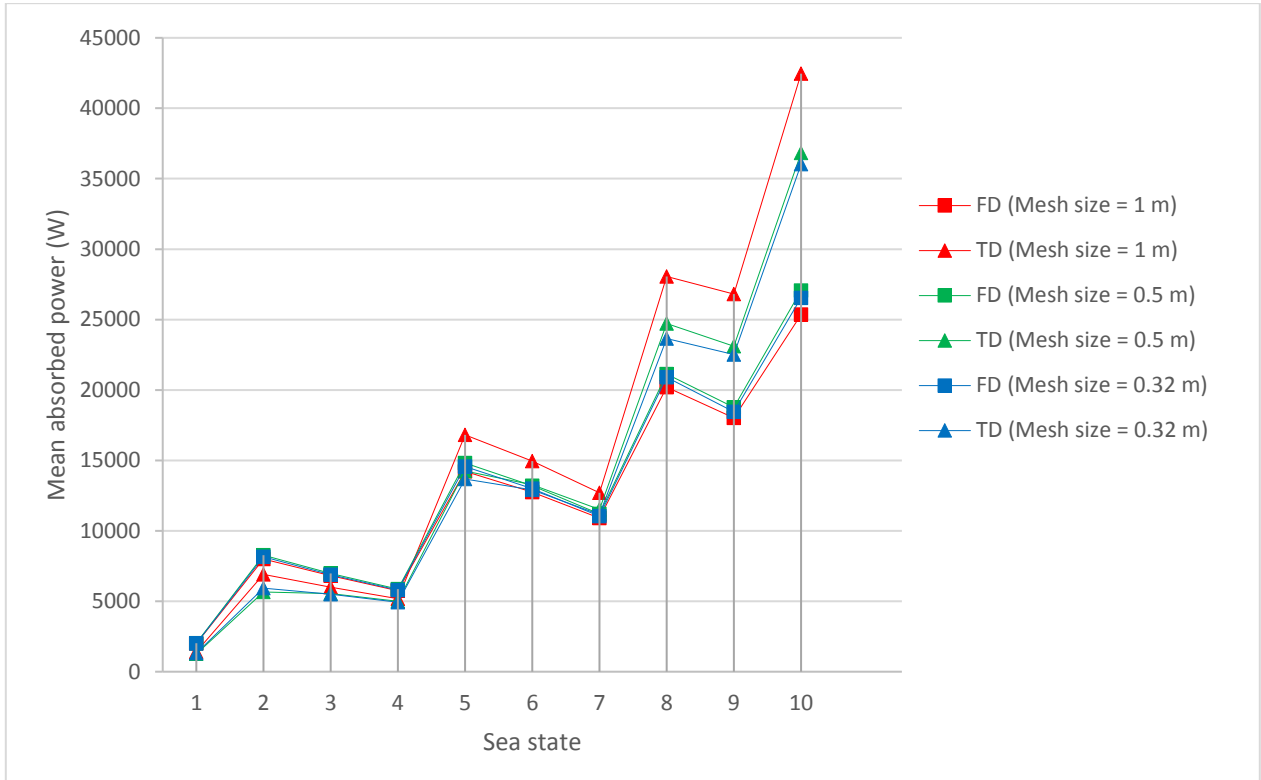
Figure 5.26 Mean absorbed power of the 10 representative sea states obtained from Time-domain analysis Vs Frequency-domain analysis

The power results obtained using the frequency-domain and time-domain analyses are close for sea states with small wave heights. On the other hand, for large wave heights the time domain estimates are significantly higher. This difference between the frequency-domain and time-domain results is reduced for finer mesh sizes with the frequency-domain results being similar for the all mesh sizes. This suggests that the time-domain results approach the frequency-domain results for finer mesh sizes. Nevertheless, the larger wave heights have low probability of occurrence as illustrated in Table 5.6, so their effect on the overall power results is reduced.

The overall total annual mean absorbed power values for the benchmark wave site obtained from the time-domain analyses is 12.06 kW, 10.7 kW and 10.4 kW for mesh sizes of 1 m, 0.5 m and 0.32 m respectively. While the corresponding values obtained from the frequency-domain statistical analysis are 10.22 kW, 10.6 kW and 10.4 kW with 15%, 1% and 0.34% reduction in the power estimate from the time-domain results for the 1 m, 0.5 m and 0.32 m max mesh element size respectively.

5.4 Optimised power matrix for the chosen Wavergy design

Optimising power output is achieved through tuning the PTO system properties, i.e. the PTO damping and stiffness. This is done either on a wave by wave basis or on a sea state basis. Tuning the PTO system on a wave by wave basis has the potential to increase power absorption significantly, however, it requires prediction of the future incident waves which is very difficult to achieve given the haphazard nature of sea waves. On the other hand, tuning the PTO system on a sea state basis is easily achieved in practice by measuring the sea state at a distance from the WEC with a data buoy and adjust the system based on the acquired information [26]. The latter method is assumed here to generate the optimised power matrix for the chosen Wavergy design.

5.4.1 Power Take-off tuning

To find the optimal damping, the Adaptive Single-objective optimisation scheme is used with the total PTO damping coefficient of all the connections (B_{pto}) as the input parameter and the mean absorbed power as the output parameter. The Adaptive Single-Objective method is a gradient-based algorithm that supports a single output parameter objective, multiple constraints and aims at finding the global optimum [46]. It is assumed that the PTO system has no stiffness. The optimisation is performed for 6 wave peak periods (T_p) of 4 s to 16 s with a 2 s step with a significant wave height (H_s) of 1 m and an iteration convergence percentage of 0.01%. The range of (B_{pto}) is from 1e4 N.m.s/rad to 1e9 N.m.s/rad.

Figures 5.27 and 5.28 show the iteration results of the optimisation of the input parameter (B_{pto}) and output parameter (the mean absorbed power) respectively. The results show that the device absorbs more power from shorter waves than longer waves. This is expected since the benchmark design wave site was dominated by relatively short wave periods (5 s to 6.5 s).
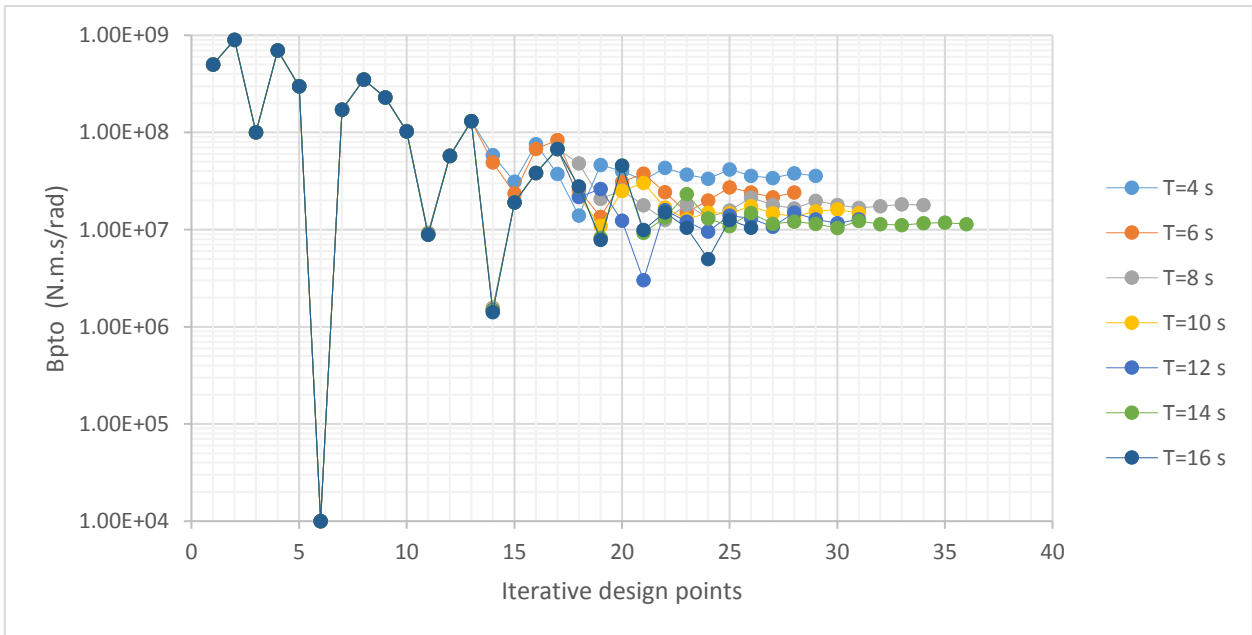
Figure 5.27 PTO damping coefficient optimisation iteration results for various wave peak periods at 1 m significant wave height
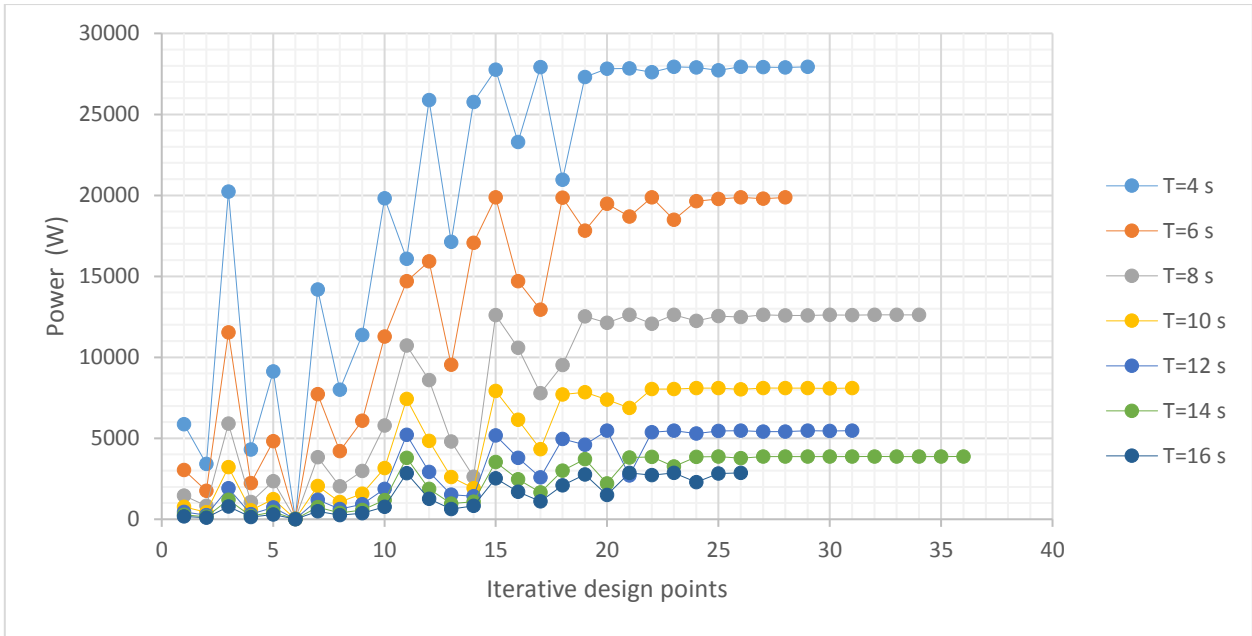
Figure 5.28 Mean absorbed power optimisation iteration results for various wave peak periods at 1 m significant wave height

The optimum values of the total PTO damping coefficient is plotted against the peak wave period (T_p) in Figure 5.29. The optimum PTO damping coefficient for intermediate wave periods can be obtained by interpolating on this curve.
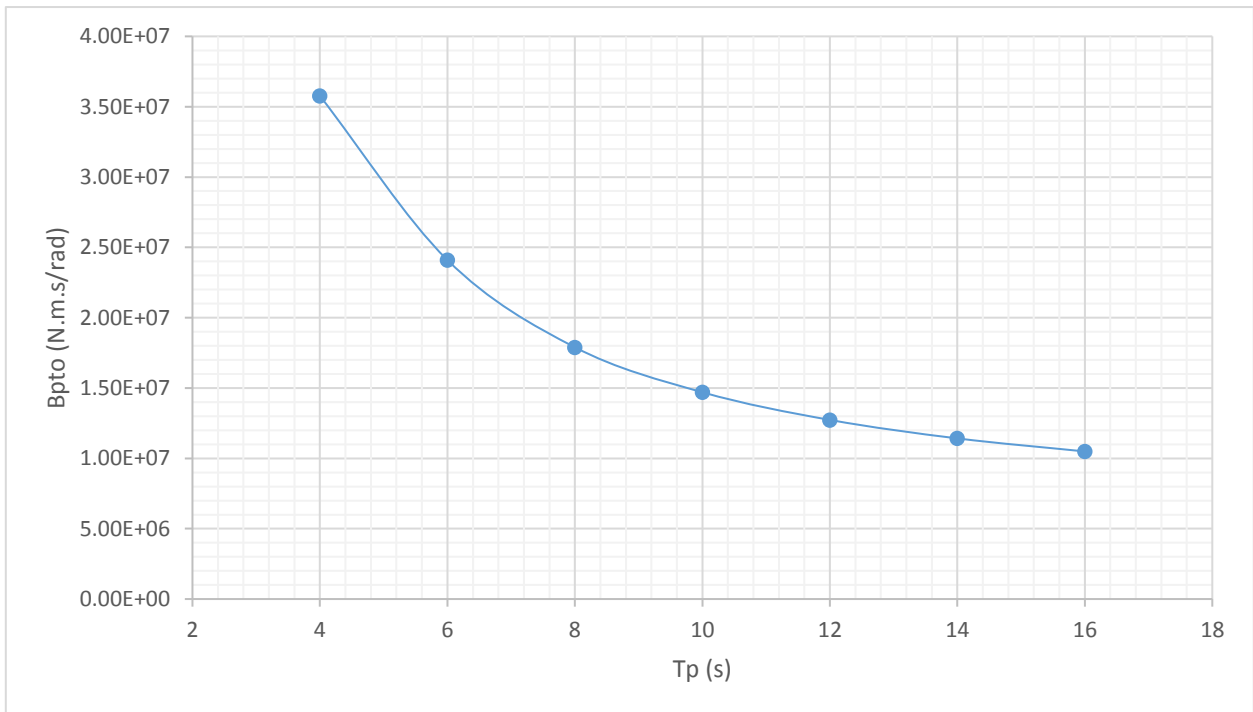
Figure 5.29 Optimum total PTO damping coefficient as a function of peak wave period

5.4.2 Generating power matrix

The optimised power matrix is generated with the frequency-domain statistical analysis method using 123 sea states with significant wave heights ranging from 0.5 m to 10.5 m and a peak time period ranging from 4 s to 16 s. These ranges for significant wave height and peak wave period cover most of the sea states encountered in various locations with different wave power resources according to [26]. The optimised power matrix for the chosen Wavergy design is given in Table 5.7.

Table 5.7 Optimised power matrix for the chosen Wavergy design (kW)

$T_p(s)$ / $H_s(m)$	4	5	6	7	8	9	10	11	12	13	14	15	16
0.5	4.09	3.96	3.36	2.72	2.18	1.75	1.41	1.15	0.95	0.79	0.67	0.57	0.49
1.5	41.86	35.21	30.06	24.49	19.63	15.72	12.67	10.33	8.51	7.09	5.99	5.12	4.42
2.5	116.28	97.99	76.10	63.99	54.53	43.67	35.20	28.69	23.64	19.69	16.64	14.22	12.28
3.5		192.06	149.72	113.25	95.95	82.93	69.00	56.22	46.34	38.59	32.62	27.87	24.06
4.5			247.49	183.99	145.94	123.86	108.52	92.94	76.61	63.79	53.92	46.07	39.78
5.5			369.71	274.85	208.06	170.87	147.78	130.99	114.44	95.30	80.55	68.82	59.42
6.5				383.88	290.59	225.44	191.71	169.43	150.97	133.10	112.51	96.11	82.99
7.5				511.08	386.88	300.15	239.77	209.66	187.53	168.91	149.79	127.96	110.49
8.5				656.46	496.93	385.52	303.47	254.96	226.20	203.92	184.98	164.36	141.92
9.5				820.00	620.73	481.57	379.07	305.21	267.51	240.86	218.25	200.02	177.28
10.5				1001.72	758.29	588.29	463.08	372.84	310.87	278.55	253.51	232.54	213.98

5.5 Comparison with other WECs

In this section, a comparison is made between the Wavergy device and the selection of WECs studied in [26]. The WEC principles used in the comparison are: small bottom-referenced heaving buoy (Bref-HB), bottom-referenced submerged heave-buoy, floating two-body (F-2HB), bottom-fixed heave-buoy array (B-HBA), floating heave-buoy array (F-HBA), bottom-fixed oscillating flap (B-OF), floating three-body oscillating flap device (F-3OF) and floating oscillating water column (F-OWC). The previous working principles are illustrated in Figure 5.30. Five representative wave sites along the European cost with power resource levels ranging from 15 kW/m to 80 kW/m. Tables 5.8 to 5.12 show the percentage probability distribution of the sea states for the five sites. Four performance evaluation measures were used in this study namely: the annual mean absorbed power (kW), the capture width ratio (%), the annual absorbed energy per characteristic mass (kWh/kg) and the annual absorbed energy per wetted surface area (MWh/kg).
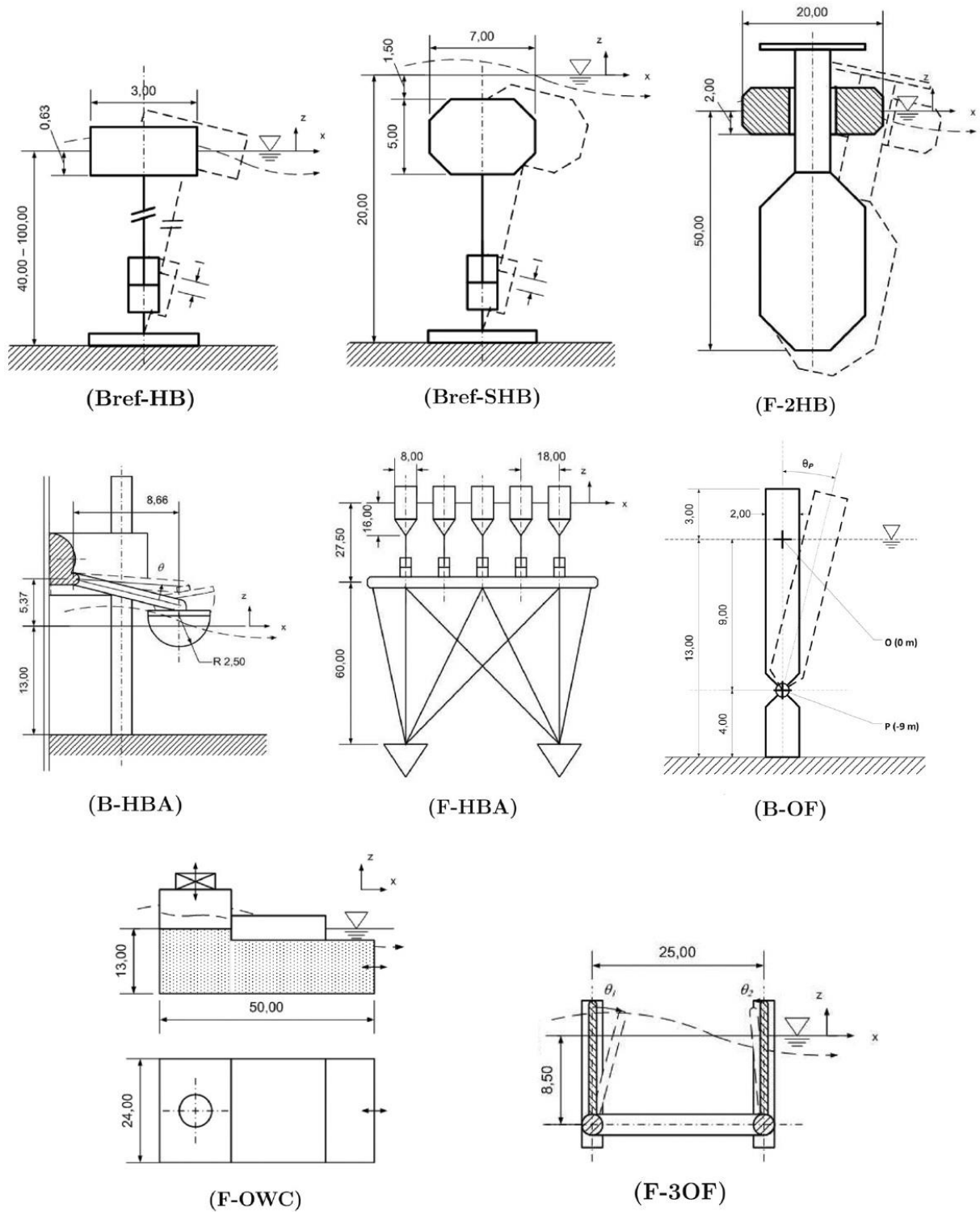
Figure 5.30 Wave energy conversion working principles studied in [26]

Table 5.8 Sea states probability distribution in % of the SEM-REV site (14.8 kW/m) [26]

$T_p(s)$ / $H_s(m)$	3.5	4.5	5.5	6.5	7.5	8.5	9.5	10.5	11.5	12.5	13.5	14.5	15.5	16.5
0.75	0.28	0.49	0.64	1.00	2.11	4.29	5.61	4.86	3.45	2.39	1.68	1.11	0.58	0.19
1.25	0.20	0.43	0.69	1.15	2.00	3.38	4.41	4.23	3.64	3.10	2.50	1.91	1.16	0.39
1.75	0.00	0.07	0.26	0.62	1.15	1.70	1.93	1.87	2.07	2.25	2.10	1.79	1.24	0.46
2.25	0.00	0.00	0.03	0.19	0.51	0.95	1.23	1.19	1.19	1.27	1.24	1.08	0.84	0.37
2.75	0.00	0.00	0.00	0.04	0.18	0.43	0.70	0.81	0.80	0.77	0.73	0.65	0.50	0.23
3.25	0.00	0.00	0.00	0.00	0.04	0.15	0.31	0.45	0.54	0.54	0.51	0.47	0.35	0.14
3.75	0.00	0.00	0.00	0.00	0.00	0.04	0.12	0.23	0.32	0.39	0.39	0.34	0.24	0.09
4.25	0.00	0.00	0.00	0.00	0.00	0.01	0.04	0.09	0.18	0.24	0.26	0.23	0.18	0.07
4.75	0.00	0.00	0.00	0.00	0.00	0.00	0.00	0.03	0.08	0.14	0.18	0.16	0.14	0.05
5.25	0.00	0.00	0.00	0.00	0.00	0.00	0.00	0.00	0.03	0.07	0.11	0.12	0.09	0.04
5.75	0.00	0.00	0.00	0.00	0.00	0.00	0.00	0.00	0.00	0.01	0.04	0.07	0.08	0.03
6.25	0.00	0.00	0.00	0.00	0.00	0.00	0.00	0.00	0.00	0.00	0.01	0.04	0.05	0.03
6.75	0.00	0.00	0.00	0.00	0.00	0.00	0.00	0.00	0.00	0.00	0.01	0.01	0.03	0.01
7.25	0.00	0.00	0.00	0.00	0.00	0.00	0.00	0.00	0.00	0.00	0.00	0.01	0.01	0.00
7.75	0.00	0.00	0.00	0.00	0.00	0.00	0.00	0.00	0.00	0.00	0.00	0.00	0.01	0.00

Table 5.9 Sea states probability distribution in % of the EMEC site (21.8 kW/m) [26]

$T_p(s)$ / $H_s(m)$	5.7	7.1	8.5	9.9	11.3	12.7	14.1	15.5	16.9	18.3
0.5	4.90	5.67	2.90	1.08	0.41	0.17	0.07	0.02	0.00	0.00
1	5.09	7.84	4.87	1.88	0.65	0.19	0.07	0.02	0.00	0.00
1.5	2.49	6.33	5.58	2.17	0.77	0.25	0.09	0.01	0.00	0.00
2	0.67	4.21	5.40	2.41	0.76	0.27	0.11	0.02	0.00	0.00
2.5	0.09	1.88	4.23	3.04	0.76	0.24	0.12	0.04	0.01	0.00
3	0.01	0.36	2.63	3.14	1.00	0.20	0.09	0.04	0.01	0.00
3.5	0.00	0.04	1.13	2.38	1.47	0.24	0.06	0.02	0.01	0.00
4	0.00	0.00	0.21	1.42	1.48	0.31	0.06	0.02	0.01	0.00
4.5	0.00	0.00	0.01	0.61	0.97	0.45	0.07	0.02	0.01	0.00
5	0.00	0.00	0.00	0.14	0.57	0.52	0.09	0.02	0.01	0.00
5.5	0.00	0.00	0.00	0.01	0.22	0.32	0.19	0.09	0.00	0.00
6	0.00	0.00	0.00	0.01	0.01	0.09	0.22	0.14	0.01	0.00
6.5	0.00	0.00	0.00	0.01	0.01	0.02	0.11	0.12	0.02	0.00
7	0.00	0.00	0.00	0.00	0.00	0.00	0.06	0.11	0.05	0.00
7.5	0.00	0.00	0.00	0.00	0.00	0.00	0.02	0.09	0.06	0.00
8	0.00	0.00	0.00	0.00	0.00	0.00	0.01	0.05	0.05	0.01
8.5	0.00	0.00	0.00	0.00	0.00	0.00	0.00	0.01	0.02	0.01
9	0.00	0.00	0.00	0.00	0.00	0.00	0.00	0.01	0.02	0.01
9.5	0.00	0.00	0.00	0.00	0.00	0.00	0.00	0.00	0.01	0.01
10	0.00	0.00	0.00	0.00	0.00	0.00	0.00	0.00	0.00	0.01

Table 5.10 Sea states probability distribution in % of the Yeu-island site (26.8 kW/m) [26]

$T_p(s)$ / $H_s(m)$	3.5	4.5	5.5	6.5	7.5	8.5	9.5	10.5	11.5	12.5	13.5	14.5	15.5	16.5
0.75	0.34	1.22	1.89	2.20	2.49	2.13	1.28	0.63	0.21	0.01	0.01	0.00	0.00	0.00
1.25	0.17	0.93	2.05	3.12	3.78	3.32	2.22	1.39	0.82	0.33	0.07	0.02	0.01	0.00
1.75	0.00	0.11	0.80	2.20	3.05	2.71	2.05	1.44	1.00	0.57	0.17	0.07	0.02	0.00
2.25	0.00	0.00	0.21	1.13	2.65	3.23	2.75	1.76	0.91	0.59	0.27	0.10	0.02	0.00
2.75	0.00	0.00	0.00	0.29	2.16	3.85	3.55	2.22	1.13	0.77	0.44	0.17	0.04	0.00
3.25	0.00	0.00	0.00	0.05	1.09	2.94	3.22	2.01	1.15	0.79	0.53	0.30	0.12	0.02
3.75	0.00	0.00	0.00	0.00	0.22	1.43	2.17	1.51	0.90	0.58	0.44	0.33	0.21	0.08
4.25	0.00	0.00	0.00	0.00	0.01	0.42	0.92	0.88	0.59	0.33	0.22	0.18	0.13	0.06
4.75	0.00	0.00	0.00	0.00	0.00	0.08	0.28	0.47	0.39	0.17	0.08	0.04	0.01	0.00
5.25	0.00	0.00	0.00	0.00	0.00	0.01	0.08	0.25	0.25	0.12	0.05	0.00	0.00	0.00
5.75	0.00	0.00	0.00	0.00	0.00	0.00	0.04	0.15	0.18	0.08	0.02	0.00	0.00	0.00
6.25	0.00	0.00	0.00	0.00	0.00	0.00	0.01	0.06	0.10	0.05	0.01	0.00	0.00	0.00
6.75	0.00	0.00	0.00	0.00	0.00	0.00	0.00	0.01	0.02	0.02	0.00	0.00	0.00	0.00
7.25	0.00	0.00	0.00	0.00	0.00	0.00	0.00	0.00	0.01	0.01	0.00	0.00	0.00	0.00

Table 5.11 Sea states probability distribution in % of the Lisbon site (37.5 kW/m) [26]

$T_p(s)$ / $H_s(m)$	7.075	8.225	9.375	10.525	11.675	12.825	13.975	15.125	16.275	17.425
0.5	0.18	0.33	0.23	0.08	0.02	0.00	0.00	0.00	0.00	0.00
1	1.37	2.89	2.87	1.42	0.35	0.02	0.00	0.00	0.00	0.00
1.5	2.51	4.87	5.02	3.47	1.82	0.76	0.18	0.02	0.00	0.00
2	2.08	3.95	4.08	3.71	3.02	2.13	0.96	0.18	0.02	0.00
2.5	0.94	2.56	3.10	2.82	2.64	2.64	1.91	0.65	0.13	0.00
3	0.18	1.30	2.26	2.13	1.91	2.00	1.85	1.02	0.28	0.02
3.5	0.00	0.43	1.24	1.52	1.39	1.24	1.11	0.89	0.41	0.08
4	0.00	0.05	0.50	0.99	0.99	0.76	0.65	0.63	0.41	0.15
4.5	0.00	0.00	0.18	0.54	0.61	0.54	0.54	0.43	0.33	0.20
5	0.00	0.00	0.05	0.23	0.39	0.41	0.35	0.28	0.23	0.15
5.5	0.00	0.00	0.00	0.08	0.23	0.26	0.18	0.15	0.13	0.08
6	0.00	0.00	0.00	0.02	0.13	0.18	0.13	0.08	0.05	0.02
6.5	0.00	0.00	0.00	0.00	0.05	0.11	0.11	0.05	0.00	0.00
7	0.00	0.00	0.00	0.00	0.00	0.02	0.08	0.05	0.00	0.00
7.5	0.00	0.00	0.00	0.00	0.00	0.00	0.02	0.02	0.00	0.00

Table 5.12 Sea states probability distribution in % of the Belmullet site (80.6 kW/m) [26]

$T_P(s)$ / $H_s(m)$	5.8	6.385	6.97	7.55	8.14	8.725	9.31	9.895	10.48	11.06	11.65	12.23	12.82	13.40	13.99	14.57	15.16	15.74	16.33
0.75	0.06	0.03	0.05	0.06	0.08	0.10	0.16	0.28	0.24	0.29	0.36	0.26	0.14	0.08	0.05	0.02	0.02	0.00	0.00
1.25	0.20	0.19	0.15	0.27	0.45	0.63	0.70	0.80	0.77	0.69	0.67	0.48	0.22	0.14	0.08	0.03	0.05	0.02	0.01
1.75	0.15	0.20	0.23	0.41	0.72	1.07	1.27	1.36	1.38	1.27	0.94	0.49	0.22	0.23	0.14	0.05	0.05	0.02	0.01
2.25	0.01	0.05	0.17	0.35	0.65	1.05	1.39	1.67	1.82	1.78	1.29	0.67	0.46	0.37	0.15	0.03	0.03	0.01	0.00
2.75	0.00	0.00	0.06	0.21	0.55	0.96	1.27	1.59	1.93	1.93	1.46	0.87	0.59	0.43	0.20	0.06	0.03	0.03	0.01
3.25	0.00	0.00	0.01	0.05	0.27	0.66	0.98	1.39	1.85	2.05	1.80	1.09	0.69	0.45	0.17	0.08	0.03	0.03	0.01
3.75	0.00	0.00	0.00	0.00	0.03	0.21	0.51	0.98	1.41	1.88	1.96	1.35	0.88	0.53	0.20	0.06	0.03	0.03	0.01
4.25	0.00	0.00	0.00	0.00	0.00	0.02	0.16	0.53	0.93	1.56	1.94	1.50	1.06	0.71	0.31	0.09	0.02	0.02	0.01
4.75	0.00	0.00	0.00	0.00	0.00	0.01	0.07	0.29	0.64	1.21	1.70	1.56	1.14	0.67	0.35	0.17	0.06	0.05	0.02
5.25	0.00	0.00	0.00	0.00	0.00	0.00	0.00	0.06	0.26	0.63	1.08	1.45	1.17	0.55	0.30	0.17	0.07	0.05	0.02
5.75	0.00	0.00	0.00	0.00	0.00	0.00	0.00	0.00	0.06	0.21	0.56	1.02	1.07	0.66	0.30	0.15	0.05	0.00	0.00
6.25	0.00	0.00	0.00	0.00	0.00	0.00	0.00	0.00	0.00	0.01	0.22	0.53	0.72	0.64	0.38	0.17	0.06	0.01	0.00
6.75	0.00	0.00	0.00	0.00	0.00	0.00	0.00	0.00	0.00	0.00	0.10	0.30	0.45	0.53	0.44	0.21	0.07	0.02	0.00
7.25	0.00	0.00	0.00	0.00	0.00	0.00	0.00	0.00	0.00	0.00	0.03	0.14	0.26	0.42	0.42	0.23	0.09	0.01	0.00
7.75	0.00	0.00	0.00	0.00	0.00	0.00	0.00	0.00	0.00	0.00	0.00	0.03	0.13	0.26	0.26	0.16	0.07	0.00	0.00
8.25	0.00	0.00	0.00	0.00	0.00	0.00	0.00	0.00	0.00	0.00	0.00	0.01	0.05	0.10	0.10	0.08	0.05	0.00	0.00
8.75	0.00	0.00	0.00	0.00	0.00	0.00	0.00	0.00	0.00	0.00	0.00	0.00	0.00	0.03	0.05	0.03	0.05	0.02	0.00
9.25	0.00	0.00	0.00	0.00	0.00	0.00	0.00	0.00	0.00	0.00	0.00	0.00	0.00	0.02	0.03	0.01	0.02	0.02	0.00
9.75	0.00	0.00	0.00	0.00	0.00	0.00	0.00	0.00	0.00	0.00	0.00	0.00	0.00	0.01	0.01	0.00	0.00	0.00	0.00
10.25	0.00	0.00	0.00	0.00	0.00	0.00	0.00	0.00	0.00	0.00	0.00	0.00	0.00	0.00	0.00	0.00	0.01	0.02	0.01
10.75	0.00	0.00	0.00	0.00	0.00	0.00	0.00	0.00	0.00	0.00	0.00	0.00	0.00	0.00	0.00	0.00	0.02	0.05	0.02
11.25	0.00	0.00	0.00	0.00	0.00	0.00	0.00	0.00	0.00	0.00	0.00	0.00	0.00	0.00	0.00	0.00	0.01	0.02	0.01
11.75	0.00	0.00	0.00	0.00	0.00	0.00	0.00	0.00	0.00	0.00	0.00	0.00	0.00	0.00	0.00	0.00	0.00	0.00	0.00
12.25	0.00	0.00	0.00	0.00	0.00	0.00	0.00	0.00	0.00	0.00	0.00	0.00	0.00	0.00	0.00	0.00	0.00	0.00	0.01
12.75	0.00	0.00	0.00	0.00	0.00	0.00	0.00	0.00	0.00	0.00	0.00	0.00	0.00	0.00	0.00	0.00	0.00	0.00	0.01
13.25	0.00	0.00	0.00	0.00	0.00	0.00	0.00	0.00	0.00	0.00	0.00	0.00	0.00	0.00	0.00	0.00	0.00	0.00	0.00
13.75	0.00	0.00	0.00	0.00	0.00	0.00	0.00	0.00	0.00	0.00	0.00	0.00	0.00	0.00	0.00	0.00	0.00	0.00	0.00
14.25	0.00	0.00	0.00	0.00	0.00	0.00	0.00	0.00	0.00	0.00	0.00	0.00	0.00	0.00	0.00	0.00	0.00	0.00	0.00

The power matrix given in Table 5.7 for the chosen Wavergy design, was obtained by using the wave site of the benchmark Pelamis device. This wave site has a power resource of roughly 4.5 kW/m and a dominant wave period of 5.5 s corresponding to a wave length of about 47 m. However, the devices studied in [26] were designed for higher wave sites with higher power resource with longer dominant wave period of about 8 s corresponding to a wave length of about 100 m. Consequently, in order to be able to compare Wavergy's performance to the aforementioned working principles the geometric properties of the chosen design given in Table 5.5 are multiplied by a factor of 2.12 which is the ratio between the dominant wavelengths of the wave sites in [26] and the wave site of the Pelamis benchmark device. The geometric parameters values of the scaled Wavergy device are given in Table 5.13. The power matrix for the scaled Wavergy design which was generated using the same method described in the previous section is given in Table 5.14.

Table 5.13 Geometric parameters values for the scaled Wavergy design

Parameter	Value
Total Number of Modules in full configuration (N)	15
Major semi-axis (a)	4.44 m
Axis ratio (b/a)	0.65
Transverse span (s)	9.48 m
Submergence depth of lower blanket (d)	14.2 m
Longitudinal joint spacing to length ratio ($L_s/2a$)	0.55
Minimum transverse spacing between modules to span ratio (T_s/s)	0.5

Table 5.14 Optimised power matrix for the scaled Wavergy design (kW)

T_p(s) / H_s(m)	4	5	6	7	8	9	10	11	12	13	14	15	16
0.5	5	9	13	19	23	24	23	20	17	14	12	10	8
1.5	47	97	121	168	211	219	203	177	150	125	105	88	74
2.5	130	294	393	512	586	608	563	490	416	348	292	245	207
3.5		577	797	1099	1427	1227	1103	961	816	683	572	479	405
4.5			1318	1846	2719	2213	1809	1589	1348	1129	946	792	669
5.5			1969	2758	4116	3522	2640	2270	2014	1686	1412	1184	1000
6.5				3851	5748	4993	3633	2988	2656	2355	1973	1653	1397
7.5				5128	7653	6648	4760	3744	3296	2971	2626	2201	1860
8.5				6586	9830	8539	6070	4622	3976	3564	3221	2827	2388
9.5				8227	12279	10666	7582	5588	4687	4177	3769	3430	2984
10.5				10050	15000	13030	9262	6826	5413	4810	4342	3951	3591

Comparing the two power matrices in Table 5.7Table 5.14, it can be seen that the mean absorbed power values has increased significantly for larger waves and the wave period with maximum power values has shifted from 5 s to 8 s. The performance evaluation measures of the selection of WECs in [26] together with the values of the performance evaluation measures for both the original chosen Wavergy device (W15) and the one scaled for comparison (W15×S) are given in Figures 5.31 to 5.34. The characteristic mass and surface area of the Wavergy device are taken as the mass displaced by half the total volume of the device and the wetted surface area respectively.

	W15	W15xS	Bref-HB	Bref-SHB	F-2HB	B-HBA	F-HBA	B-OF	F-3OF	F-OWC
SEM-REV	16.2	233.7	1.6	8.8	79	127	224	211	52	147
EMEC	32.5	423.5	2.8	18.5	127	225	326	348	112	262
Yeu Island	41.4	563.7	3.3	22	191	280	409	440	131	337
Lisbon	33.0	502.5	3.5	19	199	303	317	513	104	367
Bemullet	59.1	992.3	5	31	373	612	417	981	145	745
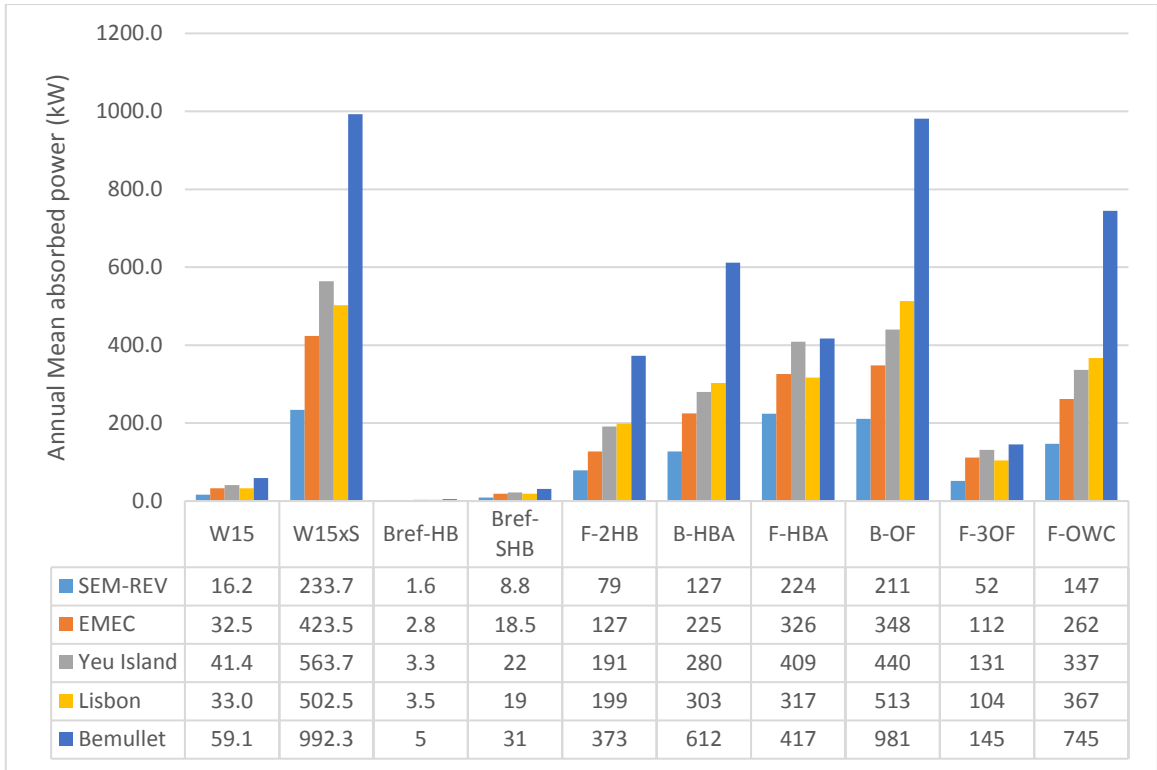
Figure 5.31 Mean annual absorbed power comparison

	W15	W15xS	Bref-HB	Bref-SHB	F-2HB	B-HBA	F-HBA	B-OF	F-3OF	F-OWC
SEM-REV	3.49	23.77	3.6	9	27	14	11	61	14	41
EMEC	4.75	29.24	4.2	13	29	16	11	68	20	50
Yeu Island	4.92	31.66	4.1	13	36	17	11	72	20	52
Lisbon	2.80	20.17	3.1	8	27	12	6.4	58	11	41
Bemullet	2.34	18.53	2.1	6	23	12	3.9	52	7	38
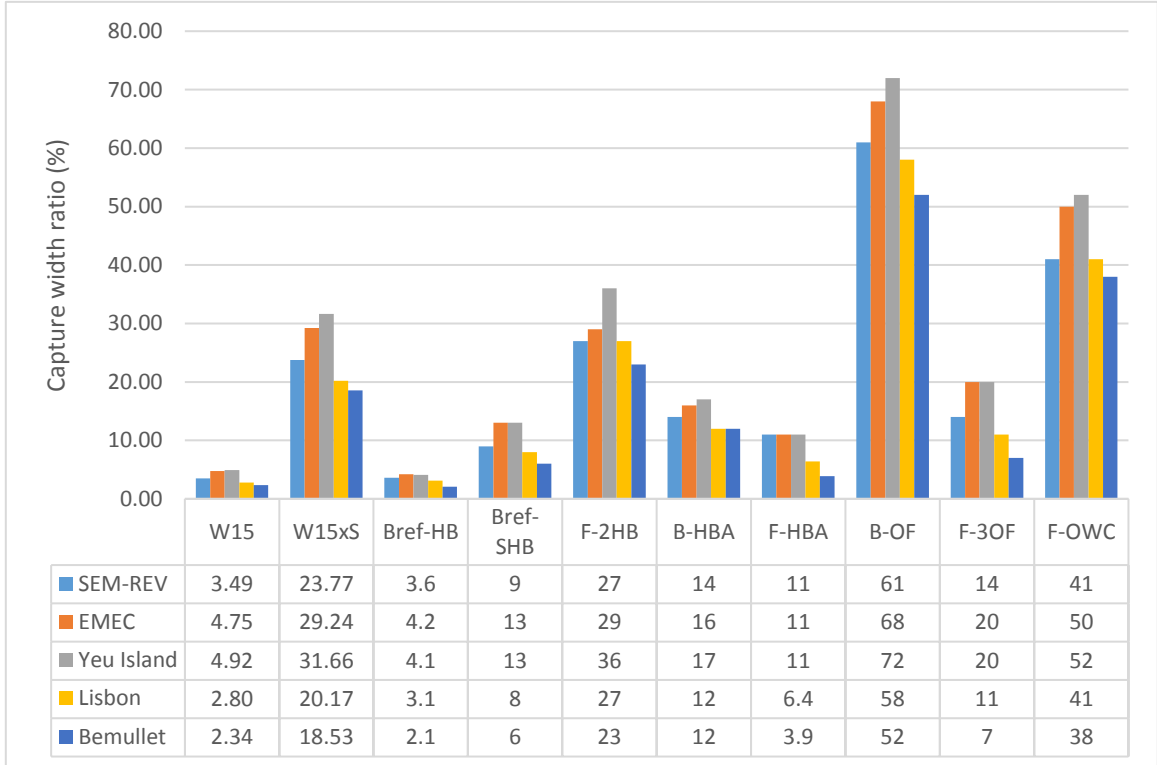
Figure 5.32 Capture width ratio comparison
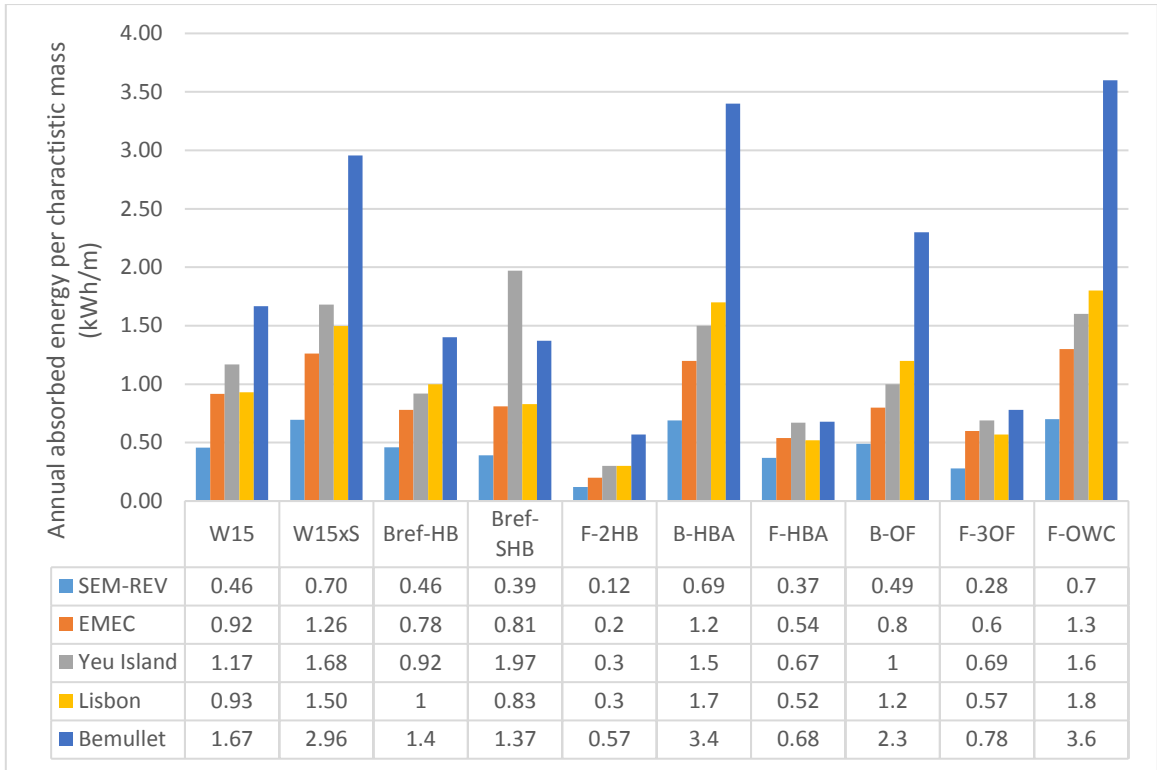
Figure 5.33 Annual absorbed energy per characteristic mass comparison

	W15	W15xS	Bref-HB	Bref-SHB	F-2HB	B-HBA	F-HBA	B-OF	F-3OF	F-OWC
SEM-REV	0.46	0.70	0.46	0.39	0.12	0.69	0.37	0.49	0.28	0.7
EMEC	0.92	1.26	0.78	0.81	0.2	1.2	0.54	0.8	0.6	1.3
Yeu Island	1.17	1.68	0.92	1.97	0.3	1.5	0.67	1	0.69	1.6
Lisbon	0.93	1.50	1	0.83	0.3	1.7	0.52	1.2	0.57	1.8
Bemullet	1.67	2.96	1.4	1.37	0.57	3.4	0.68	2.3	0.78	3.6
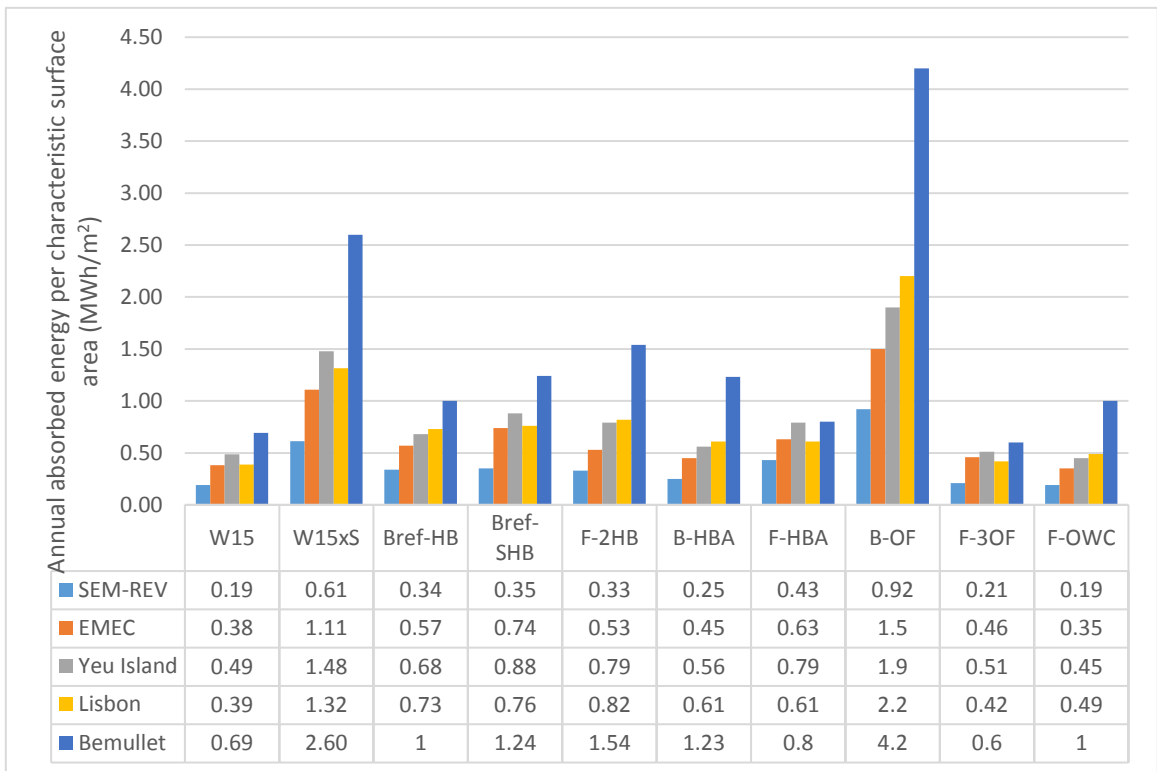
Figure 5.34 Annual absorbed energy per characteristic area comparison

	W15	W15xS	Bref-HB	Bref-SHB	F-2HB	B-HBA	F-HBA	B-OF	F-3OF	F-OWC
SEM-REV	0.19	0.61	0.34	0.35	0.33	0.25	0.43	0.92	0.21	0.19
EMEC	0.38	1.11	0.57	0.74	0.53	0.45	0.63	1.5	0.46	0.35
Yeu Island	0.49	1.48	0.68	0.88	0.79	0.56	0.79	1.9	0.51	0.45
Lisbon	0.39	1.32	0.73	0.76	0.82	0.61	0.61	2.2	0.42	0.49
Bemullet	0.69	2.60	1	1.24	1.54	1.23	0.8	4.2	0.6	1

Figure 5.31 shows that the mean absorbed power of the Wavergy device designed for the Pelamis benchmark wave site only exceeds the mean absorbed power of the small bottom-referenced heaving buoy (Bref-HB), and the bottom-referenced submerged heave-buoy (Bref-SHB). However, the scaled Wavergy device has the highest mean absorbed power among all the devices across all the five wave sites.

In Figure 5.32, the *CWR* of W15 is second to last among all of the devices only surpassing the small bottom-referenced heaving buoy (Bref-HB) device. The W15×S device ranks 3rd to 4th highest *CWR* across all wave sites. The large variation in *CWR* between the two designs, (2.34 to 4.95 %) for W15 and (18.53 to 31.66 %) for W15×S, highlights the high dependency of the Wavergy design on the deployment wave site. Hence, a generic standardized design for a wide range of wave sites with different power resource levels would not be feasible.

Wavergy's energy absorbed per characteristic mass shows good results in comparison with the other WECs for both the W15 and the W15×S designs. The annual absorbed energy per characteristic mass values of the Wavergy device ranks 3rd to 5th for the W15 design and 2nd to 3rd for the W15×S design across all wave sites and both surpass that of the floating three-body oscillating flap device (F-3OF) which is a floating oscillating wave surge converter as Wavergy. This suggests that increasing the size of Wavergy would be more beneficial and results in better power absorption properties. Finally, the annual absorbed energy per characteristic area values for the Wavergy device rank 8th to 9th for the W15 design and 2nd for the W15×S design across all wave sites.

Although the results for the scaled design are promising, they should be handled with caution since they only reflect the hydrodynamic aspects of the working concept behind the Wavergy device and they do not take into account the structural integrity or the cost-effectiveness of the device. Overall, the results show that the Wavergy device has the potential to give a very good power performance in different wave sites compared to other WECs.

Chapter 6 : Conclusions and Recommendations for future Work

The novel patent-pending Wavergy WEC was hydrodynamically analysed using the Pelamis device as a guiding benchmark WEC with a proven working principle. The resources used by this Pelamis device to extract wave energy including its total volume, total PTO damping coefficient and its deployment wave site were applied to the optimisation procedure of the Wavergy device. The Wavergy device was modelled using the hydrodynamic diffraction/radiation BEM software ANSYS AQWA and the motions responses of the device were obtained using frequency-domain statistical analysis.

The optimisation methodology used in this work is similar to the one used by Shadman et al. in [33], where a response surface method optimisation followed by a gradient-based optimisation scheme was used to optimise and refine the geometrical properties of the device. All the optimisation schemes were implemented using the built-in ANSYS DesignXplorer software. The optimisation process of the Wavergy device was split into two steps in order to reduce the computational efforts. The first step involved using only a single surface-piercing elliptical cylinder module of the Wavergy device to optimise its geometry. In the second step, using the optimised module geometry resulting from the previous step, three full modular configurations were modelled with 15, 21 and 27 modules to investigate the effects of module spacing, depth of submergence of lower module blanket and size of the device on the power performance of the Wavergy device. Finally, the Wavergy device was compared with a selection of eight benchmark devices that was studied by Babrit et al. in [26] with various working principles in five different representative wave sites with wave power resources ranging from 15 to 80 kW/m.

6.1 Conclusions

1. For maximum mean absorbed power, the results showed that the device tend to maximize the projected lateral area perpendicular to the direction of wave propagation by maximizing the span and minor axis and minimizing the major axis. On the other hand, the maximum *CWR* values occurred at minimum span values. The depth of submergence of the fixed points had an optimal value of around 13 m for all of the three single module sizes. A maximum *CWR* of around 0.21 was achieved at the optimum depth. The optimisation for the single module was performed with two objectives and one constraint. The two objectives were to maximize mean absorbed power and minimize the axis ratio and the constraint was a lower limit of 0.085 for the *CWR*. It was found that a major semi-axis of 2.1 m and an axis ratio of 0.65 represent a compromise between the two objectives for all of the three single module sizes and thus were chosen to be used in the full modular configuration modelling of the Wavergy device.

2. For full modular configurations of the Wavergy device, the longitudinal spacing was found to have a significant impact on mean absorbed power and *CWR* where both their values increase by 60 to 80% between the maximum and minimum values of ($L_s/2a$) at constant (T_s/s) values across all three modular configurations. Conversely, the transverse spacing had the opposite effect on mean absorbed power where power increased with increasing transverse spacing, however, this effect was less significant than that of the longitudinal

80

spacing as only 8 to 12% increase in mean absorbed power between the minimum and maximum values of (T_s/s) for constant ($L_s/2a$) values was achieved across all three modular configurations. On the other hand, *CWR* slightly decreases with increasing transverse spacing due to larger active widths. Values of 0.55 and 0.5 were chosen for ($L_s/2a$) and (T_s/s), respectively. Power levels and *CWR* for all of the three full modular configurations were very close suggesting that for the same module cross-section, total volume and total PTO damping coefficient the power is independent of the number of modules. This is an advantage of the Wavergy device that can make the device's manufacturing flexible and provide versatility in deployment configuration.

3. The effect of submergence depth of the lower blanket on the mean absorbed power was studied and it was found that, for all of the three modular configurations, an optimum submergence depth of the lower blanket of around 13 m exists which agrees with the single module results. However, the *CWR* at the optimum depth shows significant improvement for the full modular configuration over the single module with a value of about 0.35 for the modular configuration and a value of 0.085 for the single module. To limit the adverse effects that a large submergence depth of the lower blanket might have on the structural integrity of the device, a value of 6.7 m was chosen so that the Wavergy device generates the same mean absorbed power as the Pelamis benchmark device with the same total volume at the design wave site.

4. To study the effect of the size of the device on its power performance, the chosen Wavergy design size was varied by increasing the number of modules, increasing the span of individual modules, and scaling the dimensions of the individual modules. It was found that the effect of increasing the size of the device by increasing the number of modules results in the largest mean absorbed power and *CWR* values. Increasing the span of individual modules of the chosen 15 module configuration to correspond to the total volume of the 21, 27 and 33 module device produces power results close to that of increasing volume by adding modules, however, the difference in *CWR* values is more prominent since increasing the span of the device while maintaining a constant value of (T_s/s) means a larger active width of the device. Finally, increasing the device's size by scaling the modules dimensions had the least effect on power. All of the three methods have more effect on enhancing power performance than increasing the diameter of the Pelamis benchmark device and the first two methods surpass the Pelamis' *CWR* beyond total volume values of 950 and 1090 m^3 respectively.

5. The optimised power matrix for the chosen Wavergy device was obtained by tuning the total PTO damping coefficient to 6 wave peak periods (T_p) of 4 s to 16 s with a 2 s step and a significant wave height (H_s) of 1 m. Optimum PTO damping coefficients were found using a gradient-based optimisation scheme and an optimised power matrix for the device was generated by interpolating between the values obtained at the mentioned wave periods. The power matrix showed that the device absorbs more power from shorter waves than longer waves which was expected since the design wave site was dominated by relatively short wave periods (5 s to 6.5 s).

6. Since the Wavergy optimisation procedure was carried out for a wave site with a relatively low wave power resource (4.5 kW/m), the geometry of the chosen Wavergy design was scaled by a factor of 2.12 which is the ratio between the dominant wavelengths in the five representative wave sites in [26] and the design wave site in [30] for the sake of comparison. The following four performance evaluation measures were used in the comparison: the annual mean absorbed power (kW), capture width ratio (%), annual absorbed energy per characteristic mass (kWh/kg) and annual absorbed energy per wetted surface area (MWh/kg). The comparison showed that the performance of the scaled Wavergy device was superior to most working principles in all performance measures where the device ranked 1st to 2nd in mean absorbed power, 3rd to 4th in capture width ratio, 2nd to 3rd in annual power per characteristic mass and 2nd in annual mean absorbed energy per characteristic area across all five sea states.

6.2 Recommendations for future work

Although the results show that the working principle of the Wavergy device is hydrodynamically sound, it is stressed here that other factors like structural survivability, PTO control method and cost effectiveness must be taken into consideration in order to fully assess the performance of the Wavergy device. With that in mind, the following list gives suggestions for further future work on the Wavergy device:

1. Investigating the effects of using shapes other than the elliptical cylinder perhaps with only one or no plane of symmetry.

2. Investigating the effect of wave directionality and the possibility of using universal joints instead of hinged joints to improve the device's performance in various wave headings.

3. Optimising the device for various wave sites.

4. Optimisation of the mooring arrangement.

5. Incorporating structural analysis of the design in the optimisation process.

6. Cost-effectiveness analysis.

List of references

[1]   Babarit, A., *Ocean wave energy conversion: resource, technologies and performance*. 2017: Elsevier.

[2]   Wavergy. *Wavergy Ocean Wave Energy And Storm Mitigation Solution*. [cited 15/6/2019]; Available from: www.wavergy.net.

[3]   Panicker, N.N., *Power resource estimate of ocean surface waves.* Ocean Engineering, 1976. **3**(6): p. 429-439.

[4]   Kinsman, B., *Wind waves : their generation and propagation on the ocean surface*. 1965, Englewood Cliffs, N.J.: Prentice-Hall.

[5]   Mork, G., Barstow, S., Kabuth, A., and Pontes, M.T. *Assessing the global wave energy potential*. in *ASME 2010 29th International conference on ocean, offshore and arctic engineering*. 2010. American Society of Mechanical Engineers.

[6]   Gunn, K. and Stock-Williams, C., *Quantifying the global wave power resource.* Renewable Energy, 2012. **44**: p. 296-304.

[7]   IRENA, *REN21 (2018) GLOBAL STATUS REPORT* 2018.

[8]   Antonio, F., *Wave energy utilization: A review of the technologies.* 2010. **14**(3): p. 899-918.

[9]   Heath, T., *A review of oscillating water columns.* 2012. **370**(1959): p. 235-245.

[10]   Heath, T., *The construction, commissioning and operation of the LIMPET wave energy collector.* 2001.

[11]   Edwards, K. and Mekhiche, M., *Ocean Power Technologies Powerbuoy®: System‐Level Design, Development and Validation Methodology.* 2014.

[12]   Yemm, R., Henderson, R., and Taylor, C. *The OPD Pelamis WEC: Current status and onward programme*. in *Proc. 4th European Wave Energy Conference, Alborg Denmark*. 2000.

[13]   Cruz, J., *Ocean wave energy: current status and future prespectives*. 2007: Springer Science & Business Media.

[14]   EMEC. *PELAMIS WAVE POWER*. [cited 26/6/2019]; Available from: http://www.emec.org.uk/about-us/wave-clients/pelamis-wave-power/.

[15]   Whittaker, T., Collier, D., Folley, M., Osterried, M., Henry, A., and Crowley, M. *The development of Oyster—a shallow water surging wave energy converter*. in *Proceedings of the 7th European wave and tidal energy conference*. 2007.

[16]   EMEC.   *AQUAMARINE   POWER*.   [cited   30/6/2019];   Available   from:
         http://www.emec.org.uk/about-us/wave-clients/aquamarine-power/.

[17]   Kofoed, J.P., Frigaard, P., Sorenson, H.C., and Friis-Madsen, E. *Development of the wave
         energy converter-Wave Dragon*. in *The Tenth International Offshore and Polar
         Engineering Conference*. 2000. International Society of Offshore and Polar Engineers.

[18]   WaveDragon. [cited 1/7/2019]; Available from: http://www.wavedragon.co.uk/.

[19]   SeaEnergy.   *ANACONDA*.   [cited   2/7/2019];   Available   from:
         https://www.checkmateukseaenergy.com/anaconda/.

[20]   Chaplin, J., Farley, F., Prentice, M., Rainey, R., Rimmer, S., and Roach, A.J.P.t.E.,
         Development of the ANACONDA all-rubber WEC. 2007.

[21]   Ahmed, T.M., Welaya, Y., and Abdulmotaleb, S.M. *Numerical Modeling of the
         Hydrodynamic Performance of Hydrofoils for Auxiliary Propulsion of Ships in Regular
         Head-Waves*. in *ASME 2017 36th International Conference on Ocean, Offshore and Arctic
         Engineering*. 2017. American Society of Mechanical Engineers.

[22]   Bøckmann, E. and Steen, S. *The effect of a fixed foil on ship propulsion and motions*. in
         Proceedings of the Third International Symposium on Marine Propulsors (SMP2013).
         2013.

[23]   Kempener, R. and Neumann, F., *Wave energy technology brief*. 2014.

[24]   Babarit, A. and Clément, A. *Shape Otimisation of the SEAREV Wave Energy Converter*.
         2006.

[25]   McCabe, A., Aggidis, G., and Widden, M., *Optimizing the shape of a surge-and-pitch wave
         energy collector using a genetic algorithm*. 2010. **35**(12): p. 2767-2775.

[26]   Babarit, A., Hals, J., Muliawan, M.J., Kurniawan, A., Moan, T., and Krokstad, J.,
         Numerical benchmarking study of a selection of wave energy converters. Renewable
         Energy, 2012. **41**: p. 44-63.

[27]   McCabe, A., *Constrained optimization of the shape of a wave energy collector by genetic
         algorithm*. 2013. **51**: p. 274-284.

[28]   Kurniawan, A. and Moan, T., *Optimal geometries for wave absorbers oscillating about a
         fixed axis*. 2012. **38**(1): p. 117-130.

[29]   Goggins, J. and Finnegan, W., *Shape optimisation of floating wave energy converters for a
         specified wave energy spectrum*. 2014. **71**: p. 208-220.

[30]   Shengnan, L., Liping, S., and Jianxun, Z., *Influence Analysis of Pelamis Wave Energy
         Converter Structure Parameters*. 2014. **8**(6): p. 930-936.

[31]   Babarit, A., *A database of capture width ratio of wave energy converters.* 2015. **80**: p. 610-628.

[32]   de Andres, A., Maillet, J., Todalshaug, J.H., Möller, P., and Jeffrey, H. *On the Optimum Sizing of a Real WEC from a Techno-Economic Perspective*. in *ASME 2016 35th International Conference on Ocean, Offshore and Arctic Engineering*. 2016. American Society of Mechanical Engineers.

[33]   Shadman, M., Estefen, S.F., Rodriguez, C.A., and Nogueira, I.C.J.R.e., *A geometrical optimization method applied to a heaving point absorber wave energy converter.* 2018. **115**: p. 533-546.

[34]   Al Shami, E., Wang, X., Zhang, R., and Zuo, L., *A parameter study and optimization of two body wave energy converters.* 2019. **131**: p. 1-13.

[35]   Folley, M., *Numerical modelling of wave energy converters: state-of-the-art techniques for single devices and arrays*. 2016: Academic Press.

[36]   Falnes, J., *Ocean waves and oscillating systems: linear interactions including wave-energy extraction*. 2002: Cambridge university press.

[37]   Newman, J.N., *Marine hydrodynamics*. 1977: MIT press.

[38]   Linton, C.M. and McIver, P., *Handbook of mathematical techniques for wave/structure interactions*. 2001: Chapman and Hall/CRC.

[39]   Cummins, W., *The impulse response function and ship motions*. 1962, David Taylor Model Basin Washington DC.

[40]   Fossen, T.I., *Handbook of marine craft hydrodynamics and motion control*. 2011: John Wiley & Sons.

[41]   Lloyd, A., *Seakeeping: ship behaviour in rough weather*. 1989: Ellis Horwood.

[42]   *Aqwa Theory Manual*. 2019, Release.

[43]   Pecher, A. and Kofoed, J.P., *Handbook of ocean wave energy*. 2017: Springer London.

[44]   Box, G.E. and Wilson, K.B., *On the experimental attainment of optimum conditions.* 1951. **13**(1): p. 1-38.

[45]   Agnevall, T. *Taut Leg Moorings Using Polyester and VLA Anchors*. in *IADC/SPE Drilling Conference*. 2004. Society of Petroleum Engineers.

[46]   *DesignXplorer User's Guide.* 2019.

[47]   Xu, X., Yang, J.-M., Li, X., and Xu, L., *Hydrodynamic performance study of two side-by-side barges.* 2014. **9**(5): p. 475-488.